

## CHARACTERIZING THE TRANSITION FROM DIFFUSE ATOMIC TO DENSE MOLECULAR CLOUDS IN THE MAGELLANIC CLOUDS WITH [C II], [C I], AND CO

JORGE L. PINEDA<sup>1</sup>, WILLIAM D. LANGER<sup>1</sup>, PAUL F. GOLDSMITH<sup>1</sup>, SHINJI HORIUCHI<sup>2</sup>, THOMAS B. H. KUIPER<sup>1</sup>, ERIK MULLER<sup>3</sup>, ANNIE HUGHES<sup>4</sup>, JÜRGEN OTT<sup>5</sup>, MIGUEL A. REQUENA-TORRES<sup>6</sup>, THANGASAMY VELUSAMY<sup>1</sup>, AND TONY WONG<sup>7</sup>

<sup>1</sup>Jet Propulsion Laboratory, California Institute of Technology, 4800 Oak Grove Drive, Pasadena, CA 91109-8099, USA

<sup>2</sup>CSIRO Astronomy & Space Science/NASA Canberra Deep Space Communication Complex, PO Box 1035, Tuggeranong ACT 2901, Australia

<sup>3</sup>National Astronomical Observatory of Japan, Chile Observatory, Tokyo, Mitaka, 181-8588, Japan

<sup>4</sup>CNRS, IRAP, 9 Av. Colonel Roche, BP 44346, 31028, Toulouse Cedex 4, France; Université de Toulouse, UPS-OMP, IRAP, 31028, Toulouse Cedex 4, France

<sup>5</sup>National Radio Astronomy Observatory, P.O. Box O, 1003 Lopezville Road, Socorro, NM 87801, USA

<sup>6</sup>Space Telescope Science Institute, 3700 San Martin Dr., Baltimore, 21218 MD, USA

<sup>7</sup>Department of Astronomy, University of Illinois, Urbana, IL 61801, USA

*To appear in the Astrophysical Journal*

### ABSTRACT

We present and analyze deep *Herschel*/HIFI observations of the [C II] 158  $\mu\text{m}$ , [C I] 609  $\mu\text{m}$ , and [C I] 370  $\mu\text{m}$  lines towards 54 lines-of-sight (LOS) in the Large and Small Magellanic clouds. These observations are used to determine the physical conditions of the line-emitting gas, which we use to study the transition from atomic to molecular gas and from C<sup>+</sup> to C<sup>0</sup> to CO in their low metallicity environments. We trace gas with molecular fractions in the range  $0.1 < f(\text{H}_2) < 1$ , between those in the diffuse H<sub>2</sub> gas detected by UV absorption ( $f(\text{H}_2) < 0.2$ ) and well shielded regions in which hydrogen is essentially completely molecular. The C<sup>0</sup> and CO column densities are only measurable in regions with molecular fractions  $f(\text{H}_2) > 0.45$  in both the LMC and SMC. Ionized carbon is the dominant gas-phase form of this element that is associated with molecular gas, with C<sup>0</sup> and CO representing a small fraction, implying that most (89% in the LMC and 77% in the SMC) of the molecular gas in our sample is CO-dark H<sub>2</sub>. The mean  $X_{\text{CO}}$  conversion factors in our LMC and SMC sample are larger than the value typically found in the Milky Way. When applying a correction based on the filling factor of the CO emission, we find that the values of  $X_{\text{CO}}$  in the LMC and SMC are closer to that in the Milky Way. The observed [C II] intensity in our sample represents about 1% of the total far-infrared intensity from the LOSs observed in both Magellanic Clouds.

*Subject headings:* ISM: molecules — ISM: structure

### 1. INTRODUCTION

Understanding the life cycle of the interstellar medium in galaxies is a primary goal in the study of galaxy evolution and star formation. The formation of molecular clouds, their subsequent evolution to initiate star formation, and the radiative and mechanical feedback of stars into their progenitor molecular gas that terminates or reignites star formation are fundamental aspects determining how galaxies evolve over cosmic time. Most of the star formation at early cosmological times took place in environments with reduced gas metallicity and dust-to-gas ratio. With the implementation of ALMA it is now possible to study a large number of high-redshift systems (e.g. Carilli & Walter 2013). To interpret these observations of poorly resolved high redshift galaxies it is necessary to understand local templates of the low-metallicity interstellar medium (ISM), that can be spatially and spectrally resolved in a detail that is not achievable for distant galaxies.

The best local templates for studying the life cycle of the ISM and star formation in low-metallicity environments are the Large and Small Magellanic clouds (LMC;  $Z=0.5 Z_{\odot}$  and SMC,  $Z=0.2 Z_{\odot}$ ; Westerlund 1997). Due to their proximity (LMC:  $D = 50$  kpc; SMC:  $D = 60$  kpc; Schaefer 2008; Hilditch et al. 2005), the Magellanic

clouds provide a unique opportunity to resolve individual clouds, allowing us to conduct detailed studies of the different phases of the ISM in low-metallicity environments using various gas and dust tracers.

The interstellar medium plays the critical role of fueling star formation in galaxies. Obtaining a complete census of the mass of the different phases of the interstellar medium is thus key for understanding star formation and its effect in the evolution of galaxies. Traditionally, the distribution of the ISM phases in galactic disks has been studied in H $\alpha$  or radio continuum emission to trace the ionized gas (e.g. Haffner et al. 2009), in the H I 21 cm line which traces atomic gas (e.g. Kalberla & Kerp 2009), and in the CO line to trace shielded molecular gas (e.g. Heyer & Dame 2015). The total dust mass of the interstellar medium has been traced by modeling the spectral energy distribution of dust continuum, but the conversion from dust mass to hydrogen mass is often complicated by finding appropriate values for the dust to gas ratio, dust emissivity and dust temperature, parameters that can vary with environmental conditions (Roman-Duval et al. 2014). We lack, however, observations of very important ISM phases constituting the transition between diffuse atomic clouds and dense molecular clouds. This missing link between diffuse atomic and dense molecular gas can be isolated and characterized with observations of the [C II] 158  $\mu\text{m}$  line that traces the diffuse ionized medium,

warm and cold atomic clouds, clouds in transition from atomic to molecular form, and dense and warm photon dominated regions (PDRs). In particular, the [C II] line is a tracer of the CO–dark H<sub>2</sub> gas (Madden et al. 1997; Grenier et al. 2005; Wolfire et al. 2010; Langer et al. 2010, 2014), which is gas in which hydrogen is molecular but carbon is ionized and thus not traced by CO but by [C II]. The CO–dark H<sub>2</sub> gas represents ~30% of the molecular mass of the Milky Way and this fraction increases with galactocentric distance, which is an effect of the metallicity gradient of the Galaxy (Pineda et al. 2013).

The reduced dust–to–gas ratio and lower abundance of species responsible for gas cooling (e.g. C and O) in metal poor environments impacts the relative distributions of different ISM phases and their thermal balance. In low dust–to–gas ratio environments, the dust column density required to form enough H<sub>2</sub> to self–shield efficiently against photo–destruction, enabling the transition from atomic to molecular gas, is achieved at larger gas column densities compared with larger dust–to–gas ratio environments (e.g. Gnedin et al. 2009; Krumholz et al. 2009; Sternberg et al. 2014). Additionally, due to the reduced attenuation of FUV photons by dust in low metallicity gas, the CO molecule is more readily photo–dissociated pushing the C<sup>+</sup>/C<sup>0</sup>/CO transition to higher molecular hydrogen column densities compared to higher metallicity systems (van Dishoeck & Black 1988). This effect results in an enhanced CO–to–H<sub>2</sub> conversion factor in the Magellanic Clouds (Cohen et al. 1988; Rubio et al. 1991; Israel 1997, 2000; Bolatto et al. 2013). Observations of the distribution of [C II], [C I], and CO line emission in the Magellanic clouds are thus important tools for studying how metallicity affects the properties of the different phases of the interstellar medium.

The [C II] line has been imaged in the entire Large Magellanic cloud with the BICE balloon by Mochizuki et al. (1994), with 15' angular resolution and 175 km s<sup>−1</sup> velocity resolution. These observations showed an enhanced [C II]/CO ratio compared with the Milky Way and that [C II] constitutes about 1.32% of the far–infrared luminosity of the LMC (Rubin et al. 2009). A handful of star forming regions in the LMC and SMC have been studied with the *Kuiper Airborne Observatory* both with low (Poglitsch et al. 1995; Israel et al. 1996; Israel & Maloney 2011) and with high (Boreiko & Betz 1991) velocity resolution observations. The 30 Doradus region in the LMC has been studied in detail with the PACS instrument on *Herschel* (Chevance et al. 2016). High velocity resolution [C II] images of H II regions in the LMC and SMC are starting to become available using SOFIA (Okada et al. 2015; Requena-Torres et al. 2016).

The [C II] 158 μm, [C I] 609 μm and 370 μm fine structure, and <sup>12</sup>CO and <sup>13</sup>CO rotational, transitions are diagnostics of the physical conditions of PDRs (e.g. Kim 2006; Minamidani et al. 2008, 2011; Pineda et al. 2008, 2012; Okada et al. 2015; Lee et al. 2016; Chevance et al. 2016). When compared with predictions from PDR models, the [C II] line constrains the strength of the FUV field and volume density. The excitation of the [C I] 609 μm and 370 μm lines can give independent estimates of the kinetic temperature and H<sub>2</sub> volume density (Stutzki et al. 1997). The ionized gas component can be characterized

with the [N II] 122 and 205 μm fine structure line emission (Goldsmith et al. 2015, Langer et al. 2016) as well as with hydrogen recombination lines and free–free continuum emission in the cm wavelength regime. Characterizing the physical conditions of the gas is key for our understanding to the origin of the [C II] emission in the Magellanic clouds and will have implications in the interpretation of observations of distant galaxies.

In this paper we present deep observations of the [C II] 158 μm, [C I] 609 μm, [C I] 370 μm, and <sup>12</sup>CO *J* = 7 → 6 lines towards 54 LMC and SMC lines-of-sight (LOS). These data were obtained using the HIFI (de Graauw et al. 2010) instrument onboard the *Herschel Space Observatory*<sup>1</sup> (Pilbratt et al. 2010). We complement this data set with observations of the *J* = 1 → 0 and *J* = 3 → 2 transitions of <sup>12</sup>CO and <sup>13</sup>CO from the Mopra and APEX telescopes, respectively. We base our target selection on maps of H I, 160 μm dust continuum emission, and CO emission as well as on results from the FUSE survey of H<sub>2</sub> absorption towards the Magellanic Clouds (Cartledge et al. 2005). The targets are distributed throughout the LMC and SMC in order to study spatial variations of the properties of their ISM. By studying clouds with different physical conditions we aim to determine the key factors that characterize the evolution of the interstellar matter in the Magellanic clouds.

This paper is organized as follows. In Section 2 we describe our sample selection and observations. We discuss the determination of the contributions of the different phases of the interstellar medium to the observed [C II] emission in Section 3 and we estimate in Section 4 the physical parameters of different ISM components. In Section 5, we study the H<sup>0</sup> to H<sub>2</sub> as well as the C<sup>+</sup>/C<sup>0</sup>/CO transitions in the LMC and SMC. We also discuss the CO–to–H<sub>2</sub> conversion factor, the relationship between [C II] and far–infrared dust emission in our sample, and we compare our single dish observations with pencil beam FUV and optical studies to characterize the substructure of the ISM in the Magellanic clouds. We present our conclusions in Section 6.

## 2. SAMPLE SELECTION AND OBSERVATIONS

### 2.1. Sample Selection

To characterize the transition from diffuse atomic to dense molecular clouds in the Magellanic clouds we need to study many different clouds having different physical conditions in their low metallicity environments. Therefore our work results in statistical properties of the sample of clouds rather than full understanding of an individual region. This strategy also allows us to search for locations that could be followed up with current or future observatories (e.g. SOFIA, STO).

Our sample consists of 36 LOSs in the LMC and 18 in the SMC. We show the locations used in our analysis in Figure 1. The locations of our LOSs were selected to be as uniformly distributed as possible over the LMC and SMC, and they do not necessarily represent the brightest emission peaks in these galaxies. We present sample spectra representing diffuse and dense photon dominated

<sup>1</sup> *Herschel* is an ESA space observatory with science instruments provided by European-led Principal Investigator consortia and with important participation from NASA.

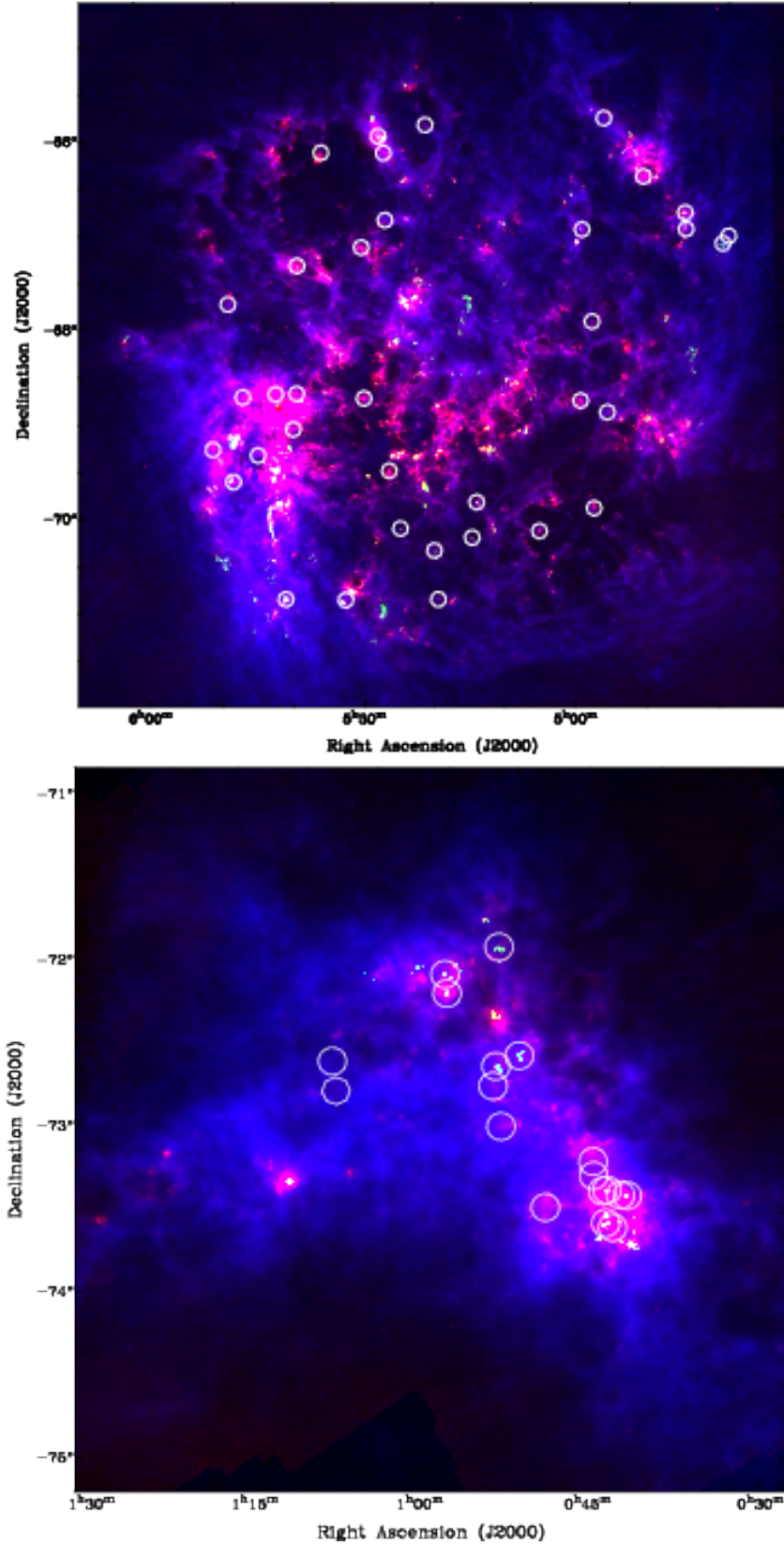


FIG. 1.— Images showing H<sup>0</sup> column density map (blue; Kim et al. 2003, Stanimirovic et al. 1999), *Herschel* 160  $\mu\text{m}$  continuum emission (red; Meixner et al. 2013), and MAGMA CO line emission (green; Wong et al. 2011 and Muller et al. 2017 in preparation) in the Large (*top*) and Small (*bottom*) Magellanic clouds. The white circles denote the positions studied in this paper. The size of the circles does not denote the beam size employed in any of the observations presented here.

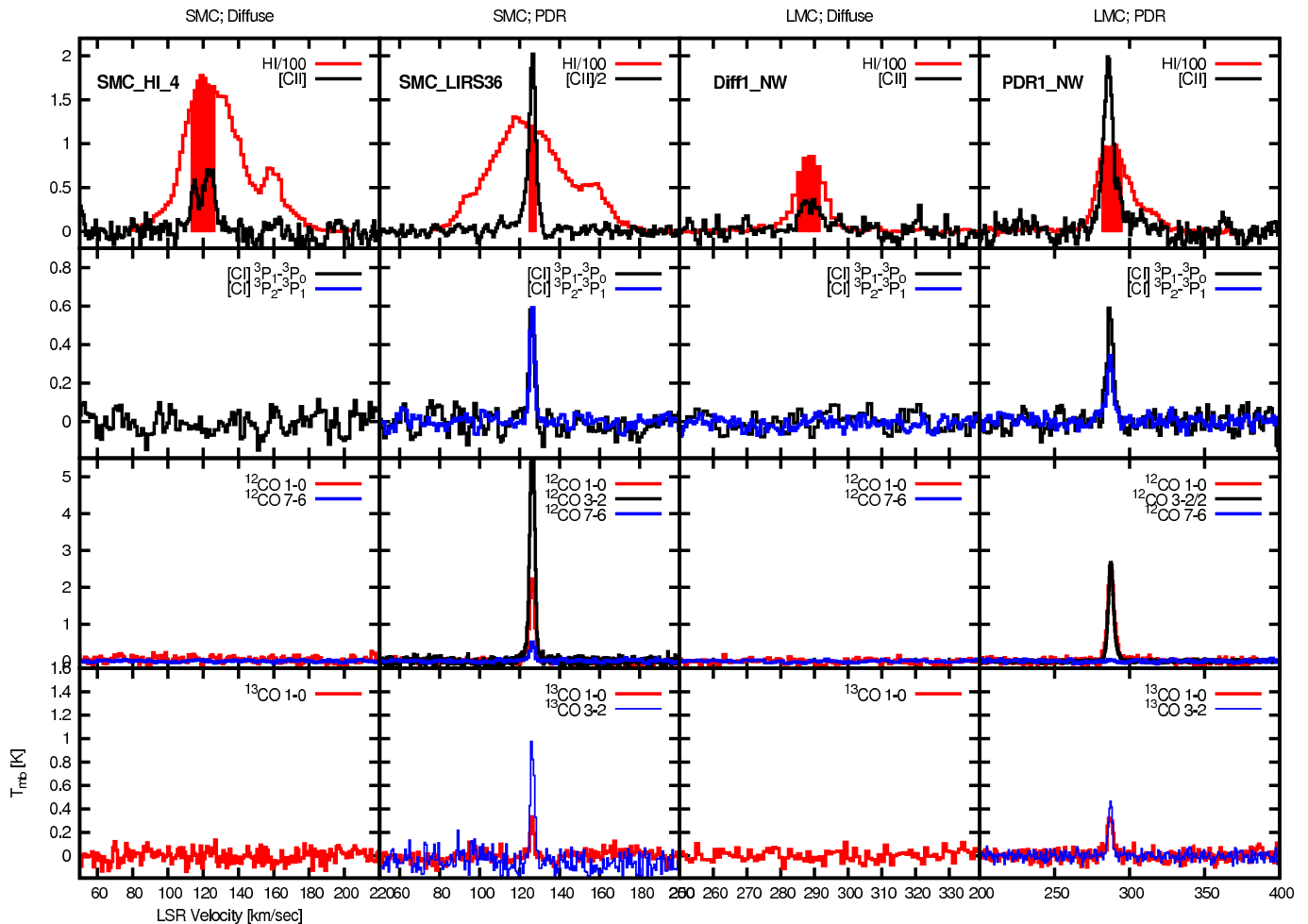


FIG. 2.— Sample spectra of ionic, atomic, and molecular species in the Large and Small Magellanic Clouds. We show examples of diffuse regions as well as of dense photon dominated regions. The shaded region in the H I spectra represents the velocity range where we assume that the H I emission is in the form of CNM (see Section 3.2).

regions (PDRs) in Figure 2. The full spectral line data set used in this paper including images of the spectra in each LOS is available as a *Herschel* User Provided Data Product<sup>2</sup>. In Table 1 and 2, we show the observational parameters in our sample, including H<sub>2</sub> column densities and molecular fractions derived in our analysis and discussed in Section 5.1. By fitting Gaussians to the observed [C II], [C I], and CO spectra we identified 49 velocity components in the LMC and 28 velocity components in the SMC. We show the integrated intensities of the spectral lines detected in our survey in Table 3 for the LMC and in Table 4 for the SMC.

Our selection of positions to sample was initially based on H I (LMC; Kim et al. 2003, SMC; Stanimirovic et al. 1999) and CO (LMC; Wong et al. 2011, SMC; Muller et al. 2010; Rubio et al. 1993) maps of the LMC and SMC. In the case of the LMC, we also used *Spitzer* 160  $\mu$ m continuum emission (Meixner et al. 2006)<sup>3</sup>. We included 7 H I peaks in both the LMC and SMC that have faint or no associated CO line emission or, in the case

of the LMC, 160  $\mu$ m continuum. These peaks represent atomic hydrogen-dominated LOSs. We also included 12 H I peaks in the LMC that are associated with 160  $\mu$ m continuum emission but are undetected in the CO maps. This sample is likely tracing clouds that are in transition from diffuse molecular to dense molecular clouds. We also included 10 CO peaks in the LMC and 7 in the SMC representing regions that have enough column density to show CO emission. They might still have a large fraction of H<sub>2</sub> gas traced by [C II] if they are clumpy and the volume filling factor of CO cores is low. Finally, our sample also includes 8 lines-of-sight in the LMC and 3 in the SMC studied in UV absorption with FUSE by Carledge et al. (2005). With these sources we have *a priori* knowledge of the H<sub>2</sub> column density, and thus they can be used to compare with our determination of the H<sub>2</sub> column densities from spectral line data.

We studied whether the physical conditions derived in our sample are representative of the average conditions in the LMC and SMC. For that purpose, we compared the ratio of the total far-infrared intensity (TIR; Section 5.4) to the H<sup>0</sup> column density (Section 3.2) as a function of the visual extinction in our sample with that derived in maps over the entire LMC and SMC. In Figure 3, we show the TIR/ $N(\text{H}^0)$  ratio as a function of  $A_V$

<sup>2</sup> <http://www.cosmos.esa.int/web/herschel/user-provided-data-products>

<sup>3</sup> The 160  $\mu$ m continuum map, used as a proxy for higher column density, warmer gas, was only available for the LMC when the sample was originally selected.

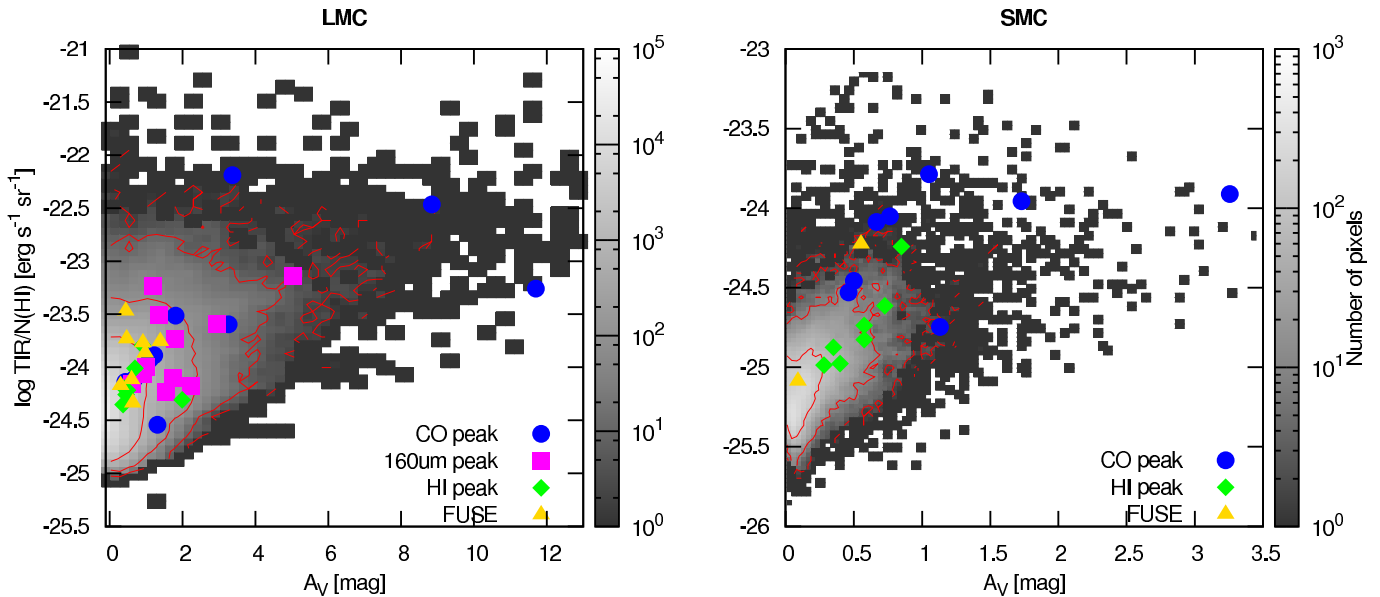


FIG. 3.— The ratio of the total far-infrared intensity (Section 5.4) to the  $H^0$  column density (Section 3.2) as a function of the visual extinction (Section 4.1) for the entire LMC and SMC. We also include data points that correspond to those in our sample in the LMC and SMC. The gray-scale represents the number of pixels at a given  $TIR/N(H^0)$  and  $A_V$  bin, with contour lines representing 2, 10, 100, and 1000 pixels.

for both the entire LMC and SMC and for the locations of our sample. The color scale in Figure 3 represents the number of pixels at a given  $TIR/N(H^0)$  and  $A_V$  bin, with contour lines representing 2, 10, 100, and 1000 pixels. The  $TIR/N(H^0)$  ratio is an approximate measure of the FUV radiation field per unit hydrogen atom, and therefore it is sensitive to how closely a LOS is associated with star formation, while the  $A_V$  is a measure of the total column density. Thus, a diffuse LOS away from star formation would be in the lower left corner of the plot, while a warm and dense photon dominated region close to newly formed stars would be in the upper right corner of the plot. The TIR and  $A_V$  maps used here were smoothed to  $60''$  to match the resolution of the HI data. The bulk of the LOSs have  $TIR/N(H^0) \simeq 10^{-25} - 10^{-23} \text{ erg s}^{-1} \text{ sr}^{-1}$  and  $A_V \lesssim 2 \text{ mag}$  in the LMC, and  $\simeq 10^{-25.5} - 10^{-24.5} \text{ erg s}^{-1} \text{ sr}^{-1}$  and  $\lesssim 0.5 \text{ mag}$  in the SMC. In the LMC, a large fraction (90%) of our sample have  $TIR/N(H^0)$  and  $A_V$  values that are similar to those of the bulk of the pixels in this galaxy. This correspondence suggests that the properties derived in our sample are representative of the average properties in the LMC. There are four LOSs that have larger  $TIR/N(H^0)$  and  $A_V$  values, corresponding to CO peaks associated with dense photon dominated regions, which represent a small volume fraction in the LMC. In the SMC, half the LOSs have conditions that are similar to the bulk of the pixels in this galaxy while the other half tend to have larger values of  $TIR/N(H^0)$  and  $A_V$ . However, most of the  $[C II]$  emission is detected in the latter half of the sample. Thus, the conditions derived in our sample in the SMC might represent those of more active regions compared with the bulk of the SMC.

## 2.2. $[C II]$ and $[C I]$ observations

We surveyed the Magellanic Clouds in the  $[C I]$   $^3P_1 - ^3P_0$ ,  $[C I]$   $^3P_2 - ^3P_1$ , and  $[C II]$   $^2P_{3/2} - ^2P_{1/2}$  fine-structure lines at 492.1607 GHz, 809.3420 GHz, and 1900.5469 GHz

(rest frequency), respectively, with the HIFI (de Graauw et al. 2010) instrument aboard the *Herschel Space Observatory* (Pilbratt et al. 2010). These observations are part of the *Herschel* Open Time 1 Project OT1\_jpineda.1. The  $^{12}CO$   $J = 7 \rightarrow 6$  (806.6518 GHz) rotational line was observed simultaneously with the  $[C I]$   $^3P_2 - ^3P_1$  line. There are 9 LOS where only the  $^{12}CO$   $J = 7 \rightarrow 6$  was observed due to an error in the frequency configuration. These LOS correspond to diffuse LOS where the  $[C I]$   $^3P_1 - ^3P_0$  line was not detected and therefore we do not expect a detection of the usually weaker  $[C I]$   $^3P_2 - ^3P_1$  line.

The  $[C II]$  1.9 THz observations were carried out with the HIFI Band 7b receiver, which employs Hot Electron Bolometer (HEB) mixers, in the LoadChop with reference observing mode. The HEB bands in HIFI show prominent electrical standing waves that are produced between the HEB mixing element and the first low noise amplifier. The standing wave shape is not a standard sinusoid and is difficult to remove from the resulting spectrum using standard fitting methods (Higgins & Kooi 2009). To remove these standing waves we used a procedure available in HIPE (Ott et al. 2006) version 12, which uses a library of standing wave shapes to find the best fit to correct the observed spectrum (see Higgins 2011 for a detailed description of this method). In HIPE we also removed residual standing waves by fitting a single sinusoidal function using the `FitHIFIFringe()` procedure. After all standing waves are removed, we exported our data to the CLASS90<sup>4</sup> data analysis software, which we used to combine the two polarization, fit the data with polynomial baselines (typically of order 3), and smooth in velocity.

The angular resolution of the  $[C II]$  observations is  $12''$ . We divided the data by a factor of 0.61 to transform the data from an antenna temperature to a main-beam

<sup>4</sup> <http://www.iram.fr/IRAMFR/GILDAS>

TABLE 1  
DERIVED PARAMETERS FOR LMC AND SMC SAMPLE

LOS	R.A	Decl.	$N(\text{H}^0)^1$ log [cm <sup>-2</sup> ]	$N(\text{H}^+)^2$ log [cm <sup>-2</sup> ]	$N(\text{H}_2)^3$ log [cm <sup>-2</sup> ]	$f(\text{H}_2)^4$	$A_V^5$ [mag]	Total far-IR <sup>6</sup> log [erg s <sup>-1</sup> cm <sup>-2</sup> sr <sup>-1</sup> ]
	J2000	J2000						
Large Magellanic Cloud								
Diff1_NW <sup>8</sup>	5:31:59.2	-66:22:52.3	21.23±0.02	20.51±0.01	–	–	0.91±0.36	-2.61±0.04
Diff2_SE <sup>8</sup>	4:59:35.5	-70:11:04.6	21.39±0.01	20.48±0.01	20.9 <sup>+0.2</sup> <sub>-0.1</sub>	0.4 <sup>+0.1</sup> <sub>-0.1</sub>	0.70±0.28	-2.70±0.04
Diff3_RIDGE <sup>8</sup>	5:31:50.6	-71:12:41.6	21.53±0.01	19.61±0.10	–	–	2.00±0.80	-2.82±0.06
Diff4_NE <sup>8</sup>	5:01:47.7	-65:59:05.2	21.39±0.01	19.85±0.06	–	–	0.38±0.15	-2.91±0.07
Diff5_SE <sup>8</sup>	4:58:54.0	-69:08:29.9	21.47±0.01	19.67±0.09	–	–	0.42±0.17	-2.78±0.05
Diff6_NW <sup>8</sup>	5:43:34.9	-67:56:08.2	21.35±0.01	20.06±0.03	–	–	0.46±0.18	-2.95±0.08
Diff7_NW <sup>8</sup>	5:25:17.3	-67:08:03.6	21.48±0.01	19.91±0.05	20.9±0.1	0.4 <sup>+0.07</sup> <sub>-0.07</sub>	0.50±0.20	-2.68±0.04
LMC10_NE <sup>9</sup>	4:51:51.1	-67:05:45.0	21.58±0.01	20.84±0.16	–	–	2.23±0.89	-2.63±0.04
LMC11_Ridge <sup>9</sup>	5:25:33.8	-69:50:16.6	21.36±0.01	19.92±0.05	21.3 <sup>+0.3</sup> <sub>-0.4</sub>	0.6 <sup>+0.2</sup> <sub>-0.2</sub>	1.21±0.48	-1.77±0.01
LMC12_SE <sup>9</sup>	5:02:13.7	-69:02:16.4	21.40±0.01	20.25±0.02	21.5 <sup>+0.2</sup> <sub>-0.5</sub>	0.7 <sup>+0.1</sup> <sub>-0.2</sub>	2.94±1.18	-1.91±0.01
LMC1_NW <sup>9</sup>	5:28:1.9	-67:25:14.0	21.43±0.01	21.14±0.00 <sup>7</sup>	21.6 <sup>+0.07</sup> <sub>-0.1</sub>	0.8 <sup>+0.07</sup> <sub>-0.07</sub>	5.05±2.02	-1.72±0.00 <sup>7</sup>
LMC2_NW <sup>9</sup>	5:25:16.3	-66:24:40.8	21.58±0.01	20.32±0.02	21.0±0.1	0.3 <sup>+0.1</sup> <sub>-0.1</sub>	0.91±0.36	-2.44±0.02
LMC3_NW <sup>9</sup>	5:20:44.8	-66:06:58.2	21.25±0.02	19.74±0.07	20.5 <sup>+0.3</sup> <sub>-0.2</sub>	0.3 <sup>+0.1</sup> <sub>-0.1</sub>	0.63±0.25	-2.85±0.06
LMC4_RIDGE <sup>9</sup>	5:28:22.5	-69:28:22.5	21.49±0.01	20.53±0.01	21.2±0.1	0.5 <sup>+0.07</sup> <sub>-0.07</sub>	1.79±0.72	-2.18±0.01
LMC5_SE <sup>9</sup>	5:06:23.1	-70:28:08.7	21.26±0.02	20.47±0.01	21.2±0.1	0.6 <sup>+0.07</sup> <sub>-0.1</sub>	1.35±0.54	-2.08±0.01
LMC7_RIDGE <sup>9</sup>	5:45:6.9	-69:50:42.6	21.74±0.01	20.49±0.01	21.2±0.1	0.4 <sup>+0.07</sup> <sub>-0.07</sub>	1.00±0.40	-2.20±0.01
LMC8_RIDGE <sup>9</sup>	5:47:11.8	-69:28:35.1	21.81±0.00 <sup>7</sup>	20.52±0.01	–	–	1.75±0.70	-2.20±0.01
LMC9_NE <sup>9</sup>	5:03:20.8	-67:11:44.2	21.61±0.01	20.17±0.03	20.5 <sup>+0.3</sup> <sub>-0.2</sub>	0.1 <sup>+0.1</sup> <sub>-0.1</sub>	1.56±0.62	-2.63±0.04
NT127 <sup>10</sup>	5:24:19.8	-70:27:48.7	21.05±0.03	19.49±0.13	21.1 <sup>+0.4</sup> <sub>-0.7</sub>	0.7 <sup>+0.2</sup> <sub>-0.2</sub>	1.23±0.49	-2.74±0.05
NT2_NE <sup>10</sup>	4:47:36.8	-67:12:13.7	21.35±0.01	–	–	–	1.32±0.53	-3.01±0.09
NT74 <sup>10</sup>	5:14:33.4	-70:10:51.9	21.33±0.01	20.87±0.15	21.4 <sup>+0.6</sup> <sub>-0.3</sub>	0.7 <sup>+0.3</sup> <sub>-0.1</sub>	1.11±0.45	-2.49±0.03
NT77 <sup>10</sup>	5:15:9.4	-70:35:42.0	21.00±0.03	20.66±0.24	21.3 <sup>+0.2</sup> <sub>-0.3</sub>	0.8 <sup>+0.1</sup> <sub>-0.1</sub>	1.82±0.73	-1.56±0.00 <sup>7</sup>
NT97 <sup>10</sup>	5:19:27.8	-71:13:52.4	21.03±0.03	19.52±0.12	–	–	0.44±0.18	-3.04±0.10
NT99 <sup>10</sup>	5:19:57.6	-70:42:21.7	21.17±0.02	20.87±0.15	–	–	0.68±0.27	-2.83±0.06
PDR1_NW <sup>10</sup>	5:25:46.9	-66:13:41.6	21.71±0.01	20.40±0.01	21.7 <sup>+0.3</sup> <sub>-0.6</sub>	0.6 <sup>+0.2</sup> <sub>-0.2</sub>	3.27±1.31	-1.93±0.01
PDR2_NW <sup>10</sup>	5:35:22.4	-67:35:00.5	21.37±0.01	21.78±0.00 <sup>7</sup>	22.2±0.1	0.9 <sup>+0.07</sup> <sub>-0.07</sub>	3.38±1.35	-0.51±0.00 <sup>7</sup>
PDR3_NE <sup>10</sup>	4:52:8.3	-66:55:13.7	21.50±0.01	21.47±0.00 <sup>7</sup>	22.5±0.1	1.0 <sup>+0.07</sup> <sub>-0.07</sub>	8.84±3.54	-0.33±0.00 <sup>7</sup>
PDR4_RIDGE <sup>10</sup>	5:39:48.7	-71:09:27.4	21.65±0.01	20.43±0.01	21.5 <sup>+0.2</sup> <sub>-0.4</sub>	0.6 <sup>+0.1</sup> <sub>-0.2</sub>	11.70±4.68	-1.42±0.00 <sup>7</sup>
SK-66D35 <sup>11</sup>	4:57:4.5	-66:34:38.0	21.49±0.01	20.64±0.00 <sup>7</sup>	21.1 <sup>+0.1</sup> <sub>-0.2</sub>	0.6 <sup>+0.3</sup> <sub>-0.1</sub>	1.40±0.56	-2.29±0.02
SK-67D2 <sup>11</sup>	4:47:4.4	-67:06:53.0	21.31±0.01	20.13±0.03	–	–	0.31±0.12	-2.61±0.04
SK-68D129 <sup>11</sup>	5:36:26.8	-68:57:32.0	21.55±0.01	20.66±0.00 <sup>7</sup>	–	–	0.98±0.39	-2.34±0.02
SK-68D140 <sup>11</sup>	5:38:57.3	-68:56:53.0	21.69±0.01	21.20±0.00 <sup>7</sup>	21.0±0.1	0.3 <sup>+0.1</sup> <sub>-0.1</sub>	0.45±0.18	-1.63±0.00 <sup>7</sup>
SK-68D155 <sup>11</sup>	5:42:54.9	-68:56:54.0	21.76±0.01	20.81±0.00 <sup>7</sup>	21.4±0.0	0.5 <sup>+0.07</sup> <sub>-0.07</sub>	0.92±0.37	-1.77±0.01
SK-68D26 <sup>11</sup>	5:01:32.2	-68:10:43.0	21.24±0.02	19.91±0.05	–	–	0.61±0.24	-2.86±0.06
SK-69D228 <sup>11</sup>	5:37:9.2	-69:20:20.0	21.52±0.01	20.85±0.00 <sup>7</sup>	20.9±0.1	0.3 <sup>+0.1</sup> <sub>-0.1</sub>	0.48±0.19	-2.17±0.01
SK-69D279 <sup>11</sup>	5:41:44.7	-69:35:15.0	21.62±0.01	20.41±0.01	–	–	0.64±0.26	-2.61±0.04

<sup>1</sup> H<sup>0</sup> column density derived from the integrated intensity of the H I 21 cm line over the full velocity range (see Section 3.2).

<sup>2</sup> H<sup>+</sup> column density derived from H $\alpha$  observations as described in Section 3.1.

<sup>3</sup> H<sub>2</sub> column density derived from [C II], [C I], and CO observations as described in Section 5.1.

<sup>4</sup> Molecular fraction,  $f(\text{H}_2) = 2N(\text{H}_2)/(N(\text{H}^0) + 2N(\text{H}_2))$  (Section 5.1).

<sup>5</sup> Visual extinction derived from dust continuum maps as described in Section 4.1.

<sup>6</sup> Total far-infrared intensity derived from Spitzer 24  $\mu\text{m}$  and *Herschel* 100  $\mu\text{m}$  maps as described in Section 5.4.

<sup>7</sup> The uncertainty is below 0.005 or 0.05.

<sup>8</sup> H I Peak (See Section 2).

<sup>9</sup> 160  $\mu\text{m}$  Peak (See Section 2).

<sup>10</sup> CO Peak (See Section 2).

<sup>11</sup> FUSE LOSs (See Section 2).



TABLE 2  
DERIVED PARAMETERS FOR LMC AND SMC SAMPLE

LOS	R.A.	Decl.	$N(\text{H}^0)^1$	$N(\text{H}^+)^2$	$N(\text{H}_2)^3$	$f(\text{H}_2)^4$	$A_V^5$	Total far-IR <sup>6</sup>
	J2000	J2000	$\log$ [cm <sup>-2</sup> ]	$\log$ [cm <sup>-2</sup> ]	$\log$ [cm <sup>-2</sup> ]		[mag]	$\log$ [erg s <sup>-1</sup> cm <sup>-2</sup> sr <sup>-1</sup> ]
Small Magellanic Cloud								
AzV18 <sup>11</sup>	0:47:13.1	-73:06:25.0	22.10±0.00 <sup>7</sup>	20.54±0.00 <sup>7</sup>	21.9±0.1	0.5 <sup>+0.1</sup> <sub>-0.07</sub>	0.55±0.22	-1.88±0.01
AzV456 <sup>11</sup>	1:10:55.8	-72:42:55.0	21.64±0.00 <sup>7</sup>	20.52±0.01	–	–	0.09±0.04	-3.15±0.12
AzV462 <sup>11</sup>	1:11:25.9	-72:32:21.0	21.62±0.00 <sup>7</sup>	19.77±0.07	–	–	0.00±0.00 <sup>7</sup>	-3.54±0.30
SMC_HL1 <sup>8</sup>	0:58:40.5	-72:34:52.4	21.99±0.00 <sup>7</sup>	20.10±0.03	–	–	0.28±0.11	-3.04±0.10
SMC_HL2 <sup>8</sup>	0:57:35.7	-72:48:56.3	21.99±0.00 <sup>7</sup>	20.11±0.03	–	–	0.40±0.16	-2.98±0.08
SMC_HL3 <sup>8</sup>	0:53:2.0	-73:15:27.9	22.02±0.00 <sup>7</sup>	20.27±0.02	–	–	0.58±0.23	-2.82±0.06
SMC_HL4 <sup>8</sup>	0:48:41.5	-73:06:08.3	22.13±0.00 <sup>7</sup>	20.36±0.01	21.8±0.1	0.5 <sup>+0.07</sup> <sub>-0.07</sub>	0.85±0.34	-2.11±0.01
SMC_HL5 <sup>8</sup>	0:47:20.4	-73:18:28.4	22.05±0.00 <sup>7</sup>	20.63±0.01	–	–	0.73±0.29	-2.73±0.05
SMC_HL6 <sup>8</sup>	0:49:53.2	-72:56:15.6	22.05±0.00 <sup>7</sup>	20.48±0.01	–	–	0.58±0.23	-2.76±0.05
SMC_HL7 <sup>8</sup>	0:49:38.1	-73:01:14.2	22.06±0.00 <sup>7</sup>	20.16±0.03	–	–	0.35±0.14	-2.80±0.06
SMC_B2.6 <sup>10</sup>	0:47:57.2	-73:17:16.4	22.00±0.00 <sup>7</sup>	20.98±0.00 <sup>7</sup>	22.2±0.1	0.7 <sup>+0.07</sup> <sub>-0.07</sub>	0.48±0.19	-1.79±0.01
SMC_LIRS36 <sup>10</sup>	0:46:40.3	-73:06:10.5	22.04±0.00 <sup>7</sup>	20.96±0.00 <sup>7</sup>	22.2±0.2	0.7 <sup>+0.1</sup> <sub>-0.1</sub>	0.60±0.24	-1.53±0.00 <sup>7</sup>
SMC_LIRS49 <sup>10</sup>	0:48:21.1	-73:05:29.0	22.12±0.00 <sup>7</sup>	20.53±0.00 <sup>7</sup>	22.5 <sup>+0.1</sup> <sub>-0.2</sub>	0.8 <sup>+0.07</sup> <sub>-0.1</sub>	0.90±0.36	-1.69±0.00 <sup>7</sup>
SMC_NE_1a <sup>10</sup>	0:59:43.8	-71:44:47.0	21.60±0.00 <sup>7</sup>	20.23±0.02	21.5 <sup>+0.1</sup> <sub>-0.2</sub>	0.6 <sup>+0.1</sup> <sub>-0.1</sub>	0.41±0.16	-2.38±0.02
SMC_NE_3c <sup>10</sup>	1:03:30.0	-71:57:00.0	21.78±0.00 <sup>7</sup>	20.48±0.01	21.5 <sup>+0.3</sup> <sub>-0.8</sub>	0.5 <sup>+0.2</sup> <sub>-0.1</sub>	0.46±0.19	-2.70±0.04
SMC_NE_3g <sup>10</sup>	1:03:9.9	-72:03:46.9	21.79±0.00 <sup>7</sup>	20.84±0.00 <sup>7</sup>	21.4 <sup>+0.1</sup> <sub>-0.2</sub>	0.5 <sup>+0.1</sup> <sub>-0.1</sub>	0.82±0.33	-2.29±0.02
SMC_NE_4a_hi <sup>10</sup>	0:57:0.0	-72:22:40.0	21.86±0.00 <sup>7</sup>	20.21±0.02	22.1 <sup>+0.6</sup> <sub>-1.9</sub>	0.8 <sup>+0.3</sup> <sub>-0.2</sub>	1.13±0.45	-2.77±0.05
SMC_NE_4c_low <sup>10</sup>	0:58:40.0	-72:27:40.0	21.93±0.00 <sup>7</sup>	20.39±0.02	22.2±0.7	0.8 <sup>+0.4</sup> <sub>-0.2</sub>	0.67±0.27	-2.63±0.04

<sup>1</sup> H<sup>0</sup> column density derived from the integrated intensity of the H I 21 cm line over the full velocity range (see Section 3.2).

<sup>2</sup> H<sup>+</sup> column density derived from H $\alpha$  observations as described in Section 3.1.

<sup>3</sup> H<sub>2</sub> column density derived from [C II], [C I], and CO observations as described in Section 5.1.

<sup>4</sup> Molecular fraction,  $f(\text{H}_2) = 2N(\text{H}_2)/(N(\text{H}^0) + 2N(\text{H}_2))$  (Section 5.1).

<sup>5</sup> Visual extinction derived from dust continuum maps as described in Section 4.1.

<sup>6</sup> Total far-infrared intensity derived from Spitzer 24  $\mu\text{m}$  and *Herschel* 100  $\mu\text{m}$  maps as described in Section 5.4.

<sup>7</sup> The uncertainty is below 0.005 or 0.05.

<sup>8</sup> H I Peak (See Section 2).

<sup>9</sup> 160  $\mu\text{m}$  Peak (See Section 2).

<sup>10</sup> CO Peak (See Section 2).

<sup>11</sup> FUSE LOSs (See Section 2).

TABLE 3  
INTEGRATED INTENSITIES OF SPECTRAL LINE FOR LMC SAMPLE

LOS	$V_{\text{LSR}}$ [km s <sup>-1</sup> ]	$I_{\text{[HI]};\text{CNM}}^1$	$I_{\text{[CII]}}$	$I_{\text{[CI]}(1-0)}$	$I_{\text{[CI]}(2-1)}$	$I_{\text{CO}(1-0)}$ [K km s <sup>-1</sup> ]	$I_{\text{CO}(3-2)}$	$I_{\text{CO}(7-6)}$	$I_{^{13}\text{CO}(1-0)}$	$I_{^{13}\text{CO}(3-2)}$
Large Magellanic Cloud										
Diff1_NW_1	288.8	510±8	2.4±0.3	–	–	–	–	–	–	–
Diff2_SE_1	233.3	169±6	2.8±0.6	0.9±0.3	–	–	–	–	–	–
Diff3_RIDGE_1	–	–	–	–	–	0.7±0.2	–	–	–	–
Diff5_SE_1	245.0	405±7	0.9±0.2	–	–	–	–	–	–	–
Diff6_NW_1	–	–	–	–	–	1.0±0.1	0.3±0.1	–	–	–
Diff7_NW_1	288.1	253±6	2.7±0.2	–	–	–	–	–	–	–
LMC10_NE_1	275.4	496±7	1.8±0.2	0.3±0.1	–	1.7±0.2	–	–	–	–
LMC11_Ridge_1	250.3	341±7	7.9±0.1	0.6±0.1	0.4±0.1	4.1±0.2	3.4±0.1	–	–	0.3±0.1
LMC12_SE_1	265.7	224±6	6.4±0.2	0.1±0.1	–	1.9±0.2	2.8±0.1	–	–	0.2±0.1
LMC12_SE_2	270.6	288±6	5.3±0.2	1.1±0.1	0.9±0.1	4.7±0.2	7.4±0.1	–	0.4±0.1	0.5±0.1
LMC1_NW_1	293.1	288±7	6.6±0.0 <sup>2</sup>	0.6±0.1	0.4±0.0 <sup>2</sup>	1.8±0.3	1.3±0.2	1.5±0.1	–	0.3±0.0 <sup>2</sup>
LMC1_NW_2	287.6	341±7	6.1±0.0 <sup>2</sup>	0.9±0.1	0.6±0.1	2.3±0.3	2.5±0.3	0.4±0.1	–	0.3±0.1
LMC1_NW_3	288.0	890±12	10.1±0.0 <sup>2</sup>	–	–	–	–	–	–	–
LMC2_NW_1	290.5	716±8	4.7±0.4	0.5±0.1	0.4±0.1	2.3±0.2	–	–	–	–
LMC3_NW_1	289.7	257±6	1.6±0.3	–	–	–	–	–	–	–
LMC4_RIDGE_1	246.6	618±9	5.7±0.3	–	–	0.6±0.2	–	–	–	–
LMC5_SE_1	219.0	75±4	9.7±0.1	0.7±0.1	0.8±0.2	2.5±0.2	3.2±0.1	–	–	0.4±0.1
LMC7_RIDGE_1	232.7	745±9	6.2±0.5	–	–	1.9±0.2	0.5±0.2	–	–	–
LMC8_RIDGE_1	238.5	688±9	3.7±0.4	–	–	–	–	–	–	–
LMC9_NE_1	274.2	310±7	2.0±0.3	–	–	3.3±0.3	1.3±0.1	–	–	–
NT127_1	235.0	73±4	0.6±0.1	1.1±0.1	0.2±0.0 <sup>2</sup>	3.7±0.2	4.2±0.1	–	–	0.3±0.1
NT2_NE_1	–	–	–	1.2±0.2	–	8.2±0.2	–	–	0.9±0.1	–
NT74_1	236.1	310±8	1.6±0.4	2.6±0.1	0.5±0.1	17.1±0.3	11.0±0.1	–	2.5±0.2	0.6±0.1
NT77_1	217.4	59±4	8.3±0.1	1.0±0.2	1.0±0.1	8.1±0.2	15.5±0.1	1.1±0.1	1.5±0.1	2.7±0.1
NT97_1	–	–	–	0.4±0.1	–	3.8±0.1	–	–	0.7±0.1	–
NT99_1	227.0	270±7	1.3±0.3	–	–	5.0±0.1	–	–	0.6±0.1	–
PDR1_NW_1	285.8	775±9	13.7±0.3	3.1±0.2	1.7±0.1	13.6±0.2	23.0±0.1	–	1.6±0.1	1.6±0.1
PDR1_NW_2	293.3	287±6	1.0±0.2	–	–	–	–	–	–	–
PDR2_NW_1	291.4	184±7	3.1±0.2	–	0.4±0.0 <sup>2</sup>	2.1±0.5	3.9±0.1	1.5±0.1	–	–
PDR2_NW_2	284.3	144±7	47.0±0.3	0.8±0.1	1.8±0.1	7.1±0.6	11.8±0.1	5.9±0.2	–	1.0±0.2
PDR2_NW_3	279.6	203±8	21.0±0.2	1.2±0.1	0.5±0.0 <sup>2</sup>	4.2±0.3	2.8±0.1	–	–	–
PDR2_NW_4	301.4	173±11	13.6±0.5	–	–	–	–	–	–	–
PDR3_NE_1	275.8	737±9	42.7±1.4	0.9±0.4	0.4±0.1	3.7±0.5	14.7±0.3	5.0±0.2	0.3±0.3	2.6±0.1
PDR3_NE_2	271.4	391±7	34.1±0.2	2.5±0.4	4.0±0.1	15.1±0.5	32.0±0.3	7.6±0.2	2.1±0.3	5.3±0.0 <sup>2</sup>
PDR3_NE_3	276.6	1370±13	36.6±1.4	–	–	–	–	–	–	–
PDR4_RIDGE_1	228.0	602±9	9.3±0.1	4.2±0.2	2.2±0.1	33.9±0.3	34.2±0.1	2.4±0.1	5.4±0.2	4.0±0.1
SK-66D35_1	–	–	–	1.0±0.3	0.3±0.1	0.7±0.1	2.0±0.1	0.5±0.1	–	0.3±0.0 <sup>2</sup>
SK-66D35_2	279.5	584±9	5.9±0.4	–	–	–	0.4±0.1	–	–	–
SK-67D2_1	–	–	–	–	–	0.7±0.1	0.3±0.0 <sup>2</sup>	–	–	–
SK-68D129_1	259.0	708±10	2.2±0.5	–	–	0.6±0.2	–	–	–	–
SK-68D140_1	250.0	635±9	7.0±0.6	–	–	–	–	–	–	–
SK-68D140_2	273.9	809±14	6.2±1.5	–	–	–	–	–	–	–
SK-68D140_3	262.0	590±9	5.4±1.2	–	–	–	–	–	–	–
SK-68D155_1	246.1	383±8	8.0±0.5	–	–	–	–	–	–	–
SK-68D155_2	256.6	374±7	1.8±0.4	–	–	–	–	–	–	–
SK-68D26_1	251.3	476±9	2.2±0.5	–	–	–	–	–	–	–
SK-69D228_1	247.0	314±9	6.1±0.3	–	–	–	–	–	–	–

<sup>1</sup> H I intensity integrated over a velocity range defined by the FWHM of the observed [C II] line (Section 3.2).

<sup>2</sup> Error below 0.05.

temperature scale<sup>5</sup>. The data were produced by the wide band spectrometer (WBS), which has a channel width of 1 MHz (0.16 km s<sup>-1</sup> at 1.9 THz). We later smoothed the data to a resolution of 0.8 km s<sup>-1</sup>. For this resolution the average rms noise of our data is<sup>6</sup> 0.1 K.

We observed the [C I] <sup>3</sup>P<sub>1</sub>–<sup>3</sup>P<sub>0</sub> line using HIFI Band

<sup>5</sup> The beam efficiencies of all HIFI bands are presented in [http://herschel.esac.esa.int/twiki/pub/Public/HifiCalibrationWeb/HifiBeamReleaseNote\\_Sep2014.pdf](http://herschel.esac.esa.int/twiki/pub/Public/HifiCalibrationWeb/HifiBeamReleaseNote_Sep2014.pdf)

<sup>6</sup> For the typical [C II] FWHM line width of about 3 km s<sup>-1</sup>, this sensitivity limit corresponds to 1.1 × 10<sup>-6</sup> erg s<sup>-1</sup> cm<sup>-2</sup> sr<sup>-1</sup>. The integrated intensity in units of K km s<sup>-1</sup> can be converted that in units of erg s<sup>-1</sup> cm<sup>-2</sup> sr<sup>-1</sup> using  $I[\text{K km s}^{-1}] = 1.43 \times 10^5 I[\text{erg s}^{-1} \text{cm}^{-2} \text{sr}^{-1}]$  (Goldsmith et al. 2012).

1, while the [C I] <sup>3</sup>P<sub>2</sub>–<sup>3</sup>P<sub>1</sub> and <sup>12</sup>CO  $J = 7 \rightarrow 6$  lines were observed simultaneously using HIFI Band 3. The angular resolutions are 44'' and 26.5'' for Bands 1 and 3, respectively. We applied main-beam efficiencies of 0.651 and 0.645, respectively, to convert these data from an antenna temperature to a main-beam temperature scale. The typical rms noise for the [C I] <sup>3</sup>P<sub>1</sub>–<sup>3</sup>P<sub>0</sub> line was 0.035 K in a 0.91 km s<sup>-1</sup> channel width. For the [C I] <sup>3</sup>P<sub>2</sub>–<sup>3</sup>P<sub>1</sub> and <sup>12</sup>CO  $J = 7 \rightarrow 6$  lines the typical rms noise was 0.02 K in a 1.1 km s<sup>-1</sup> channel width.

### 2.3. CO observations

To complement the *Herschel* data, we observed the  $J = 1 \rightarrow 0$  transitions of <sup>12</sup>CO, <sup>13</sup>CO, and C<sup>18</sup>O with



TABLE 4  
INTEGRATED INTENSITIES OF SPECTRAL LINE FOR SMC SAMPLE

LOS	$V_{\text{LSR}}$ [km s <sup>-1</sup> ]	$I_{[\text{HI}];\text{CNM}}^1$	$I_{[\text{CII}]}$	$I_{[\text{CI}](1-0)}$	$I_{[\text{CI}](2-1)}$	$I_{\text{CO}(1-0)}$ [K km s <sup>-1</sup> ]	$I_{\text{CO}(3-2)}$	$I_{\text{CO}(7-6)}$	$I_{^{13}\text{CO}(1-0)}$	$I_{^{13}\text{CO}(3-2)}$
Small Magellanic Cloud										
AzV18.1	122.0	1709±11	5.9±0.6	–	–	–	–	–	–	–
AzV18.2	136.7	764±8	3.4±0.5	–	–	–	–	–	–	–
SMC_B2.6.1	120.9	731±4	15.6±0.4	0.9±0.1	0.8±0.1	5.5±0.2	5.6±0.1	0.8±0.1	0.8±0.1	0.7±0.1
SMC_B2.6.2	125.3	1273±5	5.3±0.4	–	–	–	–	–	–	–
SMC_HI.2.1	–	–	–	0.7±0.2	–	–	–	–	–	–
SMC_HI.3.1	145.4	2347±8	4.4±0.8	0.6±0.1	–	–	–	0.4±0.1	–	–
SMC_HI.4.1	123.3	1103±4	5.5±0.4	–	–	–	–	–	–	–
SMC_HI.4.2	114.8	508±3	2.3±0.3	–	–	–	–	–	–	–
SMC_HI.6.1	149.7	431±4	1.3±0.3	–	–	–	–	–	–	–
SMC_LIRS36.1	126.4	383±3	16.4±0.1	2.0±0.1	1.8±0.1	7.6±0.2	18.9±0.1	1.5±0.1	0.7±0.1	2.8±0.2
SMC_LIRS36.2	–	–	–	–	–	0.5±0.1	–	–	–	–
SMC_LIRS49.1	110.4	448±3	5.6±0.0 <sup>2</sup>	–	–	–	0.8±0.1	–	–	–
SMC_LIRS49.2	115.0	502±3	14.3±0.0 <sup>2</sup>	2.5±0.2	1.3±0.1	8.6±0.2	18.1±0.1	0.6±0.1	0.6±0.1	2.0±0.2
SMC_LIRS49.3	125.9	1173±5	5.2±0.0 <sup>2</sup>	–	–	1.3±0.2	2.4±0.1	–	–	0.3±0.1
SMC_LIRS49.4	137.2	191±2	1.4±0.0 <sup>2</sup>	–	–	–	–	–	–	–
SMC_NE.1a.1	148.9	496±4	4.5±0.1	0.5±0.1	0.5±0.1	4.0±0.1	4.3±0.1	0.6±0.1	0.4±0.0 <sup>2</sup>	–
SMC_NE.3c.1	175.1	170±2	1.1±0.1	1.2±0.1	0.7±0.1	4.2±0.2	4.1±0.1	–	0.7±0.0 <sup>2</sup>	0.4±0.1
SMC_NE.3g.1	169.1	690±4	4.0±0.1	0.6±0.2	0.6±0.1	4.3±0.1	3.2±0.1	0.5±0.1	0.4±0.0 <sup>2</sup>	0.5±0.1
SMC_NE.4a_hi.1	–	–	–	–	–	–	0.7±0.1	–	–	0.2±0.1
SMC_NE.4a_hi.2	153.9	131±2	1.6±0.2	0.5±0.1	–	3.1±0.1	2.1±0.1	–	0.2±0.0 <sup>2</sup>	–
SMC_NE.4a_hi.3	122.2	551±4	1.3±0.3	–	–	–	–	–	–	–
SMC_NE.4c_low.1	121.6	780±4	2.1±0.4	0.7±0.1	–	5.8±0.1	1.7±0.1	0.2±0.1	0.7±0.0 <sup>2</sup>	–

<sup>1</sup> H I intensity integrated over a velocity range defined by the FWHM of the observed [C II] line (Section 3.2).

<sup>2</sup> Error below 0.05.

the ATNF Mopra<sup>7</sup> Telescope (project M580). The Mopra 22m telescope has an angular resolution of 33'' at 115 GHz. Typical system temperatures were 600, 300, and 250 K for <sup>12</sup>CO, <sup>13</sup>CO, and C<sup>18</sup>O, respectively. To convert from antenna to main-beam temperature scale, we used a main-beam efficiency of 0.42 (Ladd et al. 2005). All lines were observed simultaneously with the MOPS spectrometer in zoom mode. The spectra were smoothed in velocity to 0.87 km s<sup>-1</sup> for <sup>12</sup>CO and to 0.91 km s<sup>-1</sup> for <sup>13</sup>CO. The typical rms noise is 0.06 K for <sup>12</sup>CO and 0.05 K for <sup>13</sup>CO. The C<sup>18</sup>O line was detected only in a small number of LOSs, and we will not use these observations in the present analysis. We checked pointing accuracy every 60 minutes using a nearby SiO maser.

We used the APEX<sup>8</sup> 12m telescope (Güsten et al. 2006) to observe the <sup>12</sup>CO  $J = 3 \rightarrow 2$  and <sup>13</sup>CO  $J = 3 \rightarrow 2$  lines in 25 LOS in the LMC and SMC that have been detected in our low- $J$  observations (project M0036.93). The angular resolution of the APEX telescope is 17.5'' at 345 GHz. We converted from antenna to main-beam temperature scale using an efficiency of 0.69 for 345 GHz. The typical rms noise in the <sup>12</sup>CO  $J = 3 \rightarrow 2$  data is 0.08 K for a 0.33 km s<sup>-1</sup> channel width and in the <sup>13</sup>CO  $J = 3 \rightarrow 2$  data is 0.05 K for a 0.33 km s<sup>-1</sup> channel width.

#### 2.4. H I, H $\alpha$ , H66 $\alpha$ , and Dust Continuum data

<sup>7</sup> The Mopra radio telescope is part of the Australia Telescope which is funded by the Commonwealth of Australia for operation as a National Facility managed by CSIRO.

<sup>8</sup> This publication is based in part on data acquired with the Atacama Pathfinder Experiment (APEX). APEX is a collaboration between the Max-Planck-Institut für Radioastronomie, the European Southern Observatory, and the Onsala Space Observatory

We used the H I 21 cm maps of the entire LMC and SMC presented by Kim et al. (2003) and Stanimirovic et al. (1999) (see also Staveley-Smith et al. 2003), respectively. These maps of the Magellanic clouds were made by combining interferometric (ATCA) and single dish (Parkes) observations. The map of the LMC has an angular resolution of 60'', corresponding to a spatial resolution of 15 pc, while the SMC map has an angular resolution of 98'' corresponding to a spatial scale of 29 pc. The rms noise in the LMC map is 2.4 K in a 1.65 km s<sup>-1</sup> channel width and in the SMC map is 1.3 K over a 1.65 km s<sup>-1</sup> channel width.

To estimate the contribution to the [C II] emission from ionized gas, we used the H $\alpha$  map from Southern H-alpha Sky Survey Atlas survey (SHASSA; Gaustad et al. 2001). The SHASSA maps cover the entire LMC and SMC with an angular resolution of 48'' and a sensitivity level of 0.5 Rayleigh ( $R=10^6/4\pi$  photons cm<sup>-2</sup> s<sup>-1</sup> sr<sup>-1</sup>). We also used the NASA 70-m Deep Space Network telescope (DSS-43) to observe the H66 $\alpha$  hydrogen radio recombination line at 22.364 GHz in one of our sources with the aim to test the effect of dust extinction on the H $\alpha$  observations. The angular resolution of the DSS-43 at 22.364 GHz is 48''. We converted the data from an antenna temperature to a main beam temperature scale using a main-beam efficiency of 0.50. The H66 $\alpha$  spectrum has a rms noise of 5.4 mK in a 3.5 km s<sup>-1</sup> channel width.

We also compared our *Herschel* spectral line observations with dust continuum maps of the LMC and SMC taken using the PACS and SPIRE instruments on *Herschel*. These maps are part of the HERITAGE survey (Meixner et al. 2013) which provides images

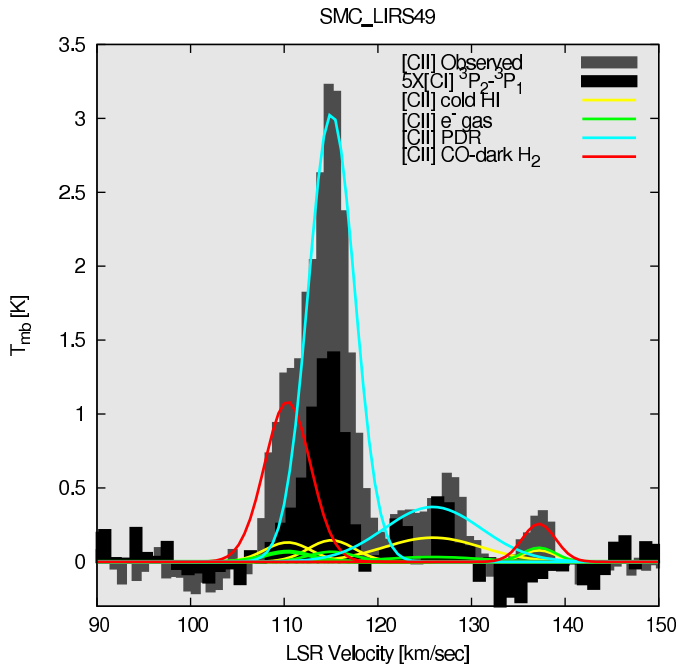


FIG. 4.— Sample [C II] and [C I]  $^3P_2-^3P_1$  spectrum illustrating the decomposition between [C II] emission associated with PDRs, CO-dark  $H_2$  gas, cold H I, and ionized gas. See Section 3 for details on the decomposition of the [C II] emission.

at  $100 \mu\text{m}$ ,  $160 \mu\text{m}$  (PACS),  $250 \mu\text{m}$ , and  $350 \mu\text{m}$ , and  $500 \mu\text{m}$  (SPIRE). The angular resolution of these maps are  $7.7''$  ( $100 \mu\text{m}$ ),  $12''$  ( $160 \mu\text{m}$ ),  $18''$  ( $250 \mu\text{m}$ ),  $25''$  ( $350 \mu\text{m}$ ), and  $40''$  ( $500 \mu\text{m}$ ). The foreground dust emission originating from the Milky Way was subtracted using a linear baseline (Meixner et al. 2013). We also used the *Spitzer*  $24 \mu\text{m}$  MIPS maps observed as part of the SAGE survey (Meixner et al. 2006) and has an angular resolution of  $6''$ .

### 2.5. Angular Resolution

The analysis presented in this paper uses a multi-wavelength data set from different telescopes. Therefore, the angular resolution of the observations is not uniform. While maps can be convolved to a uniform resolution, this is not the case for pointed [C II], [C I], and CO observations, with angular resolutions ranging from  $12''$  for [C II] and  $60''$  for H I. Therefore, absolute intensities and line ratios used in our analysis can be affected by beam dilution effects.

We studied the effect of beam dilution in our observations by smoothing the  $12''$  angular resolution  $160 \mu\text{m}$  HERITAGE dust continuum map, which is assumed to be a proxy for the distribution of gas in the LMC and SMC. We then compared the resulting intensities at different angular resolutions. In the case of ionized gas traced by  $H\alpha$  observations, we used the *Spitzer*  $24 \mu\text{m}$  images of the Magellanic clouds which is a proxy for hot dust emission associated with ionized gas. Details of this study are presented in Appendix A. The effects of beam dilution in our results will be discussed as they are presented throughout the paper. In general, we find that beam dilution has a minor effect in our results for most of our sample, with the exception of a handful of point-like, unresolved PDR sources. Note that the data used in our analysis is not corrected for beam dilution effects,

due to the uncertainty on whether the  $24 \mu\text{m}$  or  $160 \mu\text{m}$  are good tracers of the ionized and neutral gas components, respectively.

## 3. THE ORIGIN OF THE [C II] EMISSION IN THE MAGELLANIC CLOUDS

The observed [C II] emission arises from gas associated with hydrogen in the form of  $H^0$ ,  $H_2$ , and  $H^+$ . In the latter gas component, the collisions are mainly with electrons due to their higher speeds, so we refer to it as  $e^-$  gas. Thus, the observed [C II] emission is given by,

$$I_{[\text{C II}]} = I_{[\text{C II}]^{\text{H}^0}} + I_{[\text{C II}]^{\text{H}_2}} + I_{[\text{C II}]^{\text{e}^-}}. \quad (1)$$

For optically thin emission, the [C II] intensity (in units of  $\text{K km s}^{-1}$ ) is related to the  $\text{C}^+$  column density,  $N_{\text{C}^+}$  ( $\text{cm}^{-2}$ ), and volume density of the collisional partner (assumed to be uniform along the line of sight),  $n$  ( $e^-$ ,  $H^0$ , or  $H_2$ ;  $\text{cm}^{-3}$ ), as (see e.g. Goldsmith et al. 2012)

$$I_{[\text{C II}]} = N_{\text{C}^+} \left[ 3.05 \times 10^{15} \left( 1 + 0.5 \left( 1 + \frac{A_{ul}}{R_{ul}n} \right) e^{\frac{91.21}{T_{\text{kin}}}} \right) \right]^{-1}, \quad (2)$$

where  $A_{ul} = 2.3 \times 10^{-6} \text{ s}^{-1}$  is the Einstein spontaneous decay rate and  $R_{ul}$  is the collisional de-excitation rate coefficient at a kinetic temperature  $T_{\text{kin}}$ , with  $u$  and  $l$  denoting the upper and lower energy levels. Values of  $R_{ul}$  for collisions with  $H^0$ ,  $H_2$ , and  $e^-$  as a function of the kinetic temperature are available from Barinovs et al. (2005), Wiesenfeld & Goldsmith (2014), and Wilson & Bell (2002), respectively. For example, at  $T_{\text{kin}} = 100 \text{ K}$ ,  $R_{ul} = 7.58 \times 10^{-10}$  and  $5.12 \times 10^{-10} \text{ cm}^3 \text{ s}^{-1}$  for collisions with atomic and molecular hydrogen<sup>9</sup>, respectively, while at  $T_{\text{kin}} = 8000 \text{ K}$ ,  $R_{ul} = 5.2 \times 10^{-8} \text{ cm}^3 \text{ s}^{-1}$  for collisions with electrons.

Dufour et al. (1982) studied the carbon abundance in H II regions in the Magellanic clouds deriving  $12 + \log(\text{C}/\text{H}) = 7.9$  for the LMC and  $12 + \log(\text{C}/\text{H}) = 7.16$  for the SMC. Relative to the gas-phase carbon fractional abundance of  $[\text{C}/\text{H}] = 1.4 \times 10^{-4}$  determined in the Milky Way (Sofia et al. 1997), the carbon abundances in the LMC and SMC are 1.8 and 10 times lower, respectively. We used the fractional carbon abundances derived by Dufour et al. (1982) in the analysis presented here.

In the following we study the relative contribution to the observed [C II] emission from ionized, atomic, and molecular gas. In Figure 4 we show an example of the decomposition of the [C II] emission originating from different ISM components. The derived [C II] emission fractions as a function of the observed [C II] intensity for the entire sample are summarized in Figure 5.

### 3.1. Ionized gas

We estimated the [C II] intensity originating from ionized gas ( $e^-$  gas) using the Southern H-alpha Sky Survey Atlas survey (SHASSA; Gaustad et al. 2001)  $H\alpha$  emission maps of the LMC and SMC. A commonly defined

<sup>9</sup> Assuming an ortho-to-para  $H_2$  ratio, OPR=1. See discussion in Wiesenfeld & Goldsmith (2014).

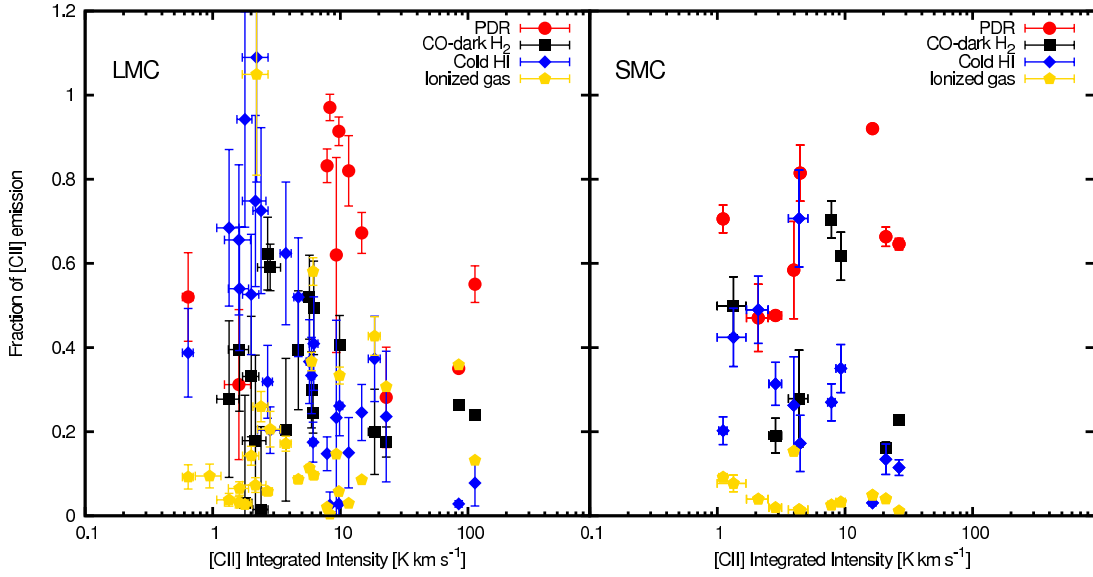


FIG. 5.— The fraction of the [C II] emission that we estimate arises from ionized gas, cold atomic gas, CO–dark H<sub>2</sub>, and photon dominated regions (PDRs) as a function of the observed [C II] emission in the LMC and SMC.

quantity used to relate the properties of the ionized gas and the observed H $\alpha$  emission is the emission measure (EM), defined as the integral of the electron volume density squared along the line of sight,

$$EM = \int n_e^2 dl. \quad (3)$$

Assuming that the electron density is constant along the line of sight, this equation can be simplified to

$$EM = \langle n_e \rangle N_e \simeq \langle n_e \rangle N_{\text{H}^+}. \quad (4)$$

The emission measure is related to the intensity of the H $\alpha$  line, in units of Rayleigh (R), as (e.g. Reynolds 1991)

$$\left( \frac{EM}{\text{pc cm}^{-6}} \right) = 2.75 \left( \frac{T_{\text{kin}}}{10^4 \text{ K}} \right)^{0.9} \left( \frac{I_{\text{H}\alpha}}{\text{R}} \right). \quad (5)$$

The critical density,  $n_{\text{cr}} \equiv A_{\text{ul}}/R_{\text{ul}}$ , is the density at which the collisional de-excitation rate is equal to the effective spontaneous decay rate, and for collisions of C<sup>+</sup> with electrons at  $T_{\text{kin}} = 8000 \text{ K}$  is equal to  $44 \text{ cm}^{-3}$ . For electron densities much smaller than the critical density  $n_e \ll n_{\text{cr}}$ , Equation (2) can be written as

$$I_{[\text{C II}]}^- = n_e N_{\text{C}^+} \left[ 1.52 \times 10^{15} n_{\text{cr}} e^{\frac{91.21}{T_{\text{kin}}}} \right]^{-1}. \quad (6)$$

The term  $n_e N_{\text{C}^+}$  can be written in terms of the fractional abundance of ionized carbon,  $X_{\text{C}^+} = N_{\text{C}^+}/N_{\text{H}^+}$ , as  $X_{\text{C}^+} n_e N_{\text{H}^+} = X_{\text{C}^+} EM$ . Paradis et al. (2011) estimated typical electron densities for regions emitting different regimes of H $\alpha$  emission. For the range of H $\alpha$  intensities in our sample, electron densities vary from 0.05 to  $3.98 \text{ cm}^{-3}$ , thus validating the assumption that  $n_e \ll n_{\text{cr}}$ . Equation (6) can thus be rewritten in terms of the emission measure as,

$$I_{[\text{C II}]}^- = X_{\text{C}^+} EM \left[ 1.52 \times 10^{15} n_{\text{cr}} e^{\frac{91.21}{T_{\text{kin}}}} \right]^{-1}, \quad (7)$$

and can be used to estimate the contribution of ionized gas to the observed [C II] emission from H $\alpha$  observations.

In Figure 5, we show the fraction of the [C II] emission we estimate arises from ionized gas as a function of the observed [C II] emission in the LMC and SMC. We assumed  $T_{\text{kin}} = 8000 \text{ K}$  for the kinetic temperature of the ionized gas. In LOSs with multiple velocity components, we assumed that each component contributes equally to the derived [C II] emission from ionized gas, as suggested by the H66 $\alpha$  spectrum in Figure 6 that shows two [C II] velocity components with varying peak intensities but uniform recombination line emission. We find that ionized gas tends to contribute a small fraction of the [C II] emission, with typical fractions around 19% in the LMC and 5% in the SMC. These contributions from ionized gas to the observed [C II] emission are in agreement with those estimated using the unobscured [N II] fine structure lines by Chevance et al. (2016) and Okada et al. (2015) in the 30 Dor and N159 regions in the LMC, respectively, and by Requena-Torres et al. (2016) in several star forming regions in the SMC. The derived contributions from ionized gas to the observed [C II] emission in the LMC and SMC are also consistent with those estimated in the Galactic plane (Pineda et al. 2013).

We estimated the H<sup>+</sup> column density in our LOSs using  $EM = n_e N_{\text{H}^+}$  and the volume densities of the ionized gas suggested by Paradis et al. (2011) for different ranges of H $\alpha$  emission. Typical H<sup>+</sup> column densities in our sample are  $10^{20.8 \pm 0.35} \text{ cm}^{-2}$  for the LMC and  $10^{20.5 \pm 0.14} \text{ cm}^{-2}$  for the SMC.

Note that the H $\alpha$  emission used here might be affected by extinction from dust grains making our estimate of the emission measure from H $\alpha$  observations a lower limit. We tested the effect of dust extinction in the H $\alpha$  observations by assuming that half of the visual extinction ( $A_{\text{H}\alpha} = 0.81 A_V$ , e.g. Viallefond & Goss 1986; Parker et al. 1992) derived for each line-of-sight (Section 4.1) is in front of the H $\alpha$  sources. We find that the H $\alpha$  intensities would be underestimated by an average factor of 4.6 in the LMC and 1.4 in the SMC. In the LMC the large factor is dominated by three warm and dense PDRs, PDR4\_RIDGE, PDR3\_NW, and LMC\_1\_NW, which are

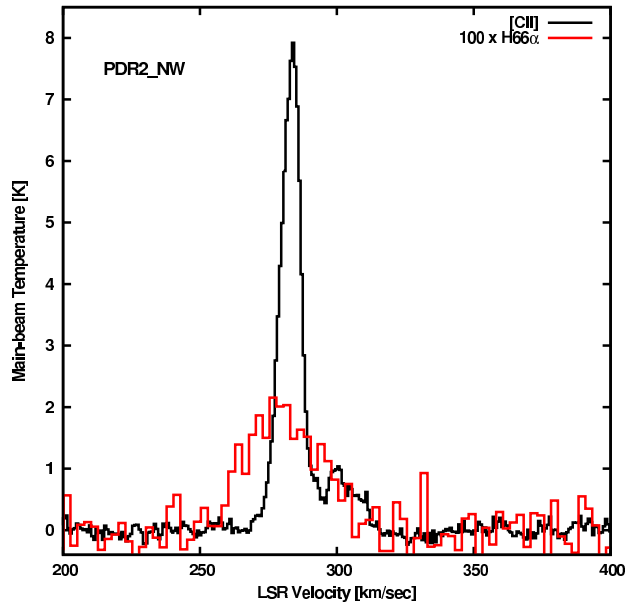


FIG. 6.— Comparison between [C II] and the H66 $\alpha$  radio recombination line in the PDR2\_NW position.

bright in [C II] and have the largest visual extinctions. Without these PDR regions, we find that the H $\alpha$  emission would be affected by a factor of 1.65 in the LMC. If a correction to the H $\alpha$  intensity for dust extinction is applied to the calculation of the contribution of ionized gas to the observed [C II] emission, the fraction would increase by a similar factor. Note that for the warm and dense PDRs mentioned above, applying a correction to the contribution from ionized gas to the observed [C II] emission would result in larger [C II] intensities than observed, suggesting that less than  $A_V/2$  of extinction is in the foreground of these sources.

We tested the reliability of H $\alpha$  as a tracer of ionized gas by observing the unobscured H66 $\alpha$  radio recombination line using the DSS-43 NASA Deep Space Network Telescope in one of our lines-of-sight (Figure 6). Following Alves et al. (2015), we converted the integrated intensity of the H66 $\alpha$  line to the emission measure, assuming  $T_{\text{kin}} = 8000$  K, to be  $1.9 \times 10^4 \text{ cm}^{-6} \text{ pc}$ . For the same position we obtain  $EM = 7.8 \times 10^3 \text{ cm}^{-6} \text{ pc}$  from H $\alpha$ , a factor of  $\sim 2.4$  lower than that obtained from H66 $\alpha$ . The position we observed in H66 $\alpha$  corresponds to a warm and dense photon dominated region likely associated with a large column of dust, so we expect a smaller effect in more diffuse regions in our sample.

### 3.2. Atomic Gas

We estimated the contribution from atomic gas to the observed [C II] emission in our sample in the Magellanic Clouds using the H I 21 cm line observations. We calculated  $N(\text{H}^0)$  for each LOS, assuming optically thin emission, using  $N(\text{H}^0) = 1.82 \times 10^{18} I(\text{H I}) \text{ cm}^{-2}$ , with  $I(\text{H I})$  in units of  $\text{K km s}^{-1}$ . We converted from  $N(\text{H}^0)$  to  $N(\text{C}^+)$  using the carbon fractional abundances of the LMC and SMC, assuming that all gas-phase carbon associated with atomic gas is in the form of  $\text{C}^+$ .

We only considered H I emission that is associated in velocity space with [C II] emission, and to calculate  $I(\text{H I})$  we integrate the H I spectrum over a velocity range de-

finied by the full width at half maximum (FWHM) of the [C II] lines. Because the [C II] emission is volume density sensitive for  $n_{\text{H}} < 3000 \text{ cm}^{-3}$ , the critical density for collisions with H (Goldsmith et al. 2012), we expect that the [C II] emission is associated with cold, dense H I (CNM; Wolfire et al. 2003) rather than diffuse, warm H I (WNM; see discussion in Pineda et al. 2013.) We therefore consider the H I emission that is associated in velocity with [C II] to be CNM while the remaining H I emission is WNM. In the top panel of Figure 2, we illustrate this decomposition by showing the velocity range as a shaded region in which we assign H I to be CNM. Note that due to the typical complexity of the H I line profiles, it is difficult to separate reliably components in velocity for our entire data set.

Our method for calculating the H I column could be overestimating the column density of cold atomic hydrogen associated with [C II] if a broad WNM component overlaps in velocity with the [C II] emission. To quantify this effect, we attempted to fit multiple Gaussian components to the H I spectra of SMC\_HI\_4 and SMC\_LIRS36 shown in Figure 2. For the Gaussian fitting, we fixed the LSR velocity of the [C II] components (see Table 4) and left the peak main-beam temperature and line width as free parameters. We then subtracted all Gaussian components that are not associated with [C II] to the observed spectra, in order to isolate the Gaussian component associated with [C II]. In this component, we recalculated the integrated intensity by integrating over the velocity range defined by the FWHM of the [C II] line, as above. We find that we would typically overestimate the H I intensity associated with CNM by a factor of about 2 in SMC\_HI\_4 and SMC\_LIRS36. Note, however, that complex H I spectra such as those of SMC\_HI\_4 and SMC\_LIRS36 are typically rare in our sample, and mostly correspond to SMC lines-of-sight. In the SMC there are 5 LOSs with such complexity out of 10 detected in [C II]. In the LMC the H I spectra is mostly similar to those of Diff1\_NW and PDR1\_NW as shown in Figure 2.

To calculate the [C II] intensity from atomic gas using Equation (2), we need to assume a gas volume density and a kinetic temperature. As discussed in Section 3.4, we adopted a kinetic temperature of  $T_{\text{kin}} = 70$  K in the case of velocity components where H I and [C II] are detected but  $^{13}\text{CO } J = 1 \rightarrow 0$  and/or  $J = 3 \rightarrow 2$  are not. In these LOSs, we were unable to determine the physical conditions of the  $\text{C}^0$  or CO layer. In LOSs with kinetic temperatures of the  $\text{C}^0$  and/or CO layers derived in the excitation analysis (Section 4.4.3), and with [C II] and H I detected, we still assume 70 K if the kinetic temperature of the  $\text{C}^0$  layer is lower than 70 K. Otherwise, we assume the kinetic temperature of the  $\text{C}^0$  layer. The volume density is then derived by combining the kinetic temperatures with the thermal pressures of the diffuse ISM derived in Section 4.3.

In Figure 5, we show the fraction of the observed [C II] emission from atomic gas as a function of the observed [C II]. The contribution from atomic gas to the observed [C II] emission shows a large scatter with average values of about 43% for the LMC and 28% for the SMC. These average contributions are consistent with the 20% contribution derived in the plane of the Milky Way by Pineda et al. (2013).

### 3.3. CO-dark H<sub>2</sub> gas and dense Photon Dominated Regions (PDRs)

When we subtract the contribution from the ionized and atomic gas components to the observed total [C II] emission, we typically find that there is residual [C II] emission. This residual emission is produced in regions where carbon is ionized but hydrogen is molecular. The molecular hydrogen component where carbon is mainly ionized, so that it is traced by [C II] and not by CO, is what we refer to as CO-dark H<sub>2</sub> gas. The CO-dark H<sub>2</sub> gas can either originate (1) from a diffuse cloud that has enough dust shielding to maintain only a trace amount of C<sup>0</sup> and CO, thus with most of the carbon in the form of C<sup>+</sup>, or (2) from the envelopes of a warm and dense molecular cloud in which the inner parts have significant column densities of C<sup>0</sup> and CO. In order to associate the observed [C II] velocity components to either of these gas conditions, we use the detection limit of the <sup>13</sup>CO lines observed in our survey to identify clouds that have enough shielding to maintain significant amounts of CO, and therefore are likely associated warm and dense molecular clouds with ongoing star formation. We assigned the [C II] emission to warm and dense PDRs in velocity components with enough CO column density for the <sup>13</sup>CO  $J = 1 \rightarrow 0$  and/or <sup>13</sup>CO  $J = 3 \rightarrow 2$  lines to be detected. In LOSs where the <sup>13</sup>CO lines are detected, we were able to perform an excitation analysis (Section 4.4) that confirms our assumption of warm and dense gas in these velocity components (see Table 5). In LOSs that are detected in [C II] and H I, but not in <sup>13</sup>CO  $J = 1 \rightarrow 0$  and/or <sup>13</sup>CO  $J = 3 \rightarrow 2$ , we assumed that the residual [C II] emission arises from diffuse CO-dark H<sub>2</sub> gas clouds. In LOSs associated with PDRs, the [C II] emission from this ISM component tends to be brighter than the emission arising from other components, which is the result of the higher volume densities and temperatures of the gas. The typical contributions to the [C II] emission associated with PDRs are 62% and 66% of the observed emission in LOS in the LMC and SMC, respectively. The fraction of the [C II] emission arising from CO-dark H<sub>2</sub> shows a large scatter, ranging from ~10% to ~80%. A similar range of CO-dark H<sub>2</sub> fractions is found in clouds in the Milky Way (Langer et al. 2014; Tang et al. 2016). This large scatter could be the result of clouds at different stages in the transition from diffuse to dense molecular gas, with clouds having varying fractions of CO-dark H<sub>2</sub> gas.

Our separation between [C II] from diffuse CO-dark H<sub>2</sub> gas and from warm and dense PDRs is sensitive to our ability to detect the <sup>13</sup>CO  $J = 1 \rightarrow 0$  and/or <sup>13</sup>CO  $J = 3 \rightarrow 2$  lines. For the thermal pressure of the diffuse ISM in the LMC and SMC derived in Section 4.3 and a kinetic temperature of the CO-dark H<sub>2</sub> of 49K (Section 5.1), we obtain  $n(\text{H}_2)=694 \text{ cm}^{-3}$  in the LMC and  $2040 \text{ cm}^{-3}$  in the SMC. For these conditions, the <sup>13</sup>CO column density required for a  $3\sigma$  detection of the <sup>13</sup>CO  $J = 1 \rightarrow 0$  and <sup>13</sup>CO  $J = 3 \rightarrow 2$  is  $4 \times 10^{14} \text{ cm}^{-2}$  and  $3 \times 10^{15} \text{ cm}^{-2}$  for the LMC and  $4.5 \times 10^{14} \text{ cm}^{-2}$  and  $1 \times 10^{15} \text{ cm}^{-2}$  of SMC, respectively.

### 3.4. Uncertainties

The main uncertainty in our decomposition originates from the assumption of the temperature of atomic and

molecular gas. The assumed kinetic temperature is used in the derivation of thermal pressures (Section 4.3) and in the calculation of the contribution of atomic gas to the observed [C II] emission. Observations of H I absorption against background continuum sources in the LMC and SMC suggest temperatures of the atomic gas as low as 10 K, with typical values of 30–40 K (Marx-Zimmer et al. 2000; Dickey et al. 2000). Note that H I absorption features are stronger the lower the kinetic temperature of the H I gas, thus there might be a systematic tendency to detect colder atomic gas in absorption. At these low temperatures, most of the gas-phase carbon is likely to be in the form of CO rather than in C<sup>+</sup>, as suggested by the detection of the <sup>12</sup>CO  $J = 1 \rightarrow 0$  line in several H I absorption sources in the LMC (Marx-Zimmer et al. 1999). While it is possible that the H I temperatures are lower in the Magellanic clouds compared with our Galaxy, we consider it unlikely that [C II] will be detected for temperatures below 40 K, as the [C II] intensity is significantly reduced for kinetic temperatures below this value. We therefore assume a temperature of 70 K for the atomic gas in our calculations, which is an intermediate value between the temperature derived from H I absorption in the Magellanic Clouds and the 100 K typically assumed in the Milky Way (Pineda et al. 2013). For the temperature of the H<sub>2</sub> gas, we assume that  $T_{\text{kin}}^{\text{H}_2} = 0.7T_{\text{kin}}^{\text{H}^0}$ , which is based on results in the Milky Way that suggest a temperature of 70 K for the CO-dark H<sub>2</sub> layer (Goldsmith 2013), and which is in agreement with PDR models calculations (e.g. Goldsmith et al. 2016). The temperature of the CO-dark H<sub>2</sub> gas corresponds to 49 K for our assumed H I temperature of 70 K.

We estimated the uncertainty associated with our H I and H<sub>2</sub> kinetic temperature assumption by calculating the range in the [C II] intensities associated with the different ISM phases resulting from assuming  $T_{\text{kin}}^{\text{H}^0} = 40$  K and  $T_{\text{kin}}^{\text{H}^0} = 100$  K in the LMC and  $T_{\text{kin}}^{\text{H}^0} = 55$  K and  $T_{\text{kin}}^{\text{H}^0} = 100$  K in the SMC. We used  $T_{\text{kin}}^{\text{H}^0} = 55$  K as a lower kinetic temperature limit in the SMC, as this is the lowest temperature where we could find solutions of the thermal pressure in the SMC (see Section 4.3). The derived uncertainties are shown as error bars in Figure 5.

Note that the assumed temperature of the CO-dark H<sub>2</sub> gas is lower than the H<sub>2</sub> rotational temperature in lines-of-sight compiled by Welty et al. (2012) in the LMC and SMC. These H<sub>2</sub> temperatures range from 40 to 120 K, with average values of 85 K in both the LMC and SMC. This range corresponds, for our assumption of  $T_{\text{kin}}^{\text{H}_2} = 0.7T_{\text{kin}}^{\text{H}^0}$ , to a range in H<sup>0</sup> kinetic temperature between 57 and 170 K. However, the LOSs studied by Welty et al. (2012) have total hydrogen column densities that are much lower compared to the values derived in our survey (see Figure 13), and therefore are diffuse and likely warmer LOSs.

Another source of uncertainty originates from beam filling effects produced by the different angular resolution of our observations. The angular resolution of the data used in our [C II] decomposition varies from 12'' for [C II] to 60'' for H I. As described in Appendix A, we derived correction factors using the 160 μm map for [C II] and H I, and the 24 μm continuum maps for the SHASSA observations. We estimate that the contribution from



the different ISM phases to the observed [C II] emission would change typically by 10%, 14%, 17%, and 16% for PDRs, CO-dark H<sub>2</sub> gas, H I gas, and ionized gas in the LMC, respectively, and by 6%, 4%, 15%, and 8% for PDRs, CO-dark H<sub>2</sub> gas, H I gas, and ionized gas in the SMC, respectively. In Figure 21, we present the fraction of [C II] originating from different ISM phases as a function of the observed [C II] intensity in the case when the intensities are corrected by beam dilution effects. We choose not to include the variation in the intensities due to beam filling factors in Figure 5 due to the uncertainty in whether the 24 μm and 160 μm emission represents the spatial distribution of the [C II] associated with ionized and neutral gas, respectively.

#### 4. PHYSICAL PARAMETERS

##### 4.1. Determination of Visual Extinction

We used the *Herschel* HERITAGE (Meixner et al. 2013) dust continuum maps of the LMC and SMC to determine the dust column density, in terms of the visual extinction  $A_V$ , in our sample. We assume that the dust spectral energy distribution (SED) in the LMC and SMC can be described by the emission predicted from an optically thin modified black body at an equilibrium temperature  $T_{\text{dust}}$ . The dust opacity at 160 μm is given by

$$\tau_{160\mu\text{m}} = \frac{I_{160\mu\text{m}}}{B_\nu(T_{\text{dust}}, 160\mu\text{m})}, \quad (8)$$

where  $I_{160\mu\text{m}}$  is the dust continuum intensity at 160 μm and  $B_\nu(T_{\text{dust}}, 160\mu\text{m})$  is the intensity of a black body with a temperature  $T_{\text{dust}}$  at 160 μm. We determined the opacity at 160 μm using the HERITAGE 160 μm map together with the dust temperatures fitted by Gordon et al. (2014) for a single temperature blackbody modified by a broken power-law emissivity, their preferred dust emission model. Both the 160 μm and dust temperature maps have a common resolution of 40". The average ( $\pm$  standard deviation) dust temperature is  $22.8 \pm 4.1$  K in the LMC and  $23.1 \pm 2.5$  K in the SMC.

Lee et al. (2015) presented maps of the visual extinction in the LMC and SMC derived from dust continuum emission. They converted the 160 μm opacity to  $A_V$  using,  $A_V = 2200\tau_{160\mu\text{m}}$ , which is the average of different methods to relate these quantities based on data in the Milky Way. (We refer the reader to their paper for more details on how this conversion factor is determined.) The different methods described in Lee et al. (2015) show a scatter from the adopted conversion factor between  $A_V$  and  $\tau_{160\mu\text{m}}$  of about 40%, and we adopt this value as the uncertainty in our determination of  $A_V$ .

We compared the values of  $A_V$  derived here with those presented by Lee et al. (2015) who derived the 160 μm opacity using the HERITAGE 160 μm map and dust temperatures determined by fitting a single temperature blackbody with an assumed  $\beta = 1.5$  wavelength dependence of the dust opacity. We find that our  $A_V$  values are in reasonable agreement with those derived by Lee et al. (2015), with differences typically within the assumed 40% uncertainty.

##### 4.2. Dust-to-Gas ratio

The dust-to-gas ratio (DGR) is a fundamental parameter relating the quantities of gas and dust in the ISM

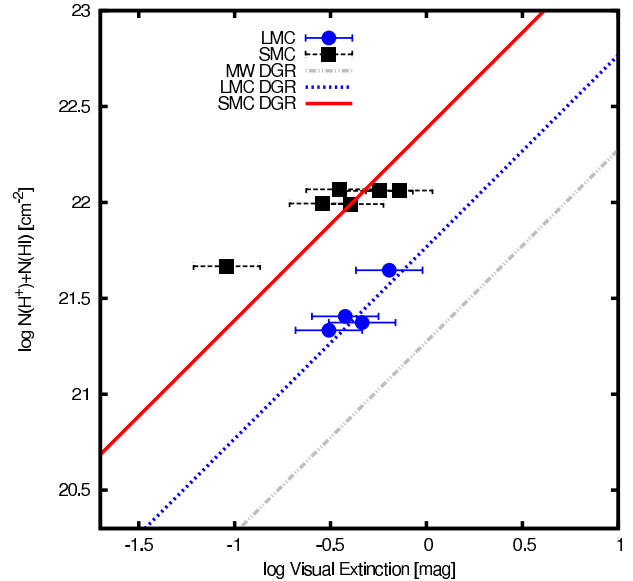


FIG. 7.— The H<sup>+</sup>+H<sup>0</sup> column density as a function the visual extinction associated with atomic gas for LOSs in the LMC and SMC where H I and H $\alpha$  are the only spectral lines detected, therefore assumed to be diffuse gas. The straight lines represent the total hydrogen column density predicted for a given  $A_V$  assuming  $N(\text{H})/A_V=7.17 \times 10^{21} \text{ cm}^{-2} \text{ mag}^{-1}$  for the LMC,  $1.68 \times 10^{22} \text{ cm}^{-2} \text{ mag}^{-1}$  for the SMC, and  $1.88 \times 10^{21} \text{ cm}^{-2} \text{ mag}^{-1}$  for the Milky Way (Section 4.2).

of galaxies and the variation of the DGR as a function of environment reflects the evolution of galaxies (Dwek 1998). In the following, we test our determination of gas column densities and visual extinctions in our sample by checking whether these two quantities are related by the DGRs that are typically found in the LMC and SMC. We initially test diffuse LOSs in our sample, but we will extend this comparison to our entire sample in Section 5.1 to test our determination of H<sub>2</sub> column densities.

The ratio of the total hydrogen column density,  $N(\text{H}) = N(\text{H}^+) + N(\text{H}^0) + 2N(\text{H}_2)$ , to color excess,  $E(B-V)$ , in the ISM of the Milky Way is  $N(\text{H})/E(B-V)=5.8 \times 10^{51} \text{ cm}^{-2} \text{ mag}^{-1}$  (Bohlin et al. 1978). Assuming a ratio of the total to selective extinction of  $R_V=3.1$ , results in a relationship between the hydrogen column density and visual extinction of  $N(\text{H})/A_V=1.88 \times 10^{21} \text{ cm}^{-2} \text{ mag}^{-1}$  in the Milky Way. In the LMC,  $N(\text{H})/E(B-V)$  is observed to be  $2 \times 10^{22} \text{ cm}^{-2} \text{ mag}^{-1}$  (Koornneef 1982; Fitzpatrick 1985a), while in the SMC,  $N(\text{H})/E(B-V)$  ranges between  $2.6 \times 10^{22} \text{ cm}^{-2} \text{ mag}^{-1}$  (Martin et al. 1989) and  $8.7 \times 10^{22} \text{ cm}^{-2} \text{ mag}^{-1}$  (Fitzpatrick 1985b). We adopt an intermediate value for the SMC of  $6.6 \times 10^{22} \text{ cm}^{-2} \text{ mag}^{-1}$ . Assuming  $R_V=3.4$  in the LMC and  $R_V=2.7$  in the SMC (Gordon et al. 2003), results in  $N(\text{H})/A_V=5.56 \times 10^{21} \text{ cm}^{-2} \text{ mag}^{-1}$  for the LMC and  $2.43 \times 10^{22} \text{ cm}^{-2} \text{ mag}^{-1}$  for the SMC. Note that the value of  $R_V$  assumed here corresponds to that in diffuse regions, and it might be larger in denser regions (Weingartner & Draine 2001; Whittet et al. 2001). Considering that a given line of sight might intersect both dense and diffuse regions, Whittet et al. (2001) estimated in the Milky Way an effective  $R_V$  along the line-of-sight that increases up to  $\sim 4.0$  for  $A_V \simeq 10$  mag. Thus, the  $N(\text{H})/A_V$  ratio can be lower by up to  $\sim 30\%$  in denser

LOSs.

We tested our estimate of the visual extinction by comparing  $A_V$  with  $N(\text{H}^+) + N(\text{H}^0)$  in LOSs where  $[\text{C II}]$  was not detected. These lines-of-sight (5 in the LMC and 7 in the SMC) likely have little or no  $\text{H}_2$  and/or have densities and temperatures that are insufficient for producing  $[\text{C II}]$  emission that will be detectable in the sensitivity limits of our survey. They are therefore well suited for our comparison between visual extinctions and the  $\text{H}^+ + \text{H}^0$  column densities as they are likely to have a negligible or no contribution from dust associated with  $\text{H}_2$  to the observed  $A_V$ . The  $\text{H}^+$  column densities for these LOSs were determined in Section 3.1 and on average represent 5% and 1.4% of the  $N(\text{H}^+) + N(\text{H}^0)$  column densities in the LMC and SMC, respectively. The  $A_V$  and  $N(\text{H}^+)$  data points used here were derived from dust continuum and  $\text{H}\alpha$  maps that were smoothed to the  $60''$  resolution of the  $\text{H I}$  data. In Figure 7, we show  $N(\text{H}^+) + N(\text{H}^0)$  as a function of  $A_V$  for LOSs in our sample where the  $[\text{C II}]$  was not detected. We also include in the plot straight lines that represent the predicted  $\text{H}^+ + \text{H}^0$  column density for a given value of  $A_V$  using the dust-to-gas ratios for the LMC, SMC, and Milky Way discussed above. Given the uncertainties in the determination of  $A_V$ , we consider that our derived values of  $A_V$  are consistent with the observed  $\text{H I}$  column densities and the independently measured gas-to-dust ratios in the LMC and SMC.

#### 4.3. Thermal Pressures of the diffuse ISM in the Magellanic Clouds

The thermal pressure of the diffuse ISM is an important parameter which, despite being a small fraction of the total ISM pressure (Boulares & Cox 1990), plays a fundamental role in the phase transition from warm and diffuse to cold and dense atomic gas (Pikel’Ner 1968; Field et al. 1969; Wolfire et al. 1995, 2003; Jenkins & Tripp 2011). Thus, studying the diffuse ISM thermal pressure is important for our understanding of molecular cloud formation and the regulation of star formation in galaxies (McKee 1989; Blitz & Rosolowsky 2006; Ostriker et al. 2010).

In the Magellanic clouds the thermal pressure of the gas is expected to be larger than the solar neighborhood because of larger FUV fields and lower dust abundances, affecting the thermal balance (Wolfire et al. 2017 in preparation; Sandstrom et al. 2010; Welty et al. 2016). Bolatto et al. (2011) compared the relationship between gas surface density and star formation rate in the SMC and found that a thermal pressure  $p_{\text{th}}/k_B = 3 \times 10^4 \text{ K cm}^{-3}$  is required to find agreement between observations and the theoretical predictions from Ostriker et al. (2010).

An estimate of the thermal pressure of the diffuse ISM is also a requirement for the determination of the column density of the CO-dark  $\text{H}_2$  gas using  $[\text{C II}]$  observations (Pineda et al. 2013). In the following we derive the thermal pressures of the diffuse ISM of the LMC and SMC by using LOSs where we detect  $\text{H I}$  and  $[\text{C II}]$  but where no CO and/or  $[\text{C I}]$  is detected. These LOSs (14 in the LMC and 6 in the SMC) are likely diffuse and the  $[\text{C II}]$  emission arises from both cold atomic and CO-dark  $\text{H}_2$  gas.

As discussed in Section 3, the observed  $[\text{C II}]$  intensity is the sum of the emission associated with the ionized,

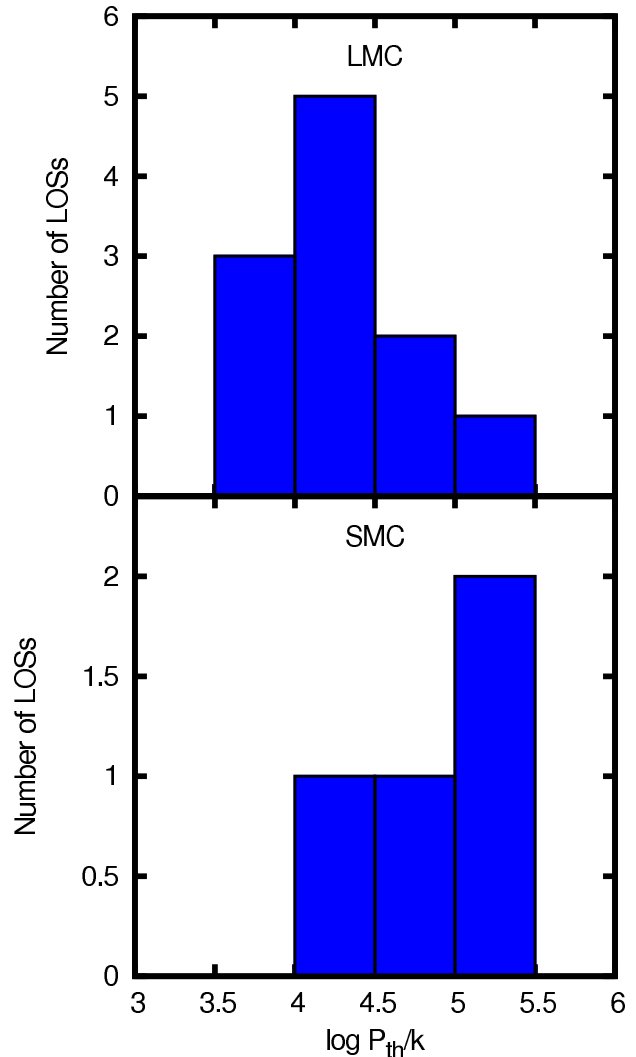


FIG. 8.— Histograms of the thermal pressure of the diffuse interstellar medium of the LMC and SMC derived in Section 4.3.

atomic, and molecular gas components. For each LOS used here, we subtracted the  $[\text{C II}]$  emission associated with ionized gas derived in Section 3.1. The remaining  $[\text{C II}]$  intensity is thus described by six parameters (see Equation 2): the kinetic temperature ( $T_{\text{kin}}^{\text{H}^0}$  and  $T_{\text{kin}}^{\text{H}_2}$ ), volume density ( $n_{\text{H}^0}$  and  $n_{\text{H}_2}$ ), and  $\text{C}^+$  column densities ( $N(\text{C}^+)_{\text{H}^0}$  and  $N(\text{C}^+)_{\text{H}_2}$ ) of gas associated with the  $\text{H}^0$  and  $\text{H}_2$  layers.

The total column density of  $\text{C}^+$  along the line of sight is the sum of the column of  $\text{C}^+$  associated with the different collisional partners,

$$N(\text{C}^+)_{\text{total}} = N(\text{C}^+)_{\text{H}^0} + N(\text{C}^+)_{\text{H}_2} + N(\text{C}^+)_{e^-}. \quad (9)$$

We used the  $\text{H I}$  21 cm observations to determine the column density of atomic hydrogen that is associated in velocity with the observed  $[\text{C II}]$  emission in Section 3.2 and the  $\text{H}^+$  column density associated with ionized gas in Section 3.1. The  $\text{H}^0$  and  $\text{H}^+$  column densities are in turn converted to a  $\text{C}^+$  column density by multiplying the carbon fractional abundances of the LMC and SMC discussed in Section 3.

To derive the column density of  $\text{C}^+$  associated with  $\text{H}_2$ ,



we need an estimate of the total hydrogen column density along the line of sight. The visual extinction along the line-of-sight is the sum of that from dust associated with molecular hydrogen, with CNM and WNM atomic gas, and with ionized gas, so that

$$A_V^{\text{total}} = A_V^{\text{H}_2} + A_V^{\text{H}^0, \text{CNM}} + A_V^{\text{H}^0, \text{WNM}} + A_V^{\text{H}^+}. \quad (10)$$

We estimated  $A_V^{\text{HI, CNM}}$  and  $A_V^{\text{HI, WNM}}$  by converting the integrated intensities of HI associated (CNM) and not associated (WNM) to the observed [C II] emission and applying the dust-to-gas ratios discussed in Section 4.2. The same dust-to-gas ratio was applied to the  $\text{H}^+$  column densities to estimate visual extinction associated with ionized gas. The visual extinction associated with  $\text{H}_2$  is then estimated by subtracting that associated with  $\text{H}^0$  and  $\text{H}^+$  to the observed value. We then converted  $A_V^{\text{H}_2}$  to a  $\text{H}_2$  column density using a dust-to-gas ratio, and to  $N(\text{C}^+)_{\text{H}_2}$  using a fractional abundance of carbon.

With an estimate of  $N(\text{C}^+)_{\text{H}^0}$  and  $N(\text{C}^+)_{\text{H}_2}$ , the remaining parameters are the kinetic temperatures and volume densities of the molecular and cold atomic gas. We assumed that for the diffuse lines-of-sight where only HI and [C II] are detected there is thermal pressure equilibrium in the interface between the cold HI and the CO-dark  $\text{H}_2$  layers,

$$p_{\text{th}}/k_B = n_{\text{H}} T_{\text{kin}}^{\text{H}^0} = n_{\text{H}_2} T_{\text{kin}}^{\text{H}_2}. \quad (11)$$

Assuming a kinetic temperature for the HI layer of 70 K and for the CO-dark  $\text{H}_2$  layer of 49 K (see discussion in Section 3.4), we searched for a thermal pressure that can reproduce the observed [C II] intensity. Figure 8 shows histograms of the thermal pressures derived in the LMC and SMC. The average ( $\pm$  standard deviation) thermal pressure is  $p_{\text{th}}/k_B = 10^{4.5 \pm 0.3} \text{ K cm}^{-3}$  in the LMC and  $p_{\text{th}}/k_B = 10^{5.0 \pm 0.2} \text{ K cm}^{-3}$  in the SMC. We note that components that are associated with the 30 Doradus nebula in the LMC tend to higher thermal pressures compared to those in other regions of the LMC. Without the LOSs associated with 30 Doradus, we find an average thermal pressure in the LMC of  $p_{\text{th}}/k_B = 10^{4.2 \pm 0.1} \text{ K cm}^{-3}$  while LOSs associated with 30 Doradus have  $p_{\text{th}}/k_B = 10^{4.9 \pm 0.2} \text{ K cm}^{-3}$ . These LOSs appear to be influenced by the feedback effects of the R136 super star cluster (Pellegrini et al. 2011). The average value for the SMC is in reasonable agreement with that suggested by Bolatto et al. (2011).

We tested the sensitivity of the derived thermal pressures to the assumed kinetic temperature of the gas. For low temperatures, the thermal pressure solutions become uncertain, as higher volume densities are needed to reproduce the observed emission, and collisional deexcitation become important, reducing the dependence of the [C II] intensity on volume density (Goldsmith et al. 2012). In the LMC the thermal pressure increases by a factor of 1.2 between 100 K and 70 K and by a factor of 6 between 100 K and 40 K. In the SMC, we could not find reliable solutions for temperatures lower than 55 K. Between 100 K and 70 K, the thermal pressure increases by a factor of 1.5 and between 100 K and 55 K, by a factor of 3.5.

We also studied the effects of beam dilution in our determination of thermal pressures in the LMC and SMC. For that purpose, we smoothed the dust continuum data

used to calculate  $A_V$ , and the  $\text{H}\alpha$  data used to estimate the contribution from ionized gas to the [C II] emission, to the 60'' resolution of the HI data used to calculate  $N(\text{H}^0)$ . We additionally corrected the observed [C II] emission with the beam dilution factor we estimated in Appendix A to correspond to emission at 60'' resolution. We used this data to recalculate the thermal pressures in our sub-sample. We find that applying a beam dilution factor to the data used in our calculation results in thermal pressures that are reduced by factors of  $\sim 1.4$  in both the LMC and SMC.

We note that the statistical significance of our determination of the thermal pressure in the LMC and SMC is limited by the small number of LOSs we were able to use. Using the technique presented here in future large scale maps of the Magellanic Clouds in [C II] will dramatically improve the significance of this result, and will allow us to compare the distribution of thermal pressures in the LMC and SMC with that in the Milky Way (Jenkins & Tripp 2011).

#### 4.4. Kinetic temperatures and $\text{H}_2$ Column and Volume Densities

We constrained the properties of the CO and [C I]-emitting gas by comparing line intensity ratios and absolute intensities of [C I],  $^{12}\text{CO}$ , and  $^{13}\text{CO}$  with the results of a radiative transfer code. We used the RADEX non-LTE radiative transfer code (van der Tak et al. 2007), using the uniform sphere approximation, to calculate line intensities as a function of the kinetic temperature,  $\text{H}_2$  volume density, and the column density per velocity interval  $N/\Delta v$  of the species of interest. The collisional rate coefficients were taken from the Leiden Atomic and Molecular Database (LAMDA; Schöier et al. 2005).

In the PDRs located at the borders of molecular clouds, the innermost region is at higher density, deeper in the cloud, and the outermost region is at lower density. Thus, the physical conditions of the  $\text{C}^0$  layer are not necessarily the same as those at the CO layer. Since we will be modelling spheres with uniform volume density and kinetic temperature, we analyzed the [C I] and CO data separately. We nevertheless assume that the [C I] and CO emission originate from the same regions with identical filling factors. This assumption is justified considering that the CO and [C I] emission arise from the FUV illuminated surfaces of clouds that are unresolved at the scale of our observations. For optically thin clumps (or for clumps with moderate opacity), the observed-to-model integrated intensity ratio gives the ratio of the beam-averaged column density to the clump intrinsic column density, assuming that the total integrated intensity is proportional to the number of clumps, i.e. no velocity crowding is present. We therefore determined the beam filling factor by comparing the observed absolute intensity of an optically thin line ( $^{13}\text{CO } J = 3 \rightarrow 2$  or  $^{13}\text{CO } J = 1 \rightarrow 0$ ) with a constrained model.

We compared the observed line intensity ratios with the predictions from a grid of RADEX models. The model grids predict line ratios for the kinetic temperatures ranging from 10 K to 200 K in steps of 10 K as a function of the CO or  $\text{C}^0$  column densities per velocity interval,  $N_{\text{CO}}/\Delta v$  (or  $N_{\text{C}^0}/\Delta v$ ), and  $\text{H}_2$  volume density,  $n_{\text{H}_2}$ . The coverage in  $N_{\text{CO}}/\Delta v$  and  $N_{\text{C}^0}/\Delta v$  is  $10^{15} - 10^{19} \text{ cm}^{-2} (\text{km s}^{-1})^{-1}$  and in  $n_{\text{H}_2}$  is  $10^2 - 10^6$

TABLE 5  
DERIVED PARAMETERS FOR LMC AND SMC SAMPLE

LOS	$N(\text{H}^0)_{\text{CNM}}^1$ log [cm <sup>-2</sup> ]	$T_{\text{kin}}^{\text{C}^+;2}$ [K]	$n_{\text{H}_2}^{\text{C}^+;3}$ log [cm <sup>-3</sup> ]	$N(\text{C}^+)_{\text{H}_2}^4$ log [cm <sup>-2</sup> ]	$T_{\text{kin}}^{\text{C}^0;2}$ [K]	$n_{\text{H}_2}^{\text{C}^0;3}$ log [cm <sup>-3</sup> ]	$N(\text{C}^0)^4$ log [cm <sup>-2</sup> ]	$T_{\text{kin}}^{\text{CO};2}$ [K]	$n_{\text{H}_2}^{\text{CO};3}$ log [cm <sup>-3</sup> ]	$N(\text{CO})^4$ log [cm <sup>-2</sup> ]	filling <sup>5</sup> factor
Large Magellanic Cloud											
Diff2_SE_1	20.5 <sup>6</sup>	49	2.8	17.1 <sup>+0.2</sup> <sub>-0.1</sub>	–	–	–	–	–	–	–
Diff7_NW_1	20.7 <sup>6</sup>	49	2.8	17.1±0.1	–	–	–	–	–	–	–
LMC11_Ridge_1	20.8 <sup>6</sup>	40±10	3.4 <sup>+0.06</sup> <sub>-0.3</sub>	17.5±0.3	40±10	3.9 <sup>+0.2</sup> <sub>-0.6</sub>	15.9 <sup>+0.3</sup> <sub>-0.7</sub>	20±10	4.5±0.1	15.9 <sup>+0.3</sup> <sub>-0.7</sub>	0.10 <sup>+0.04</sup> <sub>-0.32</sub>
LMC12_SE_1	20.6 <sup>6</sup>	30±10	3.7±0.0 <sup>6</sup>	17.5 <sup>+0.3</sup> <sub>-0.6</sub>	30±10	4.4±0.1	15.3 <sup>+0.2</sup> <sub>-0.3</sub>	40±10	4.4±0.1	16.0 <sup>+0.2</sup> <sub>-0.3</sub>	0.10 <sup>+0.02</sup> <sub>-0.05</sub>
LMC12_SE_2	20.7 <sup>6</sup>	60±10	3.1±0.0 <sup>6</sup>	17.1 <sup>+0.1</sup> <sub>-0.2</sub>	60±10	3.5±0.1	16.2 <sup>+0.2</sup> <sub>-0.4</sub>	30±10	4.6 <sup>+0.3</sup> <sub>-0.1</sub>	16.3 <sup>+0.2</sup> <sub>-0.4</sub>	0.34 <sup>+0.09</sup> <sub>-0.32</sub>
LMC_1_NW_1	20.7 <sup>6</sup>	120±20	2.6±0.0 <sup>6</sup>	17.2±0.1	120±20	2.7±0.1	16.3 <sup>+0.2</sup> <sub>-0.4</sub>	50 <sup>+10</sup> <sub>-20</sub>	6.0 <sup>+1.9</sup> <sub>-0.1</sub>	16.2 <sup>+0.4</sup> <sub>-0.5</sub>	0.01 <sup>+0.007</sup> <sub>-0.02</sub>
LMC_1_NW_2	20.8 <sup>6</sup>	160±10	2.6±0.0 <sup>6</sup>	16.9±0.1	160±10	2.9±0.1	16.1 <sup>+0.2</sup> <sub>-0.3</sub>	60±10	4.0±0.1	15.8 <sup>+0.2</sup> <sub>-0.3</sub>	0.02 <sup>+0.007</sup> <sub>-0.01</sub>
LMC_1_NW_3	21.2 <sup>6</sup>	49	2.8	17.6±0.0 <sup>6</sup>	–	–	–	–	–	–	–
LMC2_NW_1	21.1 <sup>6</sup>	49	2.8	17.2±0.1	–	–	–	–	–	–	–
LMC3_NW_1	20.7 <sup>6</sup>	49	2.8	16.7 <sup>+0.3</sup> <sub>-0.2</sub>	–	–	–	–	–	–	–
LMC4_RIDGE_1	21.1 <sup>6</sup>	49	2.8	17.4±0.1	–	–	–	–	–	–	–
LMC5_SE_1	20.1 <sup>6</sup>	170 <sup>+10</sup> <sub>-20</sub>	2.8	17.3±0.0 <sup>6</sup>	170 <sup>+10</sup> <sub>-20</sub>	3.3±0.1	16.0 <sup>+0.2</sup> <sub>-0.4</sub>	30±10	4.6 <sup>+0.2</sup> <sub>-0.1</sub>	15.9 <sup>+0.2</sup> <sub>-0.4</sub>	0.09 <sup>+0.02</sup> <sub>-0.07</sub>
LMC7_RIDGE_1	21.1 <sup>6</sup>	49	2.8	17.4±0.1	–	–	–	–	–	–	–
LMC9_NE_1	20.8 <sup>6</sup>	49	2.8	16.7 <sup>+0.3</sup> <sub>-0.2</sub>	–	–	–	–	–	–	–
NT127_1	20.1 <sup>6</sup>	30±10	2.6±0.0 <sup>6</sup>	17.2 <sup>+0.5</sup> <sub>-0.7</sub>	30±10	2.1±0.1	16.7 <sup>+0.3</sup> <sub>-0.4</sub>	30±10	4.3±0.1	16.0 <sup>+0.3</sup> <sub>-0.4</sub>	0.16 <sup>+0.05</sup> <sub>-0.15</sub>
NT77_1	20.0 <sup>6</sup>	190 <sup>+20</sup> <sub>-10</sub>	2.7±0.0 <sup>6</sup>	17.3 <sup>+0.06</sup> <sub>-0.1</sub>	190 <sup>+20</sup> <sub>-10</sub>	3.2±0.1	16.1 <sup>+0.6</sup> <sub>-0.2</sub>	50±20	4.3 <sup>+0.6</sup> <sub>-0.4</sub>	16.9 <sup>+1.1</sup> <sub>-0.6</sub>	0.74 <sup>+0.49</sup> <sub>-0.26</sub>
PDR1_NW_1	21.1 <sup>6</sup>	30±10	3.7±0.0 <sup>6</sup>	17.8 <sup>+0.3</sup> <sub>-0.3</sub>	30±10	4.4 <sup>+0.2</sup> <sub>-0.1</sub>	16.6 <sup>+0.3</sup> <sub>-0.2</sub>	30±10	4.4 <sup>+0.2</sup> <sub>-0.1</sub>	16.8 <sup>+0.7</sup> <sub>-0.2</sub>	0.79 <sup>+0.24</sup> <sub>-0.21</sub>
PDR2_NW_2	20.4 <sup>6</sup>	40±10	4.4±0.0	17.9 <sup>+0.2</sup> <sub>-0.3</sub>	40±10	5.9±0.1	16.1±0.2	40±10	5.9±0.1	16.5±0.2	0.11 <sup>+0.02</sup> <sub>-0.03</sub>
PDR2_NW_3	20.6 <sup>6</sup>	49	2.8	18.0±0.0 <sup>6</sup>	–	–	–	–	–	–	–
PDR2_NW_4	20.5 <sup>6</sup>	49	2.8	17.6±0.0 <sup>6</sup>	–	–	–	–	–	–	–
PDR3_NE_1	21.1 <sup>6</sup>	150±10	2.3±0.0 <sup>6</sup>	18.4±0.1	150±10	2.3±0.1	16.2 <sup>+0.2</sup> <sub>-0.3</sub>	60 <sup>+10</sup> <sub>-20</sub>	4.2 <sup>+0.2</sup> <sub>-0.3</sub>	16.8 <sup>+0.2</sup> <sub>-0.3</sub>	0.09 <sup>+0.02</sup> <sub>-0.04</sub>
PDR3_NE_2	20.9 <sup>6</sup>	170±10	3.4±0.0 <sup>6</sup>	17.5±0.0 <sup>6</sup>	170±10	4.5±0.1	16.6 <sup>+0.2</sup> <sub>-0.3</sub>	40±10	4.5±0.4	17.3 <sup>+0.2</sup> <sub>-0.3</sub>	0.38 <sup>+0.08</sup> <sub>-0.28</sub>
PDR3_NE_3	21.4 <sup>6</sup>	49	2.8	18.3±0.0 <sup>6</sup>	–	–	–	–	–	–	–
PDR4_RIDGE_1	21.0 <sup>6</sup>	80±20	2.7±0.0 <sup>6</sup>	17.5 <sup>+0.1</sup> <sub>-0.2</sub>	80±20	2.8±0.1	16.7 <sup>+0.3</sup> <sub>-0.5</sub>	30±10	4.6 <sup>+0.7</sup> <sub>-0.4</sub>	17.2 <sup>+0.4</sup> <sub>-0.6</sub>	0.40 <sup>+0.16</sup> <sub>-0.60</sub>
SK-66D35_2	21.0 <sup>6</sup>	49	2.8	17.1±0.1	–	–	–	–	–	–	–
SK-68D140_1	21.1 <sup>6</sup>	49	2.8	17.2±0.1	–	–	–	–	–	–	–
SK-68D155_1	20.8 <sup>6</sup>	49	2.8	17.6±0.0 <sup>6</sup>	–	–	–	–	–	–	–
SK-69D228_1	20.8 <sup>6</sup>	49	2.8	17.1±0.1	–	–	–	–	–	–	–
Small Magellanic Cloud											
AzV18_1	21.5 <sup>6</sup>	49	3.3	17.1±0.1	–	–	–	–	–	–	–
AzV18_2	21.1 <sup>6</sup>	49	3.3	16.9±0.1	–	–	–	–	–	–	–
SMC_B2.6.1	21.1 <sup>6</sup>	160±10	2.9±0.0 <sup>6</sup>	17.4±0.1	160±10	3.1±0.1	16.1 <sup>+0.3</sup> <sub>-0.5</sub>	–	4.1 <sup>+0.3</sup> <sub>-0.2</sub>	16.4 <sup>+0.4</sup> <sub>-0.6</sub>	0.06 <sup>+0.03</sup> <sub>-0.07</sub>
SMC_B2.6.2	21.4 <sup>6</sup>	49	3.3	17.1±0.1	–	–	–	–	–	–	–
SMC_HI.4.1	21.3 <sup>6</sup>	49	3.3	17.1±0.0 <sup>6</sup>	–	–	–	–	–	–	–
SMC_HI.4.2	21.0 <sup>6</sup>	49	3.3	16.7±0.1	–	–	–	–	–	–	–
SMC_LIRS36_1	20.8 <sup>6</sup>	60±10	3.5±0.0 <sup>6</sup>	17.5±0.1	60±10	3.8±0.1	16.4 <sup>+0.4</sup> <sub>-0.1</sub>	–	4.3 <sup>+0.4</sup> <sub>-0.2</sub>	16.9 <sup>+0.8</sup> <sub>-0.3</sub>	0.89 <sup>+0.42</sup> <sub>-0.11</sub>
SMC_LIRS49_1	20.9 <sup>6</sup>	49	3.3	17.2±0.0 <sup>6</sup>	–	–	–	–	–	–	–
SMC_LIRS49_2	21.0 <sup>6</sup>	50±10	3.1±0.0 <sup>6</sup>	17.8 <sup>+0.1</sup> <sub>-0.2</sub>	50±10	3.0±0.1	16.5±0.4	–	4.4±0.3	16.8 <sup>+0.8</sup> <sub>-0.6</sub>	0.51 <sup>+0.26</sup> <sub>-0.49</sub>
SMC_LIRS49_3	21.3 <sup>6</sup>	50±10	3.8 <sup>+0.1</sup> <sub>-0.06</sub>	16.8 <sup>+0.1</sup> <sub>-0.2</sub>	–	–	–	–	4.3 <sup>+0.3</sup> <sub>-0.1</sub>	16.3 <sup>+0.4</sup> <sub>-0.5</sub>	0.15 <sup>+0.03</sup> <sub>-0.24</sub>
SMC_LIRS49_4	20.5 <sup>6</sup>	49	3.3	16.6±0.0 <sup>6</sup>	–	–	–	–	–	–	–
SMC_NE_1a_1	21.0 <sup>6</sup>	110±10	3.3	16.7±0.1	110±10	3.6±0.1	15.8 <sup>+0.1</sup> <sub>-0.2</sub>	–	3.9 <sup>+0.3</sup> <sub>-0.2</sub>	16.6 <sup>+0.3</sup> <sub>-0.2</sub>	0.12 <sup>+0.007</sup> <sub>-0.05</sub>
SMC_NE_3c_1	20.5 <sup>6</sup>	40±10	3.3±0.0	16.6 <sup>+0.2</sup> <sub>-0.4</sub>	40±10	3.3±0.1	16.3 <sup>+0.3</sup> <sub>-1.0</sub>	–	3.5 <sup>+0.7</sup> <sub>-0.1</sub>	16.5 <sup>+0.4</sup> <sub>-1.0</sub>	0.06 <sup>+0.03</sup> <sub>-0.42</sub>
SMC_NE_3g_1	21.1 <sup>6</sup>	190±10	3.0±0.0 <sup>6</sup>	16.6±0.1	190±10	3.3±0.1	15.9±0.3	–	3.4±0.1	16.4±0.3	0.03±0.01
SMC_NE_4a_hi_2	20.4 <sup>6</sup>	20±10	3.8 <sup>+0.06</sup> <sub>-0.1</sub>	17.5 <sup>+0.7</sup> <sub>-2.0</sub>	20±10	4.0±0.1	15.9 <sup>+0.1</sup> <sub>-0.2</sub>	–	4.0±0.1	16.2 <sup>+0.1</sup> <sub>-0.2</sub>	0.10 <sup>+0.007</sup> <sub>-0.02</sub>
SMC_NE_4a_hi_3	21.0 <sup>6</sup>	49	3.3	16.3 <sup>+0.3</sup> <sub>-0.2</sub>	–	–	–	–	–	–	–
SMC_NE_4c_low_1	21.2 <sup>6</sup>	30 <sup>+10</sup> <sub>-20</sub>	2.8±0.0 <sup>6</sup>	17.4 <sup>+0.7</sup> <sub>-0.8</sub>	30 <sup>+10</sup> <sub>-20</sub>	2.1 <sup>+0.1</sup> <sub>-0.2</sub>	16.4 <sup>+0.5</sup> <sub>-0.4</sub>	–	2.1 <sup>+0.1</sup> <sub>-0.2</sub>	17.1 <sup>+0.6</sup> <sub>-0.5</sub>	0.15 <sup>+0.09</sup> <sub>-0.17</sub>

<sup>1</sup> H<sup>0</sup> column density derived from the integrated intensity of the H I 21 cm line over the velocity range defined by the FWHM of the [C II] velocity components (see Section 3.2).

<sup>2</sup> Kinetic temperature of the H<sub>2</sub> gas associated with C<sup>+</sup> (Section 4.4.3), C<sup>0</sup> (Section 4.4.2), and CO (Section 4.4.1).

<sup>3</sup> Volume density of the H<sub>2</sub> gas associated with C<sup>+</sup> (Section 4.4.3), C<sup>0</sup> (Section 4.4.2), and CO (Section 4.4.1).

<sup>4</sup> C<sup>+</sup> (Section 4.4.3), C<sup>0</sup> (Section 4.4.2), and CO (Section 4.4.1) column densities associated with H<sub>2</sub> gas.

<sup>5</sup> Filling factor of the [C I] and CO-emitting layers derived from <sup>13</sup>CO observations in Section 4.4.

<sup>6</sup> The uncertainty is below 0.05.

<sup>7</sup> The uncertainty is below 0.005.

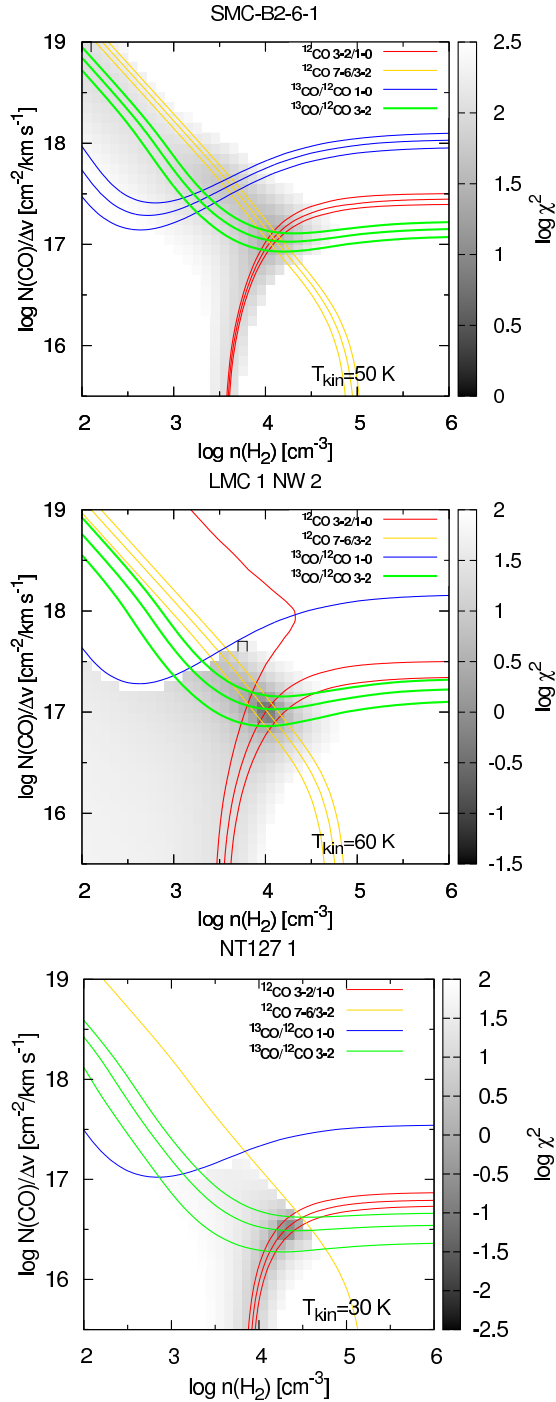


FIG. 9.— Sample comparison between the observed CO and  $^{13}\text{CO}$  line ratios and the predictions from the RADEX model. The lines represent the observed line ratios  $\pm$  the uncertainties in their determination. The comparisons are shown at the kinetic temperature at which the minimum value of  $\chi^2_{\text{total,min}}$  is located. In the middle and lower panels we show cases where the  $3\sigma$  upper limit of the  $^{13}\text{CO } J = 1 \rightarrow 0/^{12}\text{CO } J = 1 \rightarrow 0$  and/or the  $^{12}\text{CO } J = 7 \rightarrow 6/J = 3 \rightarrow 2$  ratios are used to discard solutions.

cm<sup>-3</sup>, both in steps of 0.1 dex. In our calculations, we initially assumed  $\Delta v = 1 \text{ km s}^{-1}$ , but later converted the constrained  $N_{\text{CO}}/\Delta v$  and  $N_{\text{CO}}/\Delta v$  to total C<sup>0</sup> and CO column density by multiplying by the line FWHM resulting from the Gaussian fit in each velocity component. For velocity components where the lines in the numer-

ator of the line ratios are not detected but those in the denominator are, we use the  $3\sigma$  upper limits of the lines in the numerator to calculate line ratios which are used to discard solutions in the RADEX grids (Figure 9). In Table 5, we summarize the physical parameters derived in the LMC and SMC. We only list velocity components where the [C II] line is detected.

We quantified how a RADEX model  $M(T_{\text{kin}}, N_{\text{CO}}/\Delta v, n_{\text{H}_2})$  reproduces a given line ratio  $R$  with uncertainty  $\sigma_R$  by calculating  $\chi_R^2 = \sum_i (R - M_i)^2 / \sigma_R^2$  over the entire model grid. We later added the resulting  $\chi_R^2$  for all line ratios available in a given velocity component to determine a total  $\chi^2_{\text{total}}$ . We then identified the best matching model by searching for the minimum  $\chi^2_{\text{total}}$  in the model grid,  $\chi^2_{\text{total,min}}$ . To determine the uncertainties in the derived parameters, we defined a region in the parameter space where models have a  $\chi^2_{\text{total}}$  that is within three times the minimum  $\chi^2_{\text{total,min}}$ . We then determined the range of possible values of a given parameter within this region when the other two are fixed. For well constrained models,  $\chi^2_{\text{total,min}}$  can be very small and the adjacent models in the parameter space often have  $\chi^2_{\text{total}}$  that are higher than  $3\chi^2_{\text{total,min}}$ . In this case the accuracy in which a model parameter can be determined is given by the step size of the model grid.

We studied the effect of beam dilution in the line ratios used our analysis in Appendix A. Note that we do not correct the line ratios for beam dilution effects in our analysis, due to the uncertainties of whether dust continuum emission traces the distribution of gas. In Table 6, we present the effect of beam dilution in the line ratios that are calculated using observations at different angular resolutions. We find that these line ratios typically show a 10% variation. This small variation suggest that the observed structures are relatively extended at the resolution of our observations. In Table 7, we summarize the impact of the variation in the line ratios due to beam dilution in the derived physical properties of the C<sup>0</sup> and CO layers. The kinetic temperature, column density, and filling factor of the C<sup>0</sup> and CO layers are typically affected by factors between 1.1 to 1.6. The largest impact of the variation in the line ratios is in the derived H<sub>2</sub> volume density with variations between 1.5 and 4. Note that the largest variation we see, in the resulting H<sub>2</sub> volume density of CO gas in the LMC, is dominated by three sources, PDR4\_RIDGE\_1, PDR3\_NW, and NT77, which vary by factors of 25, 8, and 8, respectively. Without these three sources we find typical variations of a factor 1.6 for  $n_{\text{H}_2}^{\text{CO}}$  in the LMC.

#### 4.4.1. CO-emitting layer

We start by deriving the excitation conditions of the CO-emitting cloud layer. Depending on availability, we compared the observed  $^{12}\text{CO } J = 7 \rightarrow 6/J = 3 \rightarrow 2$ ,  $^{12}\text{CO } J = 3 \rightarrow 2/1 \rightarrow 0$ ,  $^{13}\text{CO } J = 3 \rightarrow 2/^{12}\text{CO } J = 3 \rightarrow 2$ , and  $^{13}\text{CO } J = 1 \rightarrow 0/^{12}\text{CO } J = 1 \rightarrow 0$  intensity ratios with the predictions from a grid of RADEX models. In Figure 9 we show an example of the comparison between the model grid and the observed line ratios. We assumed a  $^{12}\text{CO}/^{13}\text{CO}$  abundance ratio of 49 derived in the N113 region in the LMC by Wang et al. (2009).

Note that there are several velocity components in the

TABLE 6  
 BEAM DILUTION EFFECT ON LINE RATIOS

Ratio <sup>1</sup>	$\Theta_a/\Theta_b^2$	LMC <sup>3</sup>	SMC <sup>3</sup>
$^{12}\text{CO } J = 7 \rightarrow 6/J = 3 \rightarrow 2$	26.5''/17.5''	1.07	1.08
$^{12}\text{CO } J = 3 \rightarrow 2/J = 1 \rightarrow 0$	17.5''/33''	1.11	1.11
$[\text{C I}] \ ^3\text{P}_2 \rightarrow \ ^3\text{P}_1/\ ^3\text{P}_1 \rightarrow \ ^3\text{P}_0$	26.5''/44''	1.09	1.05

<sup>1</sup> Line ratio involving spectral lines observed at different angular resolutions.

<sup>2</sup> Angular resolution of the spectra line in the numerator and denominator of the line ratio.

<sup>3</sup> Average variation in a line ratio due to beam dilution effects.

 TABLE 7  
 IMPACT OF BEAM DILUTION EFFECTS ON  
 DERIVED PHYSICAL PARAMETERS

Physical parameter	LMC <sup>1</sup>	SMC <sup>1</sup>
$N(\text{C}^0)$	1.2	1.5
$N(\text{CO})$	1.4	1.1
$n_{\text{H}_2}^{\text{C}^0}$	2.2	3.2
$n_{\text{H}_2}^{\text{CO}}$	4	1.5
$T_{\text{kin}}^{\text{C}^0}$	1.2	1.3
$T_{\text{kin}}^{\text{CO}}$	1.5	1.6
filling factor	1.4	1.2

<sup>1</sup> Average variation on the physical parameter resulting from beam dilution effects.

LMC and SMC where  $^{12}\text{CO } J = 1 \rightarrow 0$  was detected but where  $^{13}\text{CO } J = 1 \rightarrow 0$  and/or  $^{13}\text{CO } J = 3 \rightarrow 2$  were not detected. We were thus unable to derive the physical conditions of the CO-emitting layer in these LOSs. These LOSs are likely diffuse (see Section 3.3), as  $^{12}\text{CO } J = 1 \rightarrow 0$  is known to be detectable even in low column density regions, where  $^{13}\text{CO } J = 1 \rightarrow 0$  is not detected, and CO is not the dominant form of gas-phase carbon (Pineda et al. 2010).

We find that single component models often provide a reasonable fit to the observed line ratios in our sample. There are however some indications by the  $^{12}\text{CO}/^{13}\text{CO}$  ratios of a colder gas component. When a best fitting model is identified, we compare the observed  $^{13}\text{CO } J = 3 \rightarrow 2$  intensities, assuming this line to be optically thin, with those predicted by the model to estimate the beam filling factor. If the  $^{13}\text{CO } J = 3 \rightarrow 2$  is not detected, we use instead the  $^{13}\text{CO } J = 1 \rightarrow 0$  when available. We derived physical conditions of 23 velocity components in 20 LOSs where at least two pairs of line ratios could be calculated. The average value and standard deviation of the physical conditions in the sample are  $43 \pm 19$  K in the LMC and  $50 \pm 20$  K in the SMC for the kinetic temperature,  $10^{16.7 \pm 0.5} \text{ cm}^{-2}$  in the LMC and  $10^{16.6 \pm 0.3} \text{ cm}^{-2}$  in the SMC for the beam-averaged CO column density,  $10^{5.1 \pm 0.9} \text{ cm}^{-3}$  in the LMC and  $10^{4.0 \pm 0.3} \text{ cm}^{-3}$  in the SMC for the  $\text{H}_2$  volume density, and  $(0.2 \pm 0.2)$  in the LMC and  $(0.20 \pm 0.3)$  in the SMC for the filling factor.

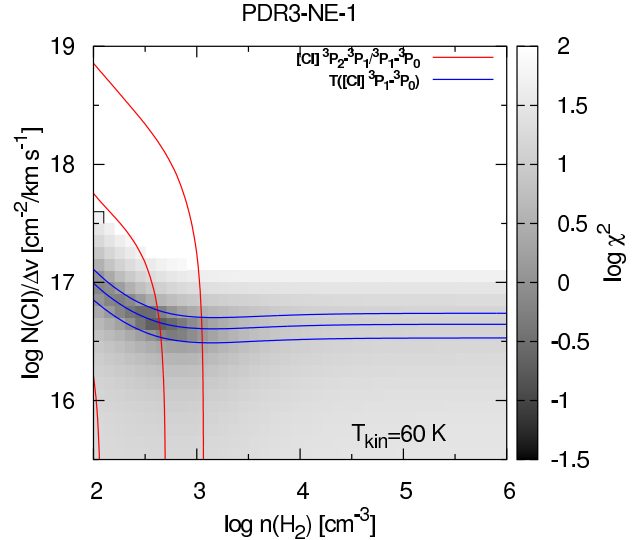


FIG. 10.— Sample comparison between the  $[\text{C I}] \ ^3\text{P}_2 \rightarrow \ ^3\text{P}_1/\ ^3\text{P}_1 \rightarrow \ ^3\text{P}_0$  line intensity ratio and the peak intensity of the  $[\text{C I}] \ ^3\text{P}_1 \rightarrow \ ^3\text{P}_0$  line with the grid of RADEX models. The comparison is shown at the kinetic temperature at which the minimum value of  $\chi^2$  is found.

#### 4.4.2. [C I]-emitting layer

We constrain the volume and column density and kinetic temperature of the [C I]-emitting layer comparing the observed  $[\text{C I}] \ ^3\text{P}_2 \rightarrow \ ^3\text{P}_1/\ ^3\text{P}_1 \rightarrow \ ^3\text{P}_0$  line intensity ratio and the peak intensity of the  $[\text{C I}] \ ^3\text{P}_1 \rightarrow \ ^3\text{P}_0$  line with the grid of RADEX models. We show a sample comparison between observations and models in Figure 10.

For kinetic temperatures above  $\sim 50$  K and  $\text{C}^0$  column densities per velocity interval below  $\sim 10^{18} \text{ cm}^{-2} (\text{K km s}^{-1})^{-1}$ , a typical range of solutions found in the [C I]-emitting layer, the  $[\text{C I}] \ ^3\text{P}_2 \rightarrow \ ^3\text{P}_1/\ ^3\text{P}_1 \rightarrow \ ^3\text{P}_0$  ratio provides a good constraint on the volume density of the [C I]-emitting gas. The peak intensity of the  $[\text{C I}] \ ^3\text{P}_1 \rightarrow \ ^3\text{P}_0$ , corrected by the filling factor derived in the CO-emitting layer, depends mostly on the  $\text{C}^0$  column density per velocity interval, and thus constrain  $N(\text{C}^0)/\Delta v$ . The multiplication by a filling factor is appropriate because, in the range of kinetic temperatures and  $\text{H}_2$  densities inferred in our analysis, the  $[\text{C I}] \ ^3\text{P}_1 - \ ^3\text{P}_0$  line is likely optically thin.

While the [C I] lines typically provide good constraints on the column and volume density of the [C I]-emitting gas, the kinetic temperature is not well constrained. We therefore further constrain the solutions by requiring that the [C I]-emitting region must have a lower or equal volume density and higher or equal kinetic temperature than the CO-emitting layer. This assumption is justified as we expect that [C I] and mid- $J$  CO lines are emitted from adjacent layers in a PDR-like structure<sup>10</sup>, where the neutral carbon is located in a somewhat warmer region with equal or lower volume density compared to the one at which CO is located, and that the cloud's volume density profile is smooth.

There are some velocity components where only the

<sup>10</sup> For an example of a typical temperature distribution and abundance structure of the main carbon species in PDRs, see e.g. Figures 7 and 9 in Tielens & Hollenbach (1985).

[C I]  $^3P_1 \rightarrow ^3P_0$  line is detected, and therefore we can only calculate a  $3\sigma$  upper limit to the [C I]  $^3P_2 \rightarrow ^3P_1$ / $^3P_1 \rightarrow ^3P_0$  ratio. In these cases we assume that the kinetic temperature and volume density at the [C I]-emitting layer are the same as those at the CO-emitting layer and we use the [C I]  $^3P_1 \rightarrow ^3P_0$ , corrected with its corresponding filling factor, to constrain the  $C^0$  column density per velocity interval.

We derived physical conditions of 22 velocity components in 20 LOSs. The average value and standard deviation of the physical conditions in the [C I]-emitting layer are  $91 \pm 60$  K in the LMC and  $73 \pm 62$  in the SMC for the kinetic temperature,  $10^{16.4 \pm 0.4} \text{ cm}^{-2}$  in the LMC and  $10^{16.2 \pm 0.3} \text{ cm}^{-2}$  in the SMC for the beam-averaged  $C^0$  column density, and  $10^{4.8 \pm 1.4} \text{ cm}^{-3}$  in the LMC and  $10^{3.5 \pm 0.5} \text{ cm}^{-3}$  in the SMC for the  $H_2$  volume density.

#### 4.4.3. [C II]-emitting layer

As mentioned above, the observed [C II] emission is the result of the combined emission from molecular, atomic, and ionized gas. In Section 3.1 and 3.2 we estimated the physical conditions of the ionized and atomic gas associated with  $C^+$  to determine their contribution to the observed [C II] emission. In the following, we describe the derivation of the physical conditions of the [C II]-emitting gas associated with molecular gas.

We estimated the volume density of the [C II]-emitting layer associated with molecular hydrogen assuming a thermal pressure and a kinetic temperature. In Section 4.3, we estimated the typical thermal pressure of the diffuse gas of  $3.4 \times 10^4 \text{ K cm}^{-3}$  and  $1 \times 10^5 \text{ K cm}^{-3}$ , in the LMC and SMC, respectively. In LOS where H I and [C II] are detected, but neither [C I], CO, nor  $^{13}\text{CO}$  emission are detected, we assume the derived diffuse ISM pressure and a kinetic temperature of 49 K (Section 3.4) to derive a typical volume density of 694 and  $2040 \text{ cm}^{-3}$  for the LMC and SMC, respectively. We also apply this criteria to LOSs where weak CO emission is detected but no  $^{13}\text{CO}$  was detected.

For velocity components where we were able to determine the physical conditions of the [C I]-emitting or  $^{12}\text{CO}$ -emitting layer, we use a thermal pressure for the [C II] emitting layer that is the geometrical mean between the diffuse ISM pressure derived in Section 4.3 and that of the [C I]-emitting or that of the  $^{12}\text{CO}$ -emitting layer, in case we were not able to determine the conditions at the [C I]-emitting layer. For the kinetic temperature we assume 49 K in case the temperature of the denser molecular gas is lower than or equal to this temperature. We adopt the kinetic temperature of the denser molecular gas in the case it is larger than 49 K. With these two assumptions, we derive typical volume densities (and standard deviations) of  $10^{3.1 \pm 0.5} \text{ cm}^{-3}$  for the LMC and  $10^{3.2 \pm 0.2} \text{ cm}^{-3}$  for the SMC.

With the estimated volume density and kinetic temperatures of the [C II]-emitting layer, we use Equation (2) to derive the  $C^+$  column density for each velocity component. Typical values of the beam-averaged column densities are  $10^{17.4 \pm 0.3} \text{ cm}^{-2}$  and  $10^{17.0 \pm 0.2} \text{ cm}^{-2}$  for the LMC and SMC, respectively.

## 5. DISCUSSION

### 5.1. The H to $H_2$ transition

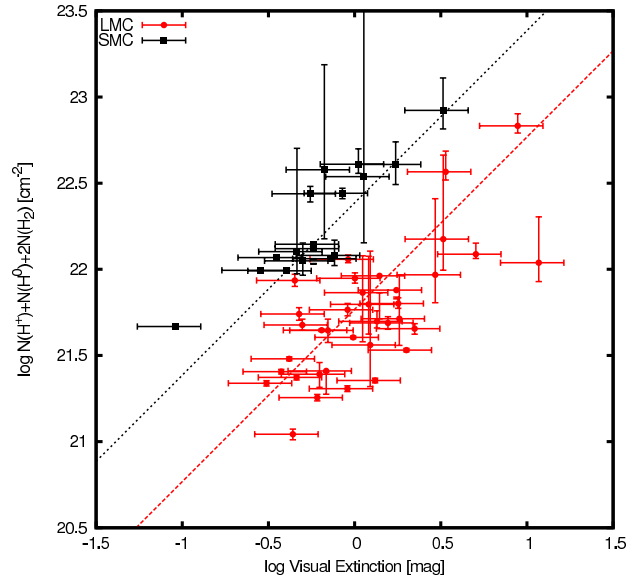


FIG. 11.— Comparison between the  $N(\text{H}^+) + N(\text{H}^0) + 2N(\text{H}_2)$  hydrogen column densities derived in this study and the visual extinction derived from dust continuum observations. The straight lines represent the total hydrogen column density predicted for a given  $A_V$  assuming  $N(\text{H})/A_V = 7.17 \times 10^{21} \text{ cm}^{-2} \text{ mag}^{-1}$  for the LMC and  $1.68 \times 10^{22} \text{ cm}^{-2} \text{ mag}^{-1}$  for the SMC (Section 4.2).

The abundance of molecular hydrogen in interstellar clouds is set by the balance between  $H_2$  formation on dust grains and photo-destruction by the ambient FUV photons. The gas transitions from being  $\text{H}^0$ -dominated to  $\text{H}_2$ -dominated when the dust column density is large enough to allow  $\text{H}_2$  self shielding to halt photo-destruction, leading to a rapid increase of the  $\text{H}_2$  abundance (e.g. Gnedin et al. 2009; Krumholz et al. 2009; Sternberg et al. 2014; Bialy & Sternberg 2016). The transition between atomic to molecular hydrogen marks the onset of the formation of molecular clouds and therefore has important implications in star formation and galaxy evolution.

The atomic gas component in clouds is often traced by observations of the H I 21 cm line, while molecular gas is determined by observing the  $^{12}\text{CO } J = 1 \rightarrow 0$  line which is converted to a  $\text{H}_2$  column density using a  $X_{\text{CO}}$  conversion factor. CO observations, however, trace mostly well-shielded regions and the diffuse  $\text{H}_2$  component (CO-dark  $\text{H}_2$ ) is not well probed. Diffuse  $\text{H}_2$  has been observed in absorption against stars in the far-ultraviolet (e.g. Tumlinson et al. 2002; Cartledge et al. 2005; Sheffer et al. 2008; Welty et al. 2012), but is limited to individual lines-of-sight and tends to trace low  $\text{H}_2$  column densities, as lines-of-sight with higher molecular content will absorb the starlight required for reliable FUSE measurements. [C II] observations, which can potentially image large regions in the Magellanic clouds, can be used to trace the CO-dark  $\text{H}_2$  component and to study how it relates to the atomic gas.

We study the transition from atomic to molecular gas in the Magellanic clouds by estimating the column density of H,  $N(\text{H}^0)$ , and of  $\text{H}_2$ ,  $N(\text{H}_2)$  in our sample. As discussed in Section 3.2, we estimated the column density of atomic hydrogen using  $N(\text{H}^0) = 1.82 \times 10^{18} I(\text{HI}) \text{ cm}^{-2}$ , with  $I(\text{HI})$  in units of  $\text{K km s}^{-1}$ . The typical uncertainty in the  $\text{H}^0$  column density is  $10^{19.8} \text{ cm}^{-2}$ . To calculate



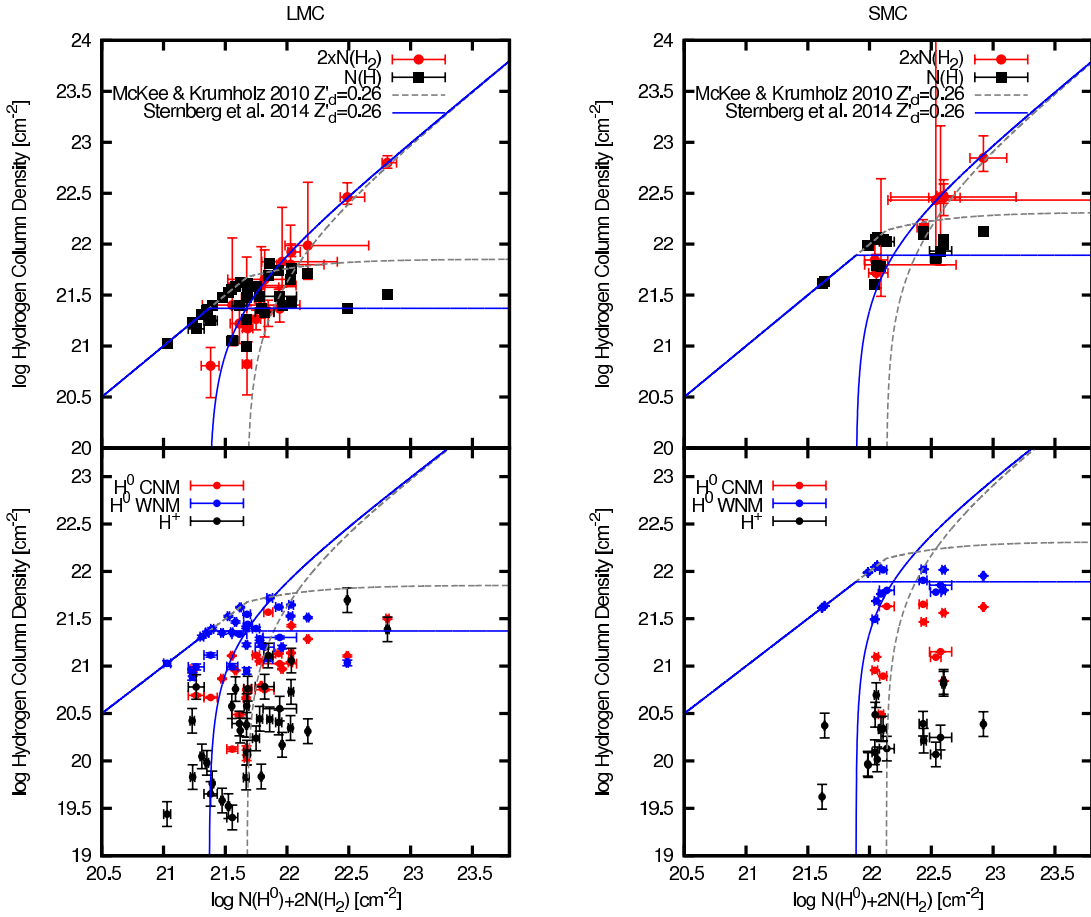


FIG. 12.— (*upper panels*) The column densities of  $\text{H}^0$  and  $\text{H}_2$  as a function of the total hydrogen column density,  $N(\text{H}^0)+2N(\text{H}_2)$ , for LOSs in the LMC (*left*) and SMC (*right*). (*lower panels*) The column densities of  $\text{H}^+$  and  $\text{H}^0$  decomposed in CNM and WNM gas as a function of the total hydrogen column density for LOSs in the LMC (*left*) and SMC (*right*). In all panels the dashed-dotted line indicates the predictions for  $N(\text{H}^0)$ , and the dashed line for  $N(\text{H}_2)$ , from the model of Sternberg et al. (2014) and McKee & Krumholz (2010) for  $Z'_d = 0.26$  and  $\chi_0=1.3$  for the LMC and  $Z'_d = 0.1$  and  $\chi_0=1.9$  for the SMC (see Section 5.1).

the  $\text{H}_2$  column density, we first calculate the total carbon column density,  $N^{\text{total}}(\text{C}) = N(\text{C}^+)_{\text{H}_2} + N(\text{C}^0) + N(\text{CO})$ , with  $N(\text{C}^+)_{\text{H}_2}$  being the column density of  $\text{C}^+$  associated with  $\text{H}_2$  (Section 4.4.3). We converted from  $N^{\text{total}}(\text{C})$  to  $N(\text{H}_2)$  applying the gas-phase carbon fractional abundances for the LMC and SMC discussed in Section 3. The estimated  $N(\text{H}_2)$  can include well shielded gas, associated with  $\text{C}^0$  and  $\text{CO}$ , as well as the diffuse  $\text{CO}$ -dark  $\text{H}_2$  gas, associated with  $\text{C}^+$ . The uncertainties in  $N(\text{H}_2)$  are the result of the propagation of those from  $N(\text{C}^+)$ ,  $N(\text{C}^0)$ ,  $N(\text{CO})$ . For  $N(\text{C}^+)$  the uncertainty is given by the propagation of the errors in the integrated intensity of the  $[\text{C II}]$  line and the errors on the thermal pressures due to the uncertainties in the physical conditions of the  $[\text{C I}]$  or  $\text{CO}$  layer. The uncertainties of  $N(\text{C}^0)$  and  $N(\text{CO})$  are estimated as part of the excitation analysis described in Section 4.4.

In order to test our determination of the  $\text{H}^0$  and  $\text{H}_2$  column densities, in Figure 11, we show a comparison between the  $N(\text{H}^+) + N(\text{H}^0) + 2N(\text{H}_2)$  hydrogen column density derived from  $\text{H}\alpha$ ,  $\text{H I}$ ,  $[\text{C II}]$ ,  $[\text{C I}]$ , and  $\text{CO}$  observations and the visual extinction derived from dust continuum (Section 4.1). We include the  $N(\text{H}^+)$  column density to account for the contribution from ionized gas to  $A_V$ . Given the uncertainties in the assumptions used

to derive all quantities involved, we find a reasonable correspondence between  $N(\text{H}^+) + N(\text{H}^0) + 2N(\text{H}_2)$  and  $A_V$ , with a scaling that corresponds to the dust-to-gas ratio of the LMC and SMC discussed in Section 4.2.

Analytic theories for the atomic-to-molecular transition have been presented by Sternberg et al. (2014) and McKee & Krumholz (2010) (see also Krumholz et al. 2008 and Krumholz et al. 2009). Their work provides expressions for the molecular fraction as a function of total hydrogen column density (Eq. 97 for Sternberg et al. 2014 and Eq. 93 for McKee & Krumholz 2010) which can be used for comparison with our data. Both models assume a value of the strength of the FUV radiation field, and that the gas metallicity and dust-to-gas ratio scale by the same factor,  $Z'_d$ . These two parameters determine the total H column density at which the transition from  $\text{H}^0$  to  $\text{H}_2$  takes place, with higher column densities when the metallicity is reduced and/or the FUV radiation field is increased. Hughes et al. (2010) studied the strength of the FUV field across the LMC using the dust temperature maps presented by Bernard et al. (2008), finding an average value of  $\chi_0=1.3$ , in units of the local FUV radiation field calculated by Draine (1978), which is similar to that found in the Solar neighborhood. In the SMC, however, the strength of the FUV field is found to be larger

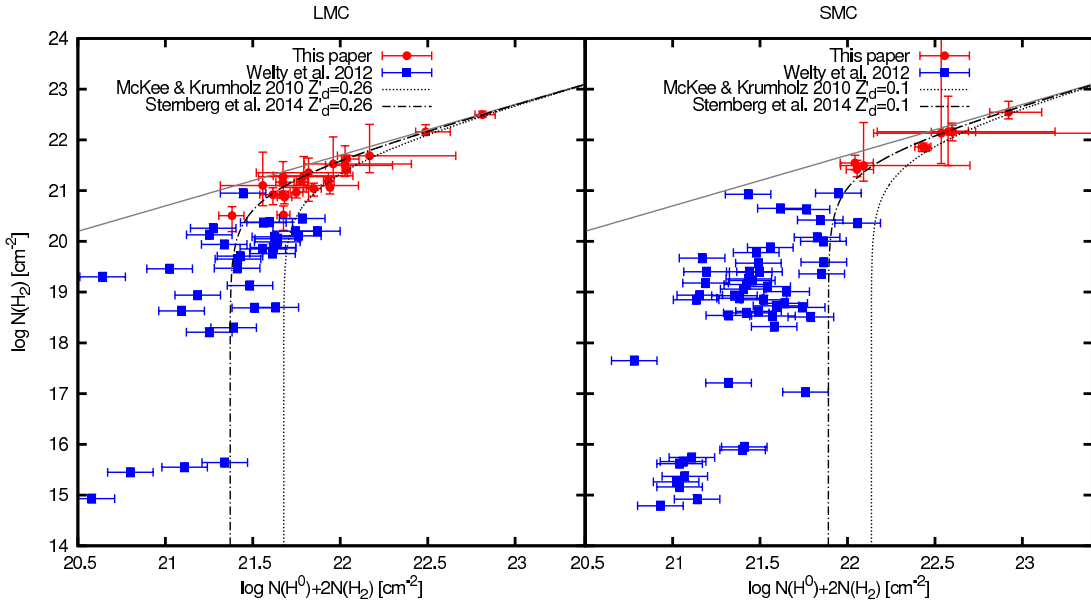


FIG. 13.— The column density of molecular hydrogen as a function of the total hydrogen column density,  $N(\text{H}^0)+2N(\text{H}_2)$ , for the values derived here and those observed in UV absorption for  $\text{H}_2$  and in optical absorption for  $\text{H}^0$  compiled by Welty et al. (2012). The straight line represents a molecular fraction of  $f(\text{H}_2)=1$ . We assume uncertainties of 10% for  $N(\text{H}^0)$  and of 20% for  $N(\text{H}_2)$  in the Welty et al. (2012) data. We also show the predictions from the models of Sternberg et al. (2014) and McKee & Krumholz (2010) for  $Z'_d = 0.26$  and  $\chi_0=1.3$  for the LMC and  $Z'_d = 0.1$  and  $\chi_0=1.9$  for the SMC (see Section 5.1).

than that in the Solar neighborhood and the LMC (e.g. Lequeux 1989). Li & Draine (2002) used IRAS, DIRBE, and ISO observations to constrain a dust model of the SMC, in which their best fit for the strength of the FUV field corresponds to  $\chi_0=1.9$ . We therefore adopt  $\chi_0=1.3$  and 1.9 for the LMC and SMC, respectively. Note that because we are adopting a single value of the FUV radiation field in our model calculations, we do not expect an exact match between model and derived column densities, as the FUV field is likely to vary among our LOSs. Both Hughes et al. (2010) and Li & Draine (2002) show variations of a factor  $\sim 2$  in the derived FUV radiation field in the LMC and SMC, respectively. Because the model predicted column density at which the  $\text{H}^0$  to  $\text{H}_2$  transition takes place is proportional to the FUV radiation field, variations in this quantity among our sample should result in a factor  $\sim 2$  scatter around the model predicted column density. This predicted scatter is consistent with that seen in our comparison between model and observed column densities (see Figures 12, 15, and 16). For the metallicity scaling, we adopt the scaling on the dust-to-gas ratio rather than of the carbon abundance, which are  $Z'=0.26$  for the LMC and 0.1 for the SMC. This assumption of using the dust-to-gas ratio is justified as the Sternberg et al. 2014 and McKee & Krumholz 2010 models focus on describing the chemical structure of the cloud (the  $\text{H}^0$  to  $\text{H}_2$  transition) which depends on the absorption of photons, and on the formation rate of  $\text{H}_2$ , on dust grains. These models, however, do not consider the thermal structure of the gas, which depends on the abundance of gas coolants. Thus the most relevant parameter in these models is the dust-to-gas ratio rather than the gas-phase abundances of elements.

As described in Sternberg et al. (2014), see their Figure 14, their theory differs from that of McKee & Krumholz (2010) in their consideration of shielding by dust asso-

ciated with both H and  $\text{H}_2$ , instead of only by dust associated with H in McKee & Krumholz (2010), and their assumption of a larger dust absorption cross section ( $\sigma_g=1.9\times 10^{-21}Z'\text{ cm}^{-2}$  vs  $1.0\times 10^{-21}Z'\text{ cm}^{-2}$ ). Additionally, they assumed a cloud geometry of a slab illuminated from both sides instead of the spherical geometry assumed by McKee & Krumholz (2010). They show that the differences between the two models are mostly explained by their consideration of absorption by dust associated with  $\text{H}_2$  and the larger dust absorption cross section they assume.

In the top panels of Figure 12, we show the column densities of  $\text{H}^0$  and  $\text{H}_2$  we have derived as a function of the  $\text{H}^0+2\text{H}_2$  column density. We also show the  $\text{H}^0$  and  $\text{H}_2$  column densities predicted by the McKee & Krumholz (2010) and Sternberg et al. (2014), as grey dashed and blue solid lines, respectively. We find that the Sternberg et al. (2014) model is in good agreement with the derived  $\text{H}^0$  and  $\text{H}_2$  column densities. The McKee & Krumholz (2010) model tends to predict lower  $\text{H}_2$  column densities for a given value of  $N_{\text{H}}$ . Note that the predicted column densities by the Sternberg et al. (2014) and McKee & Krumholz (2010) model are functions of the shielding column density, which is dominated by the cold neutral medium gas in the case of atomic gas. Thus, their predicted  $\text{H}^0$  column densities correspond to that of the CNM only, while the derived  $\text{H}^0$  column densities presented in the top panel of Figure 12 corresponds to the total  $\text{H}^0$  along the LOS with includes the contribution from both the WNM and CNM.

In the bottom panels of Figure 12, we show a decomposition of the  $\text{H}^0$  column density between WNM and CNM gas (see Section 3.2) and the contribution from  $\text{H}^+$  (Section 3.1). The Sternberg et al. (2014) and McKee & Krumholz (2010) models tend to overestimate the CNM column densities. It is, however, possible that we



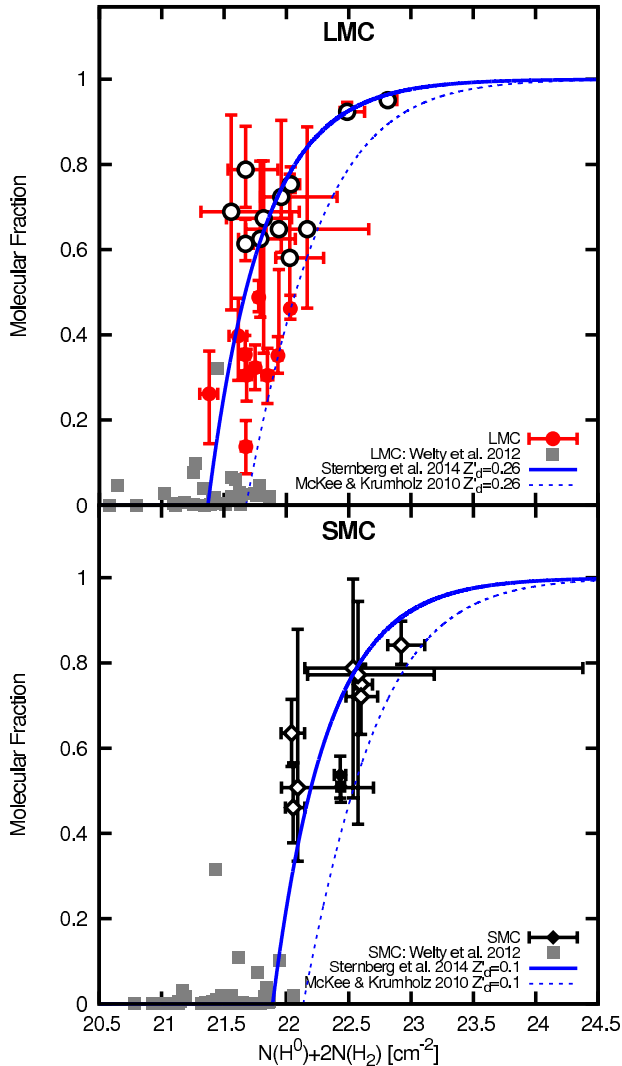


FIG. 14.— Molecular fraction (Equation 12) as a function of the total hydrogen for the LMC and SMC. The lines are the predictions from the models of Sternberg et al. (2014) and McKee & Krumholz (2010) for  $Z'_d = 0.26$  and  $\chi_0 = 1.3$  for the LMC and  $Z'_d = 0.1$  and  $\chi_0 = 1.9$  for the SMC (see Section 5.1). The filled circles and squares correspond to lines-of-sight where we derived the  $\text{H}_2$  column density from  $N(\text{C}^+)$  only while the open circles and squares represent LOSs where  $\text{C}^0$  and CO also contribute to the total carbon column density. We also include molecular fractions calculated from the sample of column densities observed in absorption in the FUV for  $\text{H}_2$  and in the optical for H I compiled by Welty et al. (2012). For clarity we do not show the error bars in the Welty et al. (2012) data. The uncertainties in the Welty et al. (2012) data are 30% for the total hydrogen column density and 36% for the molecular fraction based in the assumed uncertainties of 10% for  $N(\text{H}^0)$  and of 20% for  $N(\text{H}_2)$ .

are underestimating the CNM column density, as it can emit  $[\text{C II}]$  emission that is below the sensitivity of our observations. Most of the  $\text{H}^0$  in our sample is in the form of WNM. We estimate that the CNM typically represents 28% and 14% of the total  $\text{H}^0$  column density in the LMC and SMC, respectively. The f CNM fractions in the LMC and SMC are in good agreement with those derived in H I absorption studies by Dickey et al. (2000) using H I absorption against background continuum sources (33% for the LMC and 13% for the SMC; Dickey et al. 2000). Note that the CNM fractions derived

by Dickey et al. (2000) are proportional to the assumed kinetic temperature of the gas which in their case is 55 K. While the CNM fraction in the LMC is somewhat smaller than that found in Solar neighborhood (40% ; Heiles & Troland 2003; Pineda et al. 2013), this fraction is significantly smaller in the SMC. Dickey et al. (2000) argued that the low CNM fraction in the SMC is a result of the lower abundance of gas coolants while the reduction of the photoelectric heating efficiency due to the lower dust-to-gas ratio is offset by the enhanced FUV radiation field in the SMC (Lequeux 1989; Li & Draine 2002), resulting in warmer atomic gas. The  $\text{H}^+$  component plays a small role in the derived column densities.

We find that the thresholds where  $\text{H}_2$  formation becomes important are  $\sim 10^{21.5} \text{ cm}^{-2}$  for the LMC and  $\sim 10^{22} \text{ cm}^{-2}$  for the SMC. These correspond to  $35 M_\odot \text{ pc}^{-2}$  and  $110 M_\odot \text{ pc}^{-2}$  for the LMC and SMC, including the contribution from He, respectively. These values are higher than the Milky Way value of  $10 M_\odot \text{ pc}^{-2}$  (Krumholz et al. 2008), and reflect the lower dust-to-gas ratio of the LMC and SMC that reduces the rate of  $\text{H}_2$  formation for a given total hydrogen column density. Thus a larger hydrogen column is needed for  $\text{H}_2$  self-shielding to balance  $\text{H}_2$  photo-destruction, allowing the gas to transition to a mostly molecular phase in a low metallicity environment.

In Figure 13, we show the  $\text{H}_2$  column densities we derive together with those compiled for the LMC and SMC by Welty et al. (2012) as a function of the total hydrogen column density. For clarity, we exclude upper limits in the Welty et al. (2012) data. We also include the predictions of the model by Sternberg et al. (2014) and McKee & Krumholz (2010)<sup>11</sup>. In the LMC, the Sternberg et al. (2014) model is in good agreement with both the  $\text{H}_2$  column densities derived here and most of those compiled by Welty et al. (2012). In the SMC, however, the Sternberg et al. (2014) and McKee & Krumholz (2010) models are unable to reproduce the data points compiled by Welty et al. (2012) for  $N(\text{H}_2) \leq 10^{20} \text{ cm}^{-2}$ . A larger metallicity factor and/or a lower FUV radiation field (e.g.  $Z'_d = 0.2$  and  $\chi_0 = 1$  for the Sternberg et al. 2014 model) would be required for the theoretical models to reproduce these data points. We see that the column densities derived from  $[\text{C II}]$ ,  $[\text{C I}]$ , and CO provide a connection between the diffuse  $\text{H}_2$  detected by FUV absorption and the dense  $\text{H}_2$  in well-shielded regions. This connection is better illustrated in Figure 14, where we show the molecular fraction,

$$f(\text{H}_2) = \frac{2N(\text{H}_2)}{N(\text{H}^0) + 2N(\text{H}_2)}, \quad (12)$$

calculated for both our sample and that of Welty et al. (2012), as a function of the total hydrogen column density. We again include the predictions from the model of Sternberg et al. (2014) and McKee & Krumholz (2010). We see that the FUV absorption observations mostly trace  $f(\text{H}_2) \leq 0.2$  while our determination using  $[\text{C II}]$ ,

<sup>11</sup> Note that Welty et al. (2012) also compared their data set with the McKee & Krumholz (2010). The predictions plotted in their Figure 17 differ from those shown here, as they assumed a different metallicity/dust-to-gas ratio scaling factor of 0.5 and 0.2, for the LMC and SMC, respectively, and a FUV field of unity is implicitly assumed for both galaxies.

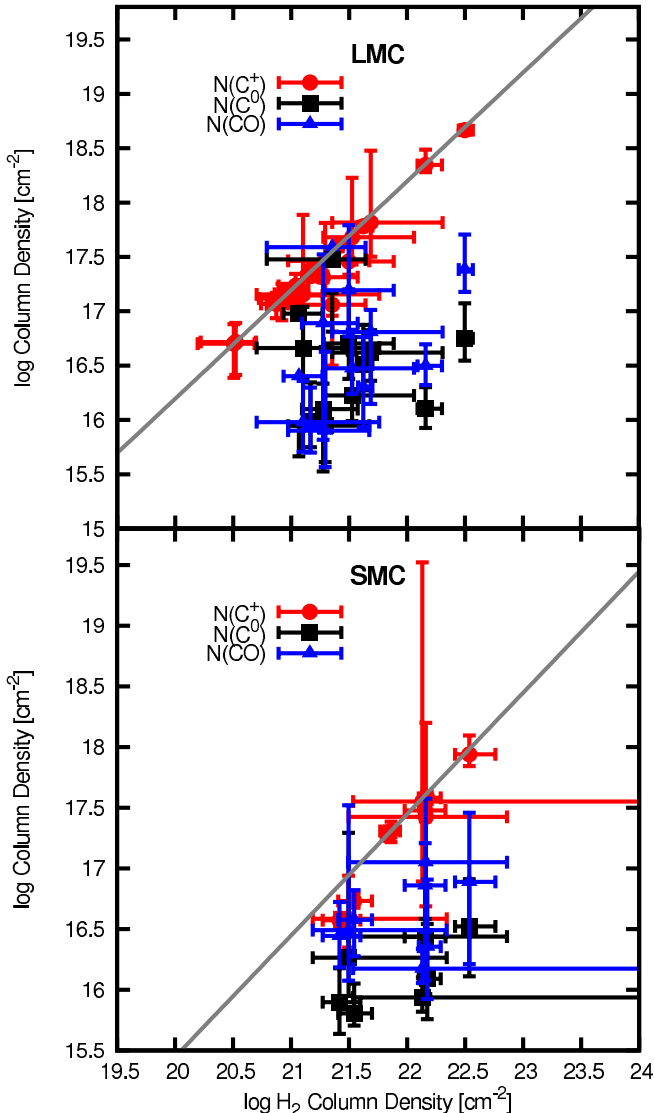


FIG. 15.— The  $C^+$ ,  $C^0$  and CO column densities associated with  $H_2$  gas as a function of the  $H_2$  column density derived in our sample in the (top) LMC and (bottom) SMC. The straight grey lines represent the total gas-phase carbon column density,  $N(C^+) + N(C^0) + N(CO)$ , that results by multiplying the  $H_2$  column density by the  $[C]/[H_2]$  abundance ratio of  $1.56 \times 10^{-4}$  for the LMC and  $2.8 \times 10^{-5}$  for the SMC (Section 3).

$[C I]$ , and CO observations traces the  $0.1 \leq f(H_2) \leq 1$  range. In Figure 14, we also separated LOSs where we derived the  $H_2$  column density from  $N(C^+)$  only from those where  $C^0$  and CO also contribute to the total carbon column density. We see that for molecular fractions  $f(H_2) \gtrsim 0.45$ , the  $C^0$ ,  $^{12}CO$ , and  $^{13}CO$  column densities are large enough for the detection of  $[C I]$ ,  $^{12}CO$ , and  $^{13}CO$  lines. The  $[C II]$  line alone traces a larger range in the molecular fraction down to 0.1. This result suggests that  $[C II]$  observations, together with that of  $[C I]$  and CO, are important tools for the study of the transition from atomic to molecular gas in the ISM of galaxies.

### 5.2. The $C^+$ to $C^0$ to CO transition

Another critical transition in interstellar clouds is that from ionized to neutral carbon and to the main molec-

ular form of carbon, CO. The  $C^+/C^0/CO$  layer is the interface between the diffuse CO-dark  $H_2$  gas and the dense molecular gas where star formation takes place. Therefore, it has an important role in the evolution of molecular clouds and star formation. The formation of CO in the gas phase is balanced by photo-destruction by FUV photons. The  $C^+/C^0/CO$  transition can take place if there is sufficient dust column density to efficiently shield the FUV photons that destroy CO. In low metallicity environments, the lower dust-to-gas ratio pushes the  $C^+/C^0/CO$  layer to higher hydrogen column densities. This effect has important implications in the ability of  $[C II]$ ,  $[C I]$ , and CO to trace the molecular hydrogen mass in clouds.

In Figure 15, we show a comparison between the  $H_2$  column density and the  $C^+$ ,  $C^0$ , and CO column densities associated with  $H_2$  derived in our sample in the LMC and SMC. The straight grey lines represent the total gas-phase carbon column density,  $N(C^+) + N(C^0) + N(CO)$ , that results by multiplying the  $H_2$  column density by the  $[C]/[H_2]$  abundance ratio of the LMC and SMC (Section 3). Ionized carbon is the dominant form of gas-phase carbon that is associated with molecular gas in our sample. Both neutral carbon and CO represent a lower fraction of the total carbon along the line-of-sight. The low column densities of CO and  $[C I]$  in our sample suggest that a large fraction of the gas column is associated with diffuse  $H_2$  gas.

We were able to determine  $C^0$  and CO column densities above  $N(H_2) \sim 10^{21} \text{ cm}^{-2}$  in the LMC and  $\sim 10^{21.5} \text{ cm}^{-2}$  in the SMC. The difference in these thresholds is likely influenced by the difference in metallicity and dust-to-gas ratio between the LMC and SMC. As we discussed in the previous section, the  $C^0$  and CO column densities have a measurable contribution to the total carbon abundance associated with  $H_2$  for  $f(H_2) \simeq 0.45$  in both the LMC and SMC.

In Figure 16, we show the fraction of  $C^+$ ,  $C^0$ , and CO to the total gas-phase carbon ( $C^+ + C^0 + CO$ ) abundance associated with  $H_2$  gas as a function of  $N(H_2)$ . Ionized carbon is the dominant form of carbon in our lines-of-sight in the LMC and SMC. On average,  $C^+$ ,  $C^0$ , and CO represent 89%, 9%, and 10% of the gas-phase carbon associated with molecular gas in the LMC and 77%, 6%, and 17% in the SMC, respectively.

### 5.3. The CO-to- $H_2$ conversion factor

The mass of molecular clouds in the Milky Way and external galaxies is often derived using observations of the  $^{12}CO J = 1 \rightarrow 0$  line together with an empirically derived CO-to- $H_2$  conversion factor,  $X_{CO} \equiv \frac{N(H_2)}{I_{CO}}$  (Bolatto et al. 2013, and references therein). The  $X_{CO}$  factor is calibrated in the Milky Way to be  $2 \times 10^{20} \text{ cm}^{-2} (\text{K km s}^{-1})^{-1}$ , but it is known to vary with environmental conditions, in particular with metallicity, which increases its value, as fainter CO emission per unit column density is observed (e.g. Rubio et al. 1993; Muller et al. 2010; Hughes et al. 2010; Leroy et al. 2007; Roman-Duval et al. 2014). In low-metallicity environments, the reduced dust-to-gas ratio results in an enhanced photo-destruction of CO, reducing the volume of  $H_2$  that is traced by CO. However, the calibration in the Galaxy accounts for regions where CO is not the dominant form

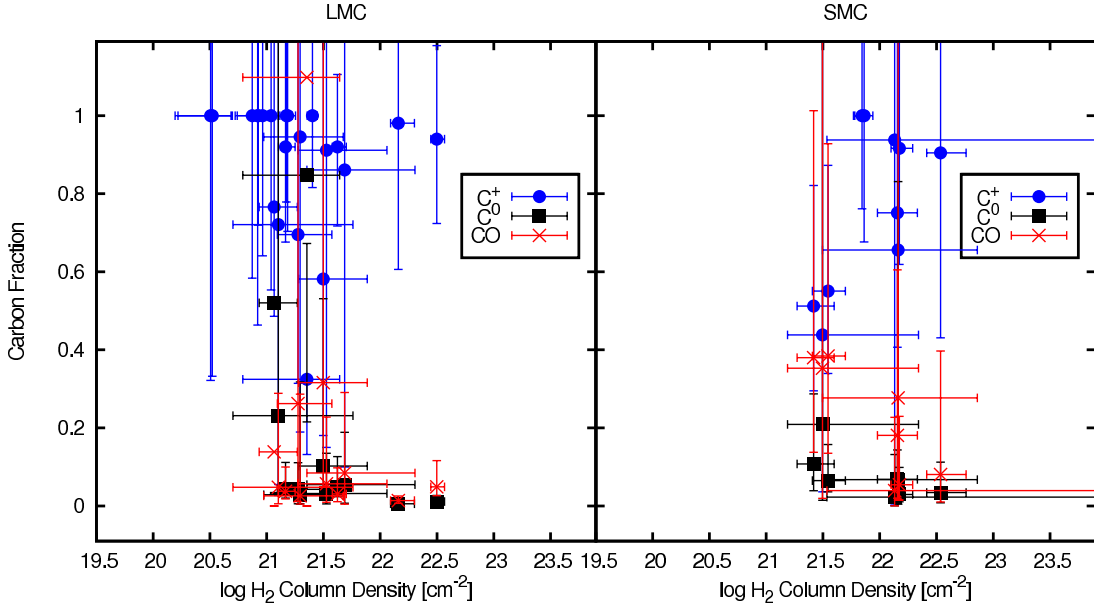


FIG. 16.— The fraction of  $C^+$ ,  $C^0$ , and CO with respect to the total carbon,  $C^+ + C^0 + CO$ , column density associated with  $H_2$  gas as a function of the  $H_2$  column density in the LMC (left) and SMC (right).

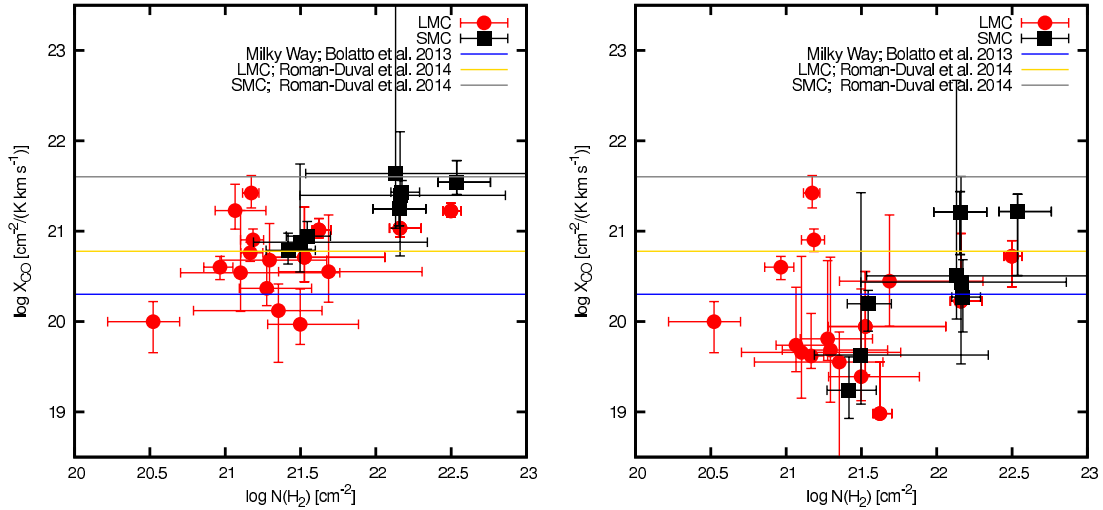


FIG. 17.— (left) The  $X_{CO}$  conversion factor as a function of the total  $H_2$  column density derived in Section 5.1 in our LMC and SMC sample. The horizontal lines correspond to  $X_{CO} = 2 \times 10^{20} \text{ cm}^{-2} (\text{K km s}^{-1})^{-1}$  compiled from several estimates in the Galaxy by Bolatto et al. (2013), and  $6 \times 10^{20} \text{ cm}^{-2} (\text{K km s}^{-1})^{-1}$  and  $4 \times 10^{21} \text{ cm}^{-2} (\text{K km s}^{-1})^{-1}$ , estimated by Roman-Duval et al. (2014) in the LMC and SMC, respectively. (right) The  $X_{CO}$  conversion factor as a function of the total  $H_2$  column density corrected by the filling factor of the CO-emitting gas derived in our sample (see Section 4.4.1).

of gas-phase carbon (Pineda et al. 2010). With our estimate of  $N(H_2)$  together with our  $^{12}\text{CO } J = 1 \rightarrow 0$  observations we can study the variation of  $X_{CO}$  as a function of metallicity in the LMC and SMC.

In the left panel of Figure 17 we show the  $X_{CO}$  conversion factor as a function of the total  $H_2$  column density in the LMC and SMC. We calculated  $X_{CO}$  by dividing the  $H_2$  column density (Section 5.1) by the CO integrated intensity, both corresponding to their total value along the line-of-sight. In the Figure, we show data points for all LOSs where CO was detected, including those where neither higher- $J$  nor isotopic transitions were detected (Section 4.4.1). In these LOSs, the  $H_2$  column density was derived from  $N(C^+)$ . While showing a large scatter, the values of  $X_{CO}$  in the LMC are consistent with,

and in the SMC somewhat lower than, those derived by Roman-Duval et al. (2014) of  $6 \times 10^{20} \text{ cm}^{-2} (\text{K km s}^{-1})^{-1}$  and  $4 \times 10^{21} \text{ cm}^{-2} (\text{K km s}^{-1})^{-1}$  for the LMC and SMC, respectively, which are similar to values commonly found in the literature (e.g. Rubio et al. 1993; Pineda et al. 2009; Muller et al. 2010; Hughes et al. 2010; Leroy et al. 2007). We find a mean value of  $X_{CO}$  in the LMC of  $9.1 \times 10^{20} \text{ cm}^{-2} (\text{K km s}^{-1})^{-1}$  and in the SMC of  $2.2 \times 10^{21} \text{ cm}^{-2} (\text{K km s}^{-1})^{-1}$ . The correlation between  $X_{CO}$  and  $N(H_2)$  in Figure 17, is a result of the intensity of CO having a much smaller variation compared with the  $H_2$  column density in our sample.

As mentioned above, the reduced dust-to-gas ratio in the low metallicity Magellanic Clouds results in an enhanced photo-destruction of CO which results in CO

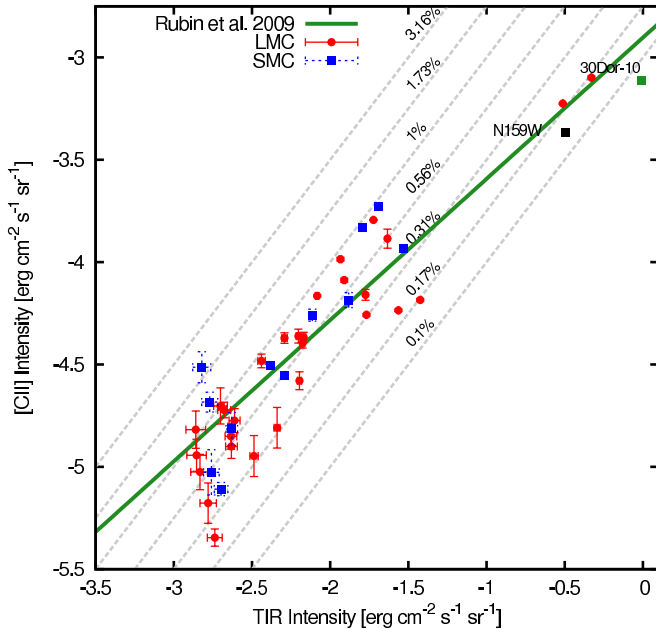


FIG. 18.— The [C II] intensity as a function of the total infrared intensity in our LMC and SMC sample. We also include values for the 30 Dor and N159W massive star forming regions in the LMC, with the [C II] data taken from Boreiko & Betz 1991. The dashed straight lines represent constant values of the photoelectric efficiency ranging from 0.1% to 3.16%, in steps of 0.25 dex. The solid straight line corresponds to the fit of the [C II]–TIR relationship obtained by Rubin et al. (2009).

tracing a smaller volume of the  $H_2$  gas. If this is the case, the  $^{12}CO J = 1 \rightarrow 0$  intensity is reduced by a filling factor, which in turn results in a larger  $X_{CO}$  compared to a cloud with solar metallicity. We can test this effect in our sample, as we derived the filling factor of the CO-emitting gas as part of the excitation analysis in Section 4.4.1. For LOSs detected in  $^{12}CO J = 1 \rightarrow 0$  but where the  $H_2$  column density was derived from  $N(C^+)$ , we assumed a filling factor of unity. In the right panel of Figure 17, we show  $X_{CO}$  as a function of the total  $H_2$  column density in our sample, but this time we multiplied  $X_{CO}$  by the filling factor derived in the excitation analysis, effectively correcting the  $I_{CO}$  intensity for filling factor effects.

While applying this correction increases the scatter in the observed values, we see that the values of  $X_{CO}$  in the LMC and SMC are closer to the value of  $X_{CO}$  in the Milky Way, where the filling factor is closer to unity. The mean values of  $X_{CO}$  in the LMC and SMC are reduced to  $2.9 \times 10^{20} \text{ cm}^{-2} (\text{K km s}^{-1})^{-1}$  and  $7.6 \times 10^{20} \text{ cm}^{-2} (\text{K km s}^{-1})^{-1}$ , respectively, which are closer to the value derived in the Milky Way of  $2 \times 10^{20} \text{ cm}^{-2} (\text{K km s}^{-1})^{-1}$  (Bolatto et al. 2013). The reduced values of  $X_{CO}$  resulting from applying a filling factor seem to confirm that the effect of metallicity on the value of  $X_{CO}$  is to reduce the filling factor of molecular gas traced by CO, resulting in a lower  $^{12}CO J = 1 \rightarrow 0$  intensity which in turn enhances the  $X_{CO}$  factor.

#### 5.4. Photoelectric heating and [C II] cooling

Photoelectric (PE) heating is the main heating mechanism in atomic and diffuse molecular clouds. In this process the gas is heated by energetic electrons that are

expelled from dust grains after they absorb FUV photons (Spitzer 1948). The efficiency in which photoelectric heating works is dependent on the strength of the FUV radiation field, the gas temperature, and the electron density, as well as on grain charging, which depends on the type of dust grain involved.

The efficiency of photoelectric heating can be studied by comparing the total infrared intensity (tracing the energy absorbed by dust) and the [C II] emission, which is the main cooling line in regions where photoelectric heating dominates. Such comparison has been done in the LMC at an angular resolution of  $14.9'$  (217 pc spatial resolution) by Rubin et al. (2009), resulting in PE heating efficiency that varies by a factor of 1.4 between diffuse and bright star-forming regions. They find that overall in the LMC, the [C II] constitutes 1.32% of the LMC’s far infrared luminosity. Similar contributions from [C II] to the observed FIR intensities were found by Israel & Maloney (2011) in several star forming regions in the LMC and SMC with the KAO at a resolution of  $55''$  (13.3 pc for the LMC and 16.2 pc for the SMC) and in a larger sample of low-metallicity dwarf galaxies (Cormier et al. 2015). The [C II]/FIR ratios found in the Magellanic clouds and other dwarf galaxies are higher than the 0.1–0.2% value found in the Milky Way (Wright et al. 1991). This difference in the [C II]/FIR ratio has been attributed to the lower dust-to-gas ratio in low metallicity environments, which results in lower FIR intensity, and in an increased volume of  $C^+$ -emitting regions. In the following, we compare our observations of [C II] in the LMC and SMC with that of the total infrared emission derived from a combination of the *Spitzer* (Meixner et al. 2006) and *Herschel* (Meixner et al. 2013) dust continuum data.

Galametz et al. (2013) compared the resolved galaxy observations of several *Herschel* and *Spitzer* bands with dust spectral energy distribution (SED) models from Draine & Li (2007) to derive empirical relationships between the specific intensity at different bands and the total far infrared intensity (TIR) integrated between  $3 \mu\text{m}$  and  $1100 \mu\text{m}$ . In irregular galaxies (such as the LMC and SMC), the total infrared is related to the far infrared intensity, defined as the intensity integrated between  $42 \mu\text{m}$  and  $122 \mu\text{m}$ , as  $TIR/FIR \approx 2$  (Hunter et al. 2001).

We adopted the calibration for the TIR intensity (in units of  $\text{erg cm}^{-2} \text{ s}^{-1} \text{ sr}^{-1}$ ) presented by Galametz et al. (2013) that uses the *Spitzer*  $24 \mu\text{m}$  and *Herschel*  $100 \mu\text{m}$  specific intensities (in units of  $\text{erg cm}^{-2} \text{ s}^{-1} \text{ sr}^{-1} \text{ Hz}^{-1}$ ),

$$I^{\text{TIR}} = 2.421\nu I_{\nu,24} + 1.410\nu I_{\nu,100}, \quad (13)$$

as it ensures that the resulting TIR intensity can be smoothed to the  $12''$  resolution of the *Herschel* [C II] observations. Galametz et al. (2013) found that this calibration is a good representation of the TIR resulting from full SED modeling of a large number of galaxies observed by *Herschel* and *Spitzer*. At  $12''$  resolution, our comparison between the TIR and [C II] intensities is at 3 pc and 3.5 pc scales in the LMC and SMC, respectively. The resulting TIR maps have a typical uncertainty of  $2 \times 10^{-4} \text{ erg cm}^{-2} \text{ s}^{-1} \text{ sr}^{-1}$ .

In Figure 18, we show the [C II] intensity as a function of the total infrared intensity estimated in the LMC and SMC. In the plot, we also include lines of constant



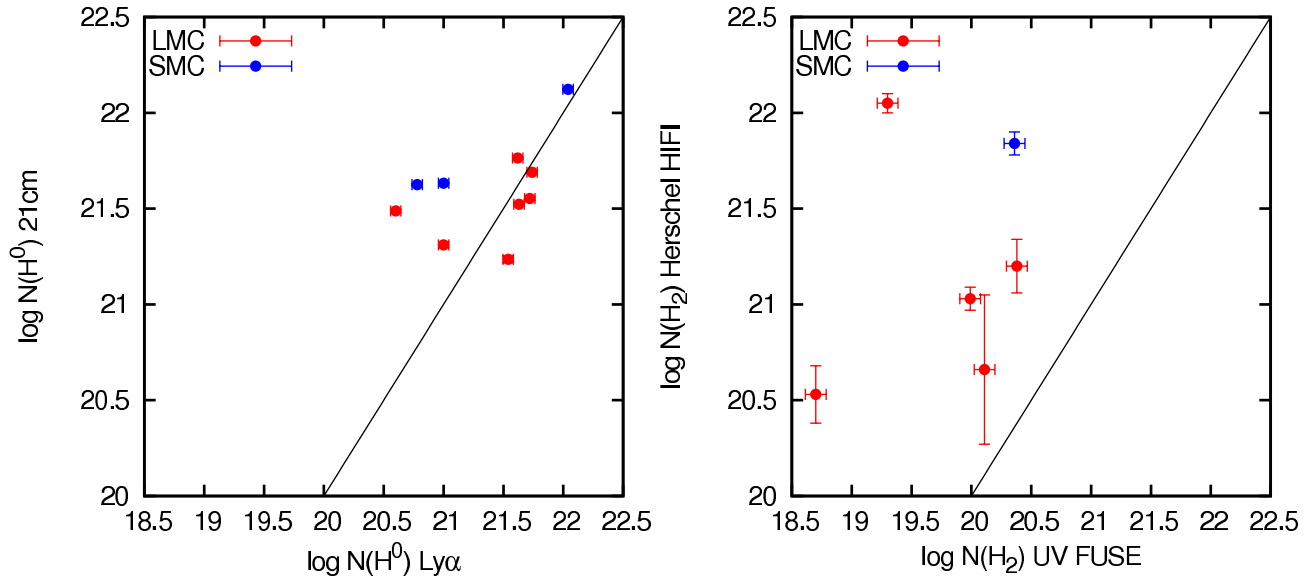


FIG. 19.— (*left*) Comparison of the  $H^0$  column densities derived using 21 cm observations and those derived using optical absorption of the  $Ly\alpha$  line. (*right*) Comparison of the  $H_2$  column densities derived in our analysis and those derived from UV absorption observations. The  $H^0$  and  $H_2$  column densities derived from absorption measurements were compiled by Welty et al. (2012).

$[C\text{II}]/\text{TIR}$  going from 0.1% to 3.16% in steps of 0.25 dex, as well as the fit of the  $[C\text{II}]$  and TIR relationship obtained by Rubin et al. (2009). We find that  $[C\text{II}]$  intensities in both the LMC and SMC have a similar relationship with the total infrared emission despite their different metallicity and dust-to-gas ratio. On average  $[C\text{II}]$  emits 0.6% and 0.8% of the TIR intensity in the LMC and SMC, respectively. In terms of the FIR intensity, these averages correspond to 1.2%, and 1.6%, and thus they are in good agreement with the 1.32% found by Rubin et al. (2009) over the whole LMC and the values found in star forming regions of the LMC and SMC by Israel & Maloney (2011).

Dense photon dominated regions in the LMC tend to have lower  $[C\text{II}]/\text{TIR}$  ratios, with  $[C\text{II}]$  emitting about 0.17% of the TIR. A similar variation from diffuse to bright regions was suggested by Rubin et al. (2009). In Figure 18, we also included data points that correspond to the 30 Dor and N159W massive star forming regions in the LMC ( $[C\text{II}]$  data from Boreiko & Betz 1991 at a  $43''$  resolution), which together with the warm and dense PDRs in our sample, are in agreement with the lower  $[C\text{II}]/\text{TIR}$  ratios at high  $[C\text{II}]$  and TIR intensities suggested by the fit presented by Rubin et al. (2009). The reduced  $[C\text{II}]/\text{TIR}$  ratio in dense PDRs can be understood as the combined effect of high volume densities and the high temperatures resulting from large FUV radiation fields. With increasing volume density and temperature, the excitation of the  $^2P_{3/2}$  level becomes a weak function of these quantities, and the  $[C\text{II}]$  intensity is only a function of column density (Goldsmith et al. 2012). The TIR intensity, which is a function of column density and dust temperature, is unaffected by the larger volume densities and FUV radiation fields.

### 5.5. Comparison with FUSE LOSs

As mentioned in Section 2, our sample contains 7 LOSs in the LMC and 3 in the SMC that coincide with stars that show UV and optical absorption features that are

used to determine the  $H_2$  and  $H^0$  column densities of their foreground gas (e.g. Welty et al. 2012; Cartledge et al. 2005; Tumlinson et al. 2002). In this sub-sample, we detected  $[C\text{II}]$  emission in 5 LOSs in the LMC and in 1 in the SMC, with one LOS in the LMC also detected in  $[C\text{I}]$  and CO. Because the column densities determined in our analysis correspond to the average column density within the beam of our observations, and those from UV and optical absorption correspond to column densities in a pencil beam, a comparison between these column densities will be sensitive to substructure in the ISM of the LMC and SMC. Another difference between these methods to determine column densities is that the column densities in our analysis correspond to the gas along the full sight-line through the LMC or SMC, while the UV and optical absorption only corresponds the gas that is in the foreground of the target stars. Therefore, a comparison between the column densities determined with these different methods can also give us some information on the structure of the ISM along the line-of-sight in the LMC and SMC.

In Figure 19, we compare the  $H^0$  column densities derived using HI 21 cm observations ( $N(H^0)_{21\text{cm}}$ ) and those derived using optical absorption of the  $Ly\alpha$  line ( $N(H^0)_{Ly\alpha}$ ) as well as a comparison between the  $H_2$  column densities derived in our analysis ( $N(H_2)_{\text{HIFI}}$ ) and those derived from UV absorption observations ( $N(H_2)_{\text{UV}}$ ). The  $H^0$  and  $H_2$  column densities derived from absorption observations were compiled by Welty et al. (2012). We see that some LOSs are in reasonable agreement between the column densities derived using HI 21 cm observations and those derived using  $Ly\alpha$  absorption, with some having slightly larger  $N(H^0)_{Ly\alpha}$  than that expected from HI 21 cm observations. However, there are several LOSs that have  $N(H^0)_{Ly\alpha}$  that is significantly lower than  $N(H^0)_{21\text{cm}}$ . We also see that the  $H_2$  column densities in our sample are systematically larger than those derived with FUSE. A similar result is seen in the comparison between atomic hydrogen

column densities in a larger sample presented by Welty et al. (2012) in the LMC and SMC. As explained by these authors,  $N(\text{H}^0)_{\text{Ly}\alpha} < N(\text{H}^0)_{21\text{cm}}$  could be a result of having the bulk of the atomic gas behind the target stars. This effect can also be explained, as well as the case when  $N(\text{H}^0)_{\text{Ly}\alpha} > N(\text{H}^0)_{21\text{cm}}$ , as a result of substructure within the 21 cm beam where the pencil beam of the optical absorption goes through a maximum or a minimum in the gas distribution that have a much different column density compared with the average within the beam. The first explanation would require that  $\text{H}_2$  is more extended along the LOSs than  $\text{H}^0$ , which contradicts the spectral information that shows that  $\text{H I}$  is much more extended in velocity compared with  $[\text{C II}]$ ,  $[\text{C I}]$ , and  $\text{CO}$ . A more likely explanation for our data is the existence of substructure within the beam of the observations. The larger difference for the  $\text{H}_2$  column densities compared to that for the  $\text{H}^0$  column densities could be a reflection of the different structure of the atomic and molecular gas, with the latter concentrated into smaller clumps.

## 6. CONCLUSIONS

In this paper we present a survey of the  $[\text{C II}]$ ,  $[\text{C I}]$ , and  $\text{CO}$  emission observed with high-velocity resolution in the Large and Small Magellanic clouds. The paper aims at characterizing the transition from diffuse atomic to dense molecular clouds in the low-metallicity environments of the Magellanic Clouds. Our sample was selected based on the  $\text{H I}$ ,  $\text{CO}$ , and dust continuum emission and includes regions in different stages in the transition from diffuse regions to dense photon dominated regions associated with star formation. Our results can be summarized as follows:

- We determined the contribution from different phases of the ISM to the observed  $[\text{C II}]$  emission in our sample. In LOSs associated with warm and dense PDRs, the  $[\text{C II}]$  emission from this ISM component tends to dominate. The contribution from diffuse  $\text{CO}$ -dark  $\text{H}_2$  to the observed  $[\text{C II}]$  shows a large scatter, ranging from  $\sim 10\%$  to  $\sim 80\%$ . This large scatter could be a reflection of clouds at different stages in the transition from diffuse to dense molecular gas, with different clouds having varying  $\text{CO}$ -dark  $\text{H}_2$  fractions. We find that ionized and atomic gas have typically smaller contributions to the observed  $[\text{C II}]$  emission (Section 3).
- Using lines-of-sight where only  $\text{H I}$  and  $[\text{C II}]$  emission were detected, and using a derivation of the visual extinction from dust continuum emission, we determined a typical thermal pressure of the diffuse ISM to be  $p_{\text{th}}/k_{\text{B}} = 3.4 \times 10^4 \text{ K cm}^{-3}$  in the LMC and  $1 \times 10^5 \text{ K cm}^{-3}$  in the SMC (Section 4.3).
- We used the  $[\text{C I}]$  and  $\text{CO}$  observations to determine the column density, kinetic temperature, and volume density of the  $\text{CO}$  and  $[\text{C I}]$ -emitting gas. We find average values and standard deviations in the  $\text{CO}$ -emitting layer of  $44 \pm 19 \text{ K}$  in the LMC and  $50 \pm 20 \text{ K}$  in the SMC for the kinetic temperature,  $10^{16.7 \pm 0.5} \text{ cm}^{-2}$  in the LMC and  $10^{16.6 \pm 0.3} \text{ cm}^{-2}$  in the SMC for the beam-averaged  $\text{CO}$  column density,  $10^{5.1 \pm 0.9} \text{ cm}^{-3}$  in

the LMC and  $10^{4.0 \pm 0.3} \text{ cm}^{-3}$  in the SMC for the  $\text{H}_2$  volume density, and  $(0.2 \pm 0.2)$  in the LMC and  $(0.20 \pm 0.3)$  in the SMC for the filling factor. In the  $[\text{C I}]$ -emitting layer we find  $91 \pm 60 \text{ K}$  in the LMC and  $73 \pm 62 \text{ K}$  in the SMC for the kinetic temperature,  $10^{16.4 \pm 0.4} \text{ cm}^{-2}$  in the LMC and  $10^{16.2 \pm 0.3} \text{ cm}^{-2}$  in the SMC for the beam-averaged  $\text{C}^0$  column density, and  $10^{4.8 \pm 1.4} \text{ cm}^{-3}$  in the LMC and  $10^{3.5 \pm 0.5} \text{ cm}^{-3}$  in the SMC for the  $\text{H}_2$  volume density. This information combined with the  $[\text{C II}]$  observations allows us to calculate the column densities of  $\text{CO}$ -dark  $\text{H}_2$  gas in our sample (Section 4.4).

- We studied the transition between atomic and molecular gas in the LMC and SMC by comparing the  $\text{H}_2$  column densities of  $\text{CO}$ -dark  $\text{H}_2$  and  $\text{CO}$ -traced  $\text{H}_2$  with the total hydrogen,  $N(\text{H}^0) + 2N(\text{H}_2)$ , column density in our sample. We find reasonable agreement between our observations and theoretical models of the  $\text{H}^0$  to  $\text{H}_2$  transition (Section 5.1).
- We found that most of the observed  $\text{H I}$  is in the form of WNM. We estimate that the CNM represents 28% and 14% of the total  $\text{H}^0$  column density in the LMC and SMC, respectively. The value in the LMC is similar to that in the Milky Way (40%; Heiles & Troland 2003; Pineda et al. 2013) while in the SMC the WNM represents a larger fraction (Section 5.1).
- We found that the  $\text{H}_2$  column densities determined using  $[\text{C II}]$ ,  $[\text{C I}]$ , and  $\text{CO}$  observations in our survey trace molecular fractions between  $0.1 \leq f(\text{H}_2) \leq 1$  range. In contrast UV absorption observations mostly trace  $f(\text{H}_2) \leq 0.2$ . The  $\text{C}^0$  and  $\text{CO}$  column densities have a measurable contribution to the total gas-phase carbon column density for molecular fractions  $f(\text{H}_2) \geq 0.45$ , while  $[\text{C II}]$  alone traces a larger range in the molecular fraction down to 0.1 (Section 5.1).
- Studying the  $\text{C}^+/\text{C}^0/\text{CO}$  transitions in our sample in the LMC and SMC reveals that most of the molecular gas in our sample is traced by  $[\text{C II}]$ . Both column densities of neutral carbon and  $\text{CO}$  represent a lower fraction of the total carbon associated with molecular gas along the line-of-sight. On average,  $\text{C}^+$ ,  $\text{C}^0$ , and  $\text{CO}$  represent 89%, 9%, and 10% of the gas-phase carbon in the LMC and 77%, 6%, and 17% in the SMC, respectively. The  $[\text{C I}]$  and  $\text{CO}$  are detected above  $N(\text{H}_2) \sim 10^{21.5} \text{ cm}^{-2}$  in the LMC and  $\sim 10^{21.8} \text{ cm}^{-2}$  in the SMC. The difference in the thresholds for  $[\text{C I}]$  and  $\text{CO}$  detection is possible a result of the metallicity and dust-to-gas ratio difference between the LMC and SMC (Section 5.2).
- We found a mean value of the  $X_{\text{CO}}$  conversion factor in the LMC of  $9.1 \times 10^{20} \text{ cm}^{-2} (\text{K km s}^{-1})^{-1}$  and in the SMC of  $2.2 \times 10^{21} \text{ cm}^{-2} (\text{K km s}^{-1})^{-1}$ , which are larger than the value of  $2 \times 10^{20} \text{ cm}^{-2} (\text{K km s}^{-1})^{-1}$  in the Milky Way. When

applying a filling factor correction to the CO emission we see that the values of  $X_{\text{CO}}$  in the LMC and SMC become closer to the value of  $X_{\text{CO}}$  in the Milky Way, where the filling factor is close to unity. This result suggests that the effect of metallicity in the value of  $X_{\text{CO}}$  is to reduce the filling factor of molecular gas traced by CO, which results in a lower  $^{12}\text{CO } J = 1 \rightarrow 0$  intensity which in turn results in an enhanced  $X_{\text{CO}}$  factor (Section 5.3).

- We found that most of the LOSs in our sample are consistent with a linear relationship between the [C II] and the total infrared emission (TIR). The [C II] emission represents about 1% of the TIR in both the LMC and SMC despite their difference in metallicity and dust-to-gas ratio. This [C II]/TIR fraction is consistent with previous determination using the [C II] map of the LMC observed with the BICE balloon (Section 5.4).
- We compared the  $\text{H}^0$  and  $\text{H}_2$  column densities derived in our analysis and those derived using optical and UV absorption in a sub-sample of our survey. We find significant discrepancies between the column density observations which can be explained

by substructure within the beam used for our observations (Section 5.5).

In conclusion, our results show that [C II], [C I], and CO observations are important tools for characterizing the transition from atomic to molecular clouds in external galaxies. Future large scale mapping of the LMC and SMC in these spectral lines with current/future balloon, airborne (SOFIA), and space observatories will make significant steps in our understanding of the evolution of the ISM, star formation, and galaxy evolution.

We would like to thank Drs. Julia Roman-Duval and Cheoljong Lee for providing their dust continuum data sets and Dr. Franck Le Petit for his help on comparing our H I and  $\text{H}_2$  data sets with theoretical predictions. We also thank an anonymous referee for a number of useful comments that significantly improved the manuscript. This research was conducted at the Jet Propulsion Laboratory, California Institute of Technology under contract with the National Aeronautics and Space Administration. We thank the staffs of the ESA and NASA *Herschel* Science Centers for their help. © 2016 California Institute of Technology. U.S. Government sponsorship acknowledged.

## APPENDIX

### BEAM DILUTION CORRECTION

#### *Absolute Intensities*

Our survey contains a set of multi-wavelength observations with different angular resolutions. When possible our analysis was made with data at matching resolutions, but there are cases in which we have to rely on a combination of data with different angular resolutions. In order to quantify how beam dilution affects the results involving absolute intensities presented in this paper, we smoothed the  $12''$  angular resolution  $160 \mu\text{m}$  HERITAGE dust continuum maps of the LMC and SMC to the different angular resolutions of data set used in our analysis ( $12''$ ,  $17''$ ,  $27''$ ,  $33''$ ,  $44''$ ,  $48''$ , and  $60''$ ). We assumed that the distribution of dust continuum emission is similar to that of the spectral lines used in our analysis. This assumption is motivated by the agreement between dust continuum and [C II] maps in star forming regions in the LMC (see e.g. Okada et al. 2015 and Galametz et al. 2013 for N159). We choose a reference angular resolution of  $40''$  which is an intermediate value between  $12''$  and  $60''$ . In Figure 20, we show the variation of the absolute  $160 \mu\text{m}$  intensities for angular resolutions between  $12''$  and  $60''$  with respect to that at  $40''$ . Remarkably, most of our LOSs in the LMC and SMC show variations within  $\sim 40\%$  in the  $12''$  to  $60''$  range, even though the beam area varies by a factor of 25. There are however four exceptions, NT77, PDR3\_NE, PDR2\_NW, and LMC12\_NW where the intensities vary by factors of 6, 3.5, 2, and 1.7 respectively. In the SMC, AzV462, SMC\_NE\_1a, and SMC\_LIRS36, have the largest variations with factors of 2.3, 2, and 1.8, respectively. Note that we did not detect [C II] emission in AzV462.

We also studied the variations of the SHASSA  $\text{H}\alpha$  intensities for varying angular resolution, by using the  $24 \mu\text{m}$  dust continuum maps of the LMC and SMC. The  $24 \mu\text{m}$  continuum emission is a proxy for hot dust emission associated with H II regions. The angular resolution of the  $24 \mu\text{m}$  images is  $6''$ . We convolved these images to  $12''$  corresponding to [C II] observations and to  $48''$  corresponding to that of the  $\text{H}\alpha$  map. We then computed the ratio of the  $24 \mu\text{m}$  intensities at  $12''$  and  $48''$  to determine a beam dilution correction factor for the  $\text{H}\alpha$  data, which we use to quantify the impact of beam dilution in our results. We find that the median flux variation between  $12''$  and  $48''$  is a factor of 1.15 in both in the LMC and SMC. The mean variations are factors of 1.6 in the LMC and of 1.7 in the SMC. The difference between the median and mean factors are mostly driven by three LOSs in both the LMC and SMC that show larger variations in their fluxes. In the LMC, they are SK-67D2, PDR3\_NE, and NT77, with fluxes varying by factors of 3.1, 3.4, and 8.3, respectively. (Note that SK-67D2 was not detected in [C II] in our survey.) In the SMC, the LOSs with the largest variations are SMC\_LIRS36, SMC\_NE\_1a, and SMC\_NE\_4c\_low, with fluxes varying by factors of 3.6, 3.7, 5.2, respectively.

In Figure 21, we present the fraction of [C II] originating from different ISM phases as a function of the observed [C II] intensity in the case when the intensities are corrected by beam dilution effects. All quantities involved in the calculation of the contribution from different ISM phases to the observed [C II] emission have been corrected by beam filling effect to correspond to a common angular resolution of  $40''$ . In general, beam dilution effects have a small impact in the fraction of [C II] emission originating from the different phases of the ISM.



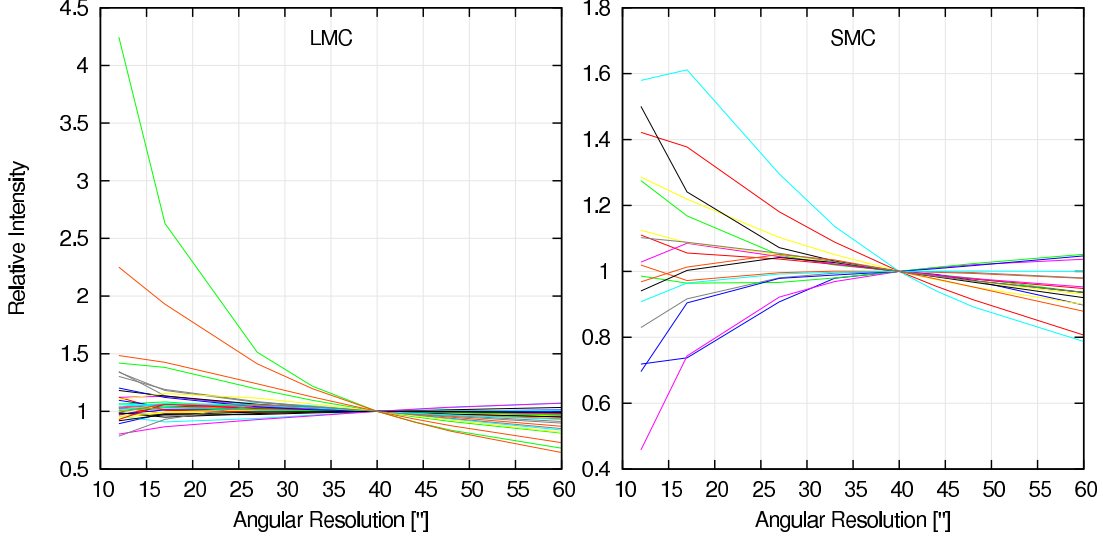


FIG. 20.— The  $160\ \mu\text{m}$  dust continuum intensity smoothed to different angular resolutions relative to that at  $40''$  as a function of angular resolution for our sample in the LMC (*left panel*) and SMC (*right panel*).

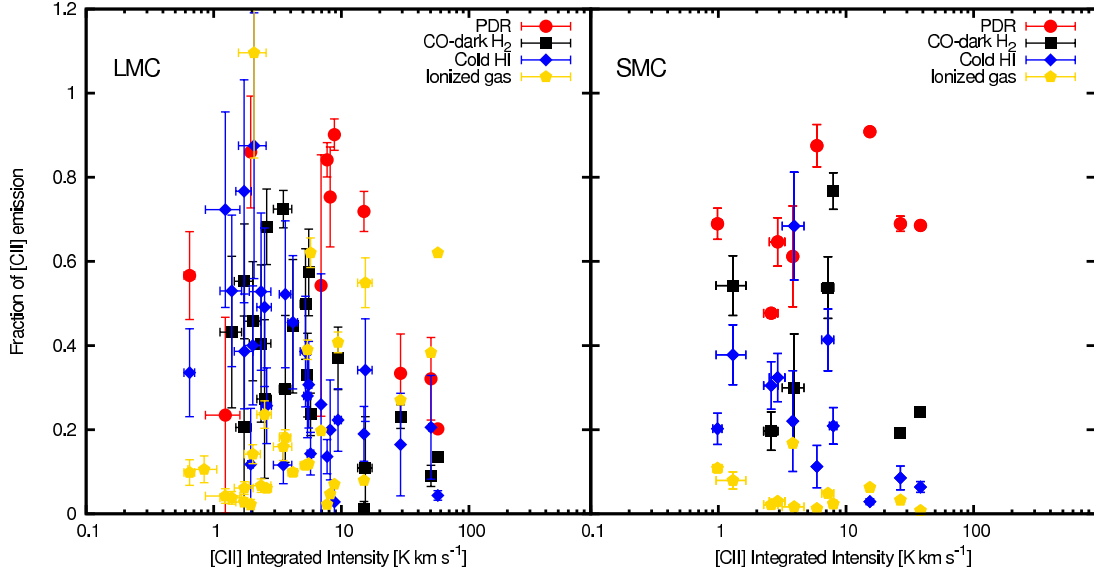


FIG. 21.— The fraction of the  $[\text{C II}]$  emission that we estimate arises from ionized gas, cold atomic gas, CO–dark  $\text{H}_2$ , and photon dominated regions (PDRs) as a function of the observed  $[\text{C II}]$  emission in the LMC and SMC. All data points have been corrected by dilution effects as described in Appendix A.

### Line Ratios

Another instance where we use a combination of pointed observations at different angular resolutions is in the excitation analysis in Section 4.4, where we use line ratios of CO and  $[\text{C I}]$  lines to estimate the physical conditions of the CO and  $[\text{C I}]$ -emitting gas. In the following we describe a simple model that we used to account for beam dilution effects in the line ratios. Because we assume Gaussian sources, the model provides only a first order correction to the observed line ratios, as the structure of the ISM is likely to be more complex.

The ratio of the antenna temperatures of two lines,  $T_1^*$  and  $T_2^*$ , originating from a Gaussian source with FWHM size  $\Theta_s$ , when observed having the same FWHM beam size  $\Theta_f$  centered in the source, is given by

$$\frac{T_1^*}{T_2^*} = \frac{T_1 \Theta_s^2}{\Theta_f^2 + \Theta_s^2} = \frac{T_1}{T_2}, \quad (\text{A1})$$

where  $T_1$  and  $T_2$  are the intrinsic peak antenna temperature of the source. When the source is convolved with Gaussians having two different FWHM beam size  $\Theta_a$  and  $\Theta_b$ , the integrated intensity ratio is given by

$$\frac{T_1^*}{T_2^*} = \frac{T_1 \Theta_s^2 + \Theta_b^2}{T_2 \Theta_s^2 + \Theta_a^2}, \quad (\text{A2})$$

Thus, the intrinsic ratio is related to the observed ratio as

$$\frac{T_1}{T_2} = \frac{T_1^*}{T_2^*} f_{1,2}, \quad (\text{A3})$$

where

$$f_{1,2} \equiv \frac{\Theta_s^2 + \Theta_a^2}{\Theta_s^2 + \Theta_b^2}. \quad (\text{A4})$$

The observed line ratio can therefore be corrected for beam dilution effects if an estimate  $f_{1,2}$  is available. We can estimate  $f_{1,2}$  by comparing the line or continuum emission of the same source at different angular resolutions. In this case  $T_1 = T_2$  and therefore the dilution factor is given by the inverse of the ratio of the convolved peak intensities,  $f_{1,2} = T_2^*/T_1^*$ .

We used the 160  $\mu\text{m}$  HERITAGE dust continuum map with 12'' angular resolution to estimate  $f_{1,2}$  for the sources in our survey. We smoothed the 160  $\mu\text{m}$  map to the different angular resolution of the spectral lines involved in our analysis (17'', 27'', 33'', and 44'') and calculated the dilution factors of each line ratio using Equation (A4) by calculating the ratio of the 160  $\mu\text{m}$  emission at the different angular resolution pairs. We used the derived correction factors to study the effect beam dilution in the line ratios used in our analysis. Note that we do not correct the line ratios for beam dilution effects in our analysis, due to the uncertainties of whether dust continuum emission traces the distribution of gas. In Table 6, we present the effect of beam dilution in the line ratios that are calculated using observations at different angular resolutions. We find that these line ratios would typically vary by 10%. This small variation suggest that the observed structures are relatively extended at the resolution of our observations.

#### REFERENCES

- Alves, M. I. R., Calabretta, M., Davies, R. D., et al. 2015, *MNRAS*, 450, 2025
- Barinovs, Ģ., van Hemert, M. C., Krems, R., & Dalgarno, A. 2005, *ApJ*, 620, 537
- Bernard, J.-P., Reach, W. T., Paradis, D., et al. 2008, *AJ*, 136, 919
- Bialy, S., & Sternberg, A. 2016, *ApJ*, 822, 83
- Blitz, L., & Rosolowsky, E. 2006, *ApJ*, 650, 933
- Bohlin, R. C., Savage, B. D., & Drake, J. F. 1978, *ApJ*, 224, 132
- Bolatto, A. D., Wolfire, M., & Leroy, A. K. 2013, *ARA&A*, 51, 207
- Bolatto, A. D., Leroy, A. K., Jameson, K., et al. 2011, *ApJ*, 741, 12
- Boreiko, R. T., & Betz, A. L. 1991, *ApJ*, 380, L27
- Boulares, A., & Cox, D. P. 1990, *ApJ*, 365, 544
- Carilli, C. L., & Walter, F. 2013, *ARA&A*, 51, 105
- Cartledge, S. I. B., Clayton, G. C., Gordon, K. D., et al. 2005, *ApJ*, 630, 355
- Chevance, M., Madden, S. C., Lebouteiller, V., et al. 2016, *A&A*, 590, A36
- Cohen, R. S., Dame, T. M., Garay, G., et al. 1988, *ApJ*, 331, L95
- Cormier, D., Madden, S. C., Lebouteiller, V., et al. 2015, *A&A*, 578, A53
- de Graauw, T., Helmich, F. P., Phillips, T. G., et al. 2010, *A&A*, 518, L6+
- Dickey, J. M., Mebold, U., Stanimirovic, S., & Staveley-Smith, L. 2000, *ApJ*, 536, 756
- Draine, B. T. 1978, *ApJS*, 36, 595
- Draine, B. T., & Li, A. 2007, *ApJ*, 657, 810
- Dufour, R. J., Shields, G. A., & Talbot, Jr., R. J. 1982, *ApJ*, 252, 461
- Dwek, E. 1998, *ApJ*, 501, 643
- Field, G. B., Goldsmith, D. W., & Habing, H. J. 1969, *ApJ*, 155, L149
- Fitzpatrick, E. L. 1985a, *ApJ*, 299, 219
- , 1985b, *ApJS*, 59, 77
- Galametz, M., Kennicutt, R. C., Calzetti, D., et al. 2013, *MNRAS*, 431, 1956
- Gaustad, J. E., McCullough, P. R., Rosing, W., & Van Buren, D. 2001, *PASP*, 113, 1326
- Gnedin, N. Y., Tassis, K., & Kravtsov, A. V. 2009, *ApJ*, 697, 55
- Goldsmith, P. F. 2013, *ApJ*, 774, 134
- Goldsmith, P. F., Langer, W. D., Pineda, J. L., & Velusamy, T. 2012, *ApJS*, 203, 13
- Goldsmith, P. F., Pineda, J. L., Langer, W. D., et al. 2016, *ApJ*, 824, 141
- Goldsmith, P. F., Yıldız, U. A., Langer, W. D., & Pineda, J. L. 2015, *ApJ*, 814, 133
- Gordon, K. D., Clayton, G. C., Misselt, K. A., Landolt, A. U., & Wolff, M. J. 2003, *ApJ*, 594, 279
- Gordon, K. D., Roman-Duval, J., Bot, C., et al. 2014, *ApJ*, 797, 85
- Grenier, I. A., Casandjian, J.-M., & Terrier, R. 2005, *Science*, 307, 1292
- Güsten, R., Nyman, L. Å., Schilke, P., et al. 2006, *A&A*, 454, L13
- Haffner, L. M., Dettmar, R.-J., Beckman, J. E., et al. 2009, *Reviews of Modern Physics*, 81, 969
- Heiles, C., & Troland, T. H. 2003, *ApJ*, 586, 1067
- Heyer, M., & Dame, T. M. 2015, *ARA&A*, 53, 583
- Higgins, D. R. 2011, PhD thesis, National University of Ireland Maynooth
- Higgins, R. D., & Kooi, J. W. 2009, in *Society of Photo-Optical Instrumentation Engineers (SPIE) Conference Series*, Vol. 7215, *Society of Photo-Optical Instrumentation Engineers (SPIE) Conference Series*
- Hilditch, R. W., Howarth, I. D., & Harries, T. J. 2005, *MNRAS*, 357, 304
- Hughes, A., Wong, T., Ott, J., et al. 2010, *MNRAS*, 406, 2065
- Hunter, D. A., Kaufman, M., Hollenbach, D. J., et al. 2001, *ApJ*, 553, 121
- Israel, F. 2000, in *Molecular Hydrogen in Space*, ed. F. Combes & G. Pineau Des Forets, 293
- Israel, F. P. 1997, *A&A*, 328, 471
- Israel, F. P., & Maloney, P. R. 2011, *A&A*, 531, A19
- Israel, F. P., Maloney, P. R., Geis, N., et al. 1996, *ApJ*, 465, 738
- Jenkins, E. B., & Tripp, T. M. 2011, *ApJ*, 734, 65
- Kalberla, P. M. W., & Kerp, J. 2009, *ARA&A*, 47, 27
- Kim, S. 2006, *PASP*, 118, 94
- Kim, S., Staveley-Smith, L., Dopita, M. A., et al. 2003, *ApJS*, 148, 473
- Koornneef, J. 1982, *A&A*, 107, 247
- Krumholz, M. R., McKee, C. F., & Tumlinson, J. 2008, *ApJ*, 689, 865
- , 2009, *ApJ*, 693, 216
- Ladd, N., Purcell, C., Wong, T., & Robertson, S. 2005, *PASA*, 22, 62
- Langer, W. D., Goldsmith, P. F., & Pineda, J. L. 2016, *A&A*, 590, A43
- Langer, W. D., Velusamy, T., Pineda, J. L., et al. 2010, *A&A*, 521, L17
- Langer, W. D., Velusamy, T., Pineda, J. L., Willacy, K., & Goldsmith, P. F. 2014, *A&A*, 561, A122
- Lee, C., Leroy, A. K., Schnee, S., et al. 2015, *MNRAS*, 450, 2708
- Lee, M.-Y., Madden, S., Lebouteiller, V., et al. 2016, *ArXiv e-prints*, arXiv:1606.04290
- Lequeux, J. 1989, in *Recent Developments of Magellanic Cloud Research*, ed. K. S. de Boer, F. Spite, & G. Stasińska, 119
- Leroy, A., Bolatto, A., Stanimirovic, S., et al. 2007, *ApJ*, 658, 1027
- Li, A., & Draine, B. T. 2002, *ApJ*, 576, 762
- Madden, S. C., Poglitsch, A., Geis, N., Stacey, G. J., & Townes, C. H. 1997, *ApJ*, 483, 200
- Martin, N., Maurice, E., & Lequeux, J. 1989, *A&A*, 215, 219
- Marx-Zimmer, M., Herbstmeier, U., Dickey, J. M., et al. 2000, *A&A*, 354, 787
- Marx-Zimmer, M., Zimmer, F., Herbstmeier, U., & Dickey, J. M. 1999, in *IAU Symposium*, Vol. 190, *New Views of the Magellanic Clouds*, ed. Y.-H. Chu, N. Suntzeff, J. Hesser, & D. Bohlender, 124

- McKee, C. F. 1989, *ApJ*, 345, 782
- McKee, C. F., & Krumholz, M. R. 2010, *ApJ*, 709, 308
- Meixner, M., Gordon, K. D., Indebetouw, R., et al. 2006, *AJ*, 132, 2268
- Meixner, M., Panuzzo, P., Roman-Duval, J., et al. 2013, *AJ*, 146, 62
- Minamidani, T., Mizuno, N., Mizuno, Y., et al. 2008, *ApJS*, 175, 485
- Minamidani, T., Tanaka, T., Mizuno, Y., et al. 2011, *AJ*, 141, 73
- Mochizuki, K., Nakagawa, T., Doi, Y., et al. 1994, *ApJ*, 430, L37
- Muller, E., Ott, J., Hughes, A., et al. 2010, *ApJ*, 712, 1248
- Okada, Y., Requena-Torres, M. A., Güsten, R., et al. 2015, *A&A*, 580, A54
- Ostriker, E. C., McKee, C. F., & Leroy, A. K. 2010, *ApJ*, 721, 975
- Ott, S., Bakker, J., Brumfit, J., et al. 2006, in *Astronomical Society of the Pacific Conference Series*, Vol. 351, *Astronomical Data Analysis Software and Systems XV*, ed. C. Gabriel, C. Arviset, D. Ponz, & S. Enrique, 516
- Paradis, D., Paladini, R., Noriega-Crespo, A., et al. 2011, *ApJ*, 735, 6
- Parker, J. W., Garmany, C. D., Massey, P., & Walborn, N. R. 1992, *AJ*, 103, 1205
- Pellegrini, E. W., Baldwin, J. A., & Ferland, G. J. 2011, *ApJ*, 738, 34
- Pikel'Ner, S. B. 1968, *Soviet Ast.*, 11, 737
- Pilbratt, G. L., Riedinger, J. R., Passvogel, T., et al. 2010, *A&A*, 518, L1+
- Pineda, J. L., Goldsmith, P. F., Chapman, N., et al. 2010, *ApJ*, 721, 686
- Pineda, J. L., Langer, W. D., Velusamy, T., & Goldsmith, P. F. 2013, *A&A*, 554, A103
- Pineda, J. L., Ott, J., Klein, U., et al. 2009, *ApJ*, 703, 736
- Pineda, J. L., Mizuno, N., Stutzki, J., et al. 2008, *A&A*, 482, 197
- Pineda, J. L., Mizuno, N., Röllig, M., et al. 2012, *A&A*, 544, A84
- Poglitsch, A., Krabbe, A., Madden, S. C., et al. 1995, *ApJ*, 454, 293
- Requena-Torres, M. A., Israel, F. P., Okada, Y., et al. 2016, *A&A*, 589, A28
- Reynolds, R. J. 1991, *ApJ*, 372, L17
- Roman-Duval, J., Gordon, K. D., Meixner, M., et al. 2014, *ApJ*, 797, 86
- Rubin, D., Hony, S., Madden, S. C., et al. 2009, *A&A*, 494, 647
- Rubio, M., Garay, G., Montani, J., & Thaddeus, P. 1991, *ApJ*, 368, 173
- Rubio, M., Lequeux, J., & Boulanger, F. 1993, *A&A*, 271, 9
- Sandstrom, K. M., Bolatto, A. D., Draine, B. T., Bot, C., & Stanimirović, S. 2010, *ApJ*, 715, 701
- Schaefer, B. E. 2008, *AJ*, 135, 112
- Schöier, F. L., van der Tak, F. F. S., van Dishoeck, E. F., & Black, J. H. 2005, *A&A*, 432, 369
- Sheffer, Y., Rogers, M., Federman, S. R., et al. 2008, *ApJ*, 687, 1075
- Sofia, U. J., Cardelli, J. A., Guerin, K. P., & Meyer, D. M. 1997, *ApJ*, 482, L105
- Spitzer, Jr., L. 1948, *ApJ*, 107, 6
- Stanimirovic, S., Staveley-Smith, L., Dickey, J. M., Sault, R. J., & Snowden, S. L. 1999, *MNRAS*, 302, 417
- Staveley-Smith, L., Kim, S., Calabretta, M. R., Haynes, R. F., & Kesteven, M. J. 2003, *MNRAS*, 339, 87
- Sternberg, A., Le Petit, F., Roueff, E., & Le Bourlot, J. 2014, *ApJ*, 790, 10
- Stutzki, J., Graf, U. U., Haas, S., et al. 1997, *ApJ*, 477, L33+
- Tang, N., Li, D., Heiles, C., et al. 2016, *A&A*, 593, A42
- Tielens, A. G. G. M., & Hollenbach, D. 1985, *ApJ*, 291, 722
- Tumlinson, J., Shull, J. M., Rachford, B. L., et al. 2002, *ApJ*, 566, 857
- van der Tak, F. F. S., Black, J. H., Schöier, F. L., Jansen, D. J., & van Dishoeck, E. F. 2007, *A&A*, 468, 627
- van Dishoeck, E. F., & Black, J. H. 1988, *ApJ*, 334, 771
- Viallefond, F., & Goss, W. M. 1986, *A&A*, 154, 357
- Wang, M., Chin, Y.-N., Henkel, C., Whiteoak, J. B., & Cunningham, M. 2009, *ApJ*, 690, 580
- Weingartner, J. C., & Draine, B. T. 2001, *ApJ*, 548, 296
- Welty, D. E., Lauroesch, J. T., Wong, T., & York, D. G. 2016, *ApJ*, 821, 118
- Welty, D. E., Xue, R., & Wong, T. 2012, *ApJ*, 745, 173
- Westerlund, B. E. 1997, *The Magellanic Clouds* (New York: Cambridge Univ. Press)
- Whittet, D. C. B., Gerakines, P. A., Hough, J. H., & Shenoy, S. S. 2001, *ApJ*, 547, 872
- Wiesenfeld, L., & Goldsmith, P. F. 2014, *ApJ*, 780, 183
- Wilson, N. J., & Bell, K. L. 2002, *MNRAS*, 337, 1027
- Wolfire, M. G., Hollenbach, D., & McKee, C. F. 2010, *ApJ*, 716, 1191
- Wolfire, M. G., Hollenbach, D., McKee, C. F., Tielens, A. G. G. M., & Bakes, E. L. O. 1995, *ApJ*, 443, 152
- Wolfire, M. G., McKee, C. F., Hollenbach, D., & Tielens, A. G. G. M. 2003, *ApJ*, 587, 278
- Wong, T., Hughes, A., Ott, J., et al. 2011, *ApJS*, 197, 16
- Wright, E. L., Mather, J. C., Bennett, C. L., et al. 1991, *ApJ*, 381, 200